Tunneling Spectroscopy of the Quantum Hall edge states using GaAs Quantum Wires

Inauguraldissertation

zur

Erlangung der Würde eines Doktors der Philosophie

vorgelegt der

Philosophisch-Naturwissenschaftlichen Fakultät

der Universität Basel

von

Taras Patlatiuk

aus der Ukraine

2021

Genehmigt von der Philosophisch-Naturwissenschaftlichen Fakultät

auf Antrag von

Prof. D. M. Zumbühl

Dr. H. Steinberg

Basel, den 19.2.2019

Prof. Dr. Martin Spiess

Dekan

Abstract

Edge states play a crucial role in many condensed matter systems, including the quantum Hall effect and topological insulators. Knowledge and control of the properties of the edge states is of particular importance for both fundamental understanding of novel materials and potential practical applications.

In this thesis a new spectroscopy technique to probe the integer quantum Hall edge states is demonstrated. For this, a GaAs cleaved edge overgrowth quantum wire is used as a momentum-conserving probe tunnel coupled to a 2D electron gas (2DEG), which at finite perpendicular magnetic field hosts the integer quantum Hall edge states. An in-plane magnetic field is used to match the momentum of the 1D wire with the momentum of an edge state, allowing one to discriminate spatially overlapping quantum Hall edge states. Using this technique, the momentum and the guiding center position of multiple integer quantum Hall edge states was tracked from very low magnetic fields all the way up to higher magnetic fields where individual edge states are magnetically depopulated. Analytical and numerical models that infer the properties of the edge states from the bulk spectrum were developed. These models quantitatively capture the whole magnetic field evolution of the observed tunneling resonances. Additionally, features that go beyond the single-particle picture such as exchange-enhanced spin splitting and signatures of edge-state reconstruction were also observed.

The ability to fabricate a 1D wires from other materials and tunnel couple them to novel systems, for example, topological insulators, would greatly broaden the applicability of the described spectroscopy technique. In addition, fabrication of the nanowires with strong spin-orbit interaction is also very important for the realization of the topological qubits based on Majorana Fermions, which are expected to be more robust against decoherence compared to the other types of qubits.

A promising growth technique of InGaAs nanowires on top of defect-free GaAs nanomembranes using molecular beam epitaxy was investigated. This growth tech-

nique is particularly attractive as it allows for the fabrication of patternable and highly regular branched nanowire arrays, necessary for scaling up the number of qubits. The coherence length of 130 nm and a lower bound on the spin-orbit length of 280 nm were obtained for such nanowires by fitting a simple quasi-1D transport model to magnetoconductance measurements.

The presence of quasiparticles in the superconductor could destroy the topological protection of the qubits based on Majorana fermions. The thermal population of quasiparticles also limits the operation temperature of the near term quantum computers based on superconducting qubits. For the normal metal-insulator-superconductor (NIS) tunnel junctions the quasiparticles produce a subgap leakage current characterized by the Dynes parameter.

By careful shielding and filtering of the measurement lines connected to the tunnel junction, finite-bias current steps were observed in the characteristic IV curves of NIS devices, which potentially could explain the origin of the phenomenological Dynes parameter. Qualitatively similar steps were observed in numerical simulations and were attributed to the sample specific geometry and disorder configuration enhanced Andreev reflections.

Contents

1 Background

1.1 Cleaved-edge overgrowth quantum wires

1.1.1 Growth and fundamental properties

The ability to confine an electron gas into two dimensions (2DEG) opens the doors for discovering of many new phenomena, including the quantum Hall effect, quantum dots, etc. A number of new phenomena are expected to be even larger in one dimension (1D). Electrons confined to one-dimensional wires are expected to have long correlation lengths because of electron-electron (e-e) interactions. Unfortunately, this makes 1D systems very susceptible to pinning by impurities at low temperatures, which causes the system to go into the insulating phase, and makes the study of strongly correlated 1D electron systems very challenging. An important signature of a non-interacting ballistic 1D conductor is the quantization of its electrical conductivity by integer multiples of the conductance quantum $G_0 = 2e^2/h$, where e is the electron charge and h is the Planck constant and the factor of 2 is due to spin degeneracy.

One of the first methods to prepare 1D wires was using surface gates to deplete a 2DEG in order to form a narrow electron channel. Usually 2DEG's are buried deep below the surface of the sample to ensure a high electron mobility, so the gates located at the surface of the wafer generate a weak lateral confinement in such wires that results in a small subband spacing. In this case, even small potential fluctuations induced by the gate's roughness or impurities located near the channel easily mix different modes and destroy ballistic electron transport.

A big breakthrough happened after the discovery of a new wire fabrication technique called Cleaved-Edge Overgrowth (CEO) [1, 2], which consists of two molecular beam epitaxy (MBE) growths. The first step is to form a 2DEG in a modulation doped GaAs quantum well, embedded between two AlGaAs layers, that resides 500 nm below the surface of the wafer, shown in Fig.1a. In the second step, tungsten top gates with

a width of $2 - 10\,\mu$m are evaporated onto the wafer surface. These gates can locally deplete the 2DEG and define the length of the quantum wires. Next, the wafer with the prefabricated gates is loaded again into the MBE chamber, where it is cleaved under a high vacuum environment, Fig.1b. This exposes an atomically clean (110) surface that is used as a substrate for the second MBE growth of AlGaAs with a layer of side dopants (green), Fig.1c. This provides the tight confinement of electrons at the edge of the GaAs on three sides by atomically smooth semiconductor interfaces and by a strong electric field, induced by overgrowth dopants in the fourth direction. Under application of negative voltage to the top gates, electrons are repelled from underneath the gate. For sufficiently negative voltage, all electrons are removed from the bulk of the sample. At this point, electrons are only left at the edge of the sample because of the attractive force induced by the side dopants. These electrons form a quantum wire with the length roughly equal to the length of the gate. The 2DEG to the left and to the right of the gate serve as source and drain contacts to the wire. The gate voltage also controls the density of the electrons in the wire and, correspondingly, the number of quantum wire modes.

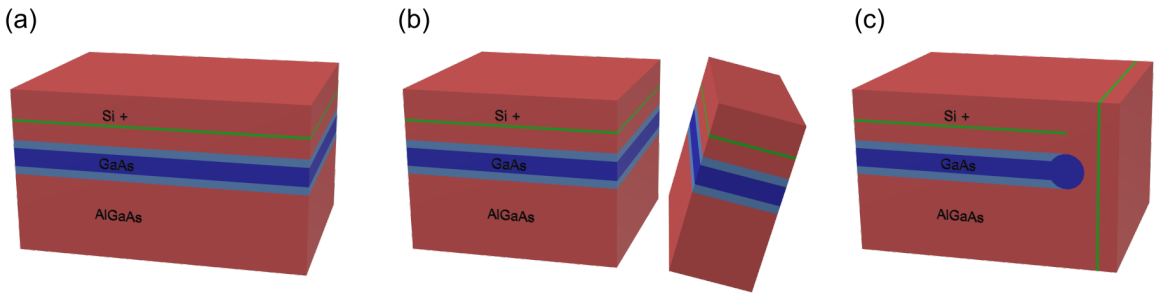

Figure 1: (a) Regular 2DEG grows on the (100) substrate surface. (b) Cleave process inside the MBE chamber. (c) Overgrowth of AlGaAs and side dopants (green) on the (110) surface.

The differential conductance of CEO wires shows clear plateaus as a function of the gate voltage for wire lengths up to $10\,\mu$m [2], suggesting that the transport mean free path exceeds $10\,\mu$m. This also indicates a lack of backscattering or mode mixing inside the quantum wire and confirms the exceptional quality of the wires fabricated using this technique. The energy splitting between the lowest two eigenstates of $\approx 20\,$meV

was obtained from the evolution of conductance plateaus as a function of magnetic filed applied in the plane of the 2DEG. For the comparison, the subband separation of the surface-gate defined wires is of the order of $\approx 1\,\mathrm{meV}$.

1.1.2 Non-universal conductance quantization

In the publication by A. Yacoby [2], it was pointed out that the conductance of the last wire mode $G = 1.8e^2/h$ is lower than expected $2e^2/h$. This reduction was observed in all samples and was the same in all the devices fabricated from the same quantum well material, confirming that this deviation is not an artifact of wire the fabrication process. As the temperature rises up from 300 mK, conductance also goes up and saturates at the conductance quantum of $2e^2/h$ [2]. Some samples were also equipped with a side gate evaporated after the overgrowth onto the cleaved plane. A voltage applied to this gate controls the density of electrons in the wire. Measurements involving this side gate reveal that the conductance plateaus are independent of wire density. It is also important to mention that the value of conductance at the last plateau did not show the saturation behavior as a function of temperature down to the lowest accessible temperature of 300 mK.

To describe this reduction, three different theoretical models were suggested. In the first model, electrons are assumed to be non-interacting both in the wire and in the 2DEG contacts. In this case, conductance can be calculated using Landauer's formula and, for a transmission probability of one, will give $G = NG_0$. Reduced conductance in this case can be explained by non-ideal electron transmission. The voltage applied to the gate locally tunes the Fermi energy of the wire, so the plateaus indicate that the transmission probability is energy independent, which is very unlikely to be the case. For non-interacting theories, energy-independent transmission probability should also be temperature independent, which clearly contradicts the experiment.

The second model assumes the presence of e-e interactions in the finite-length wire, coupled to the non-interacting Fermi liquid leads. Conductance through such a system

without disorder was theoretically studied in [3–5], and was predicted to be independent of the strength of e-e interactions and equal to $2e^2/h$ for a singe mode quantum wire. To explain the reduction of the conductance, one has to include the presence of disorder in the wire. This situation was studied theoretically and experimentally by Maslov [6] and Tarucha et al. [7], respectively. The power-law decrease of the conductance was observed experimentally as temperature was lowered. The strength of the e-e interaction depends strongly on the electron density, so, for Maslov's theory, conductance should also be side gate voltage dependent. This is in contradiction with the observation of the long conductance plateau with the conductance value independent of the side gate voltage.

The third model considers the competition between the scattering from the 2DEG to the edge modes and backscattering inside the wires. Momenta of the 2DEG states and edge modes at the Fermi level are very different, so impurities have to be involved in the process of transferring electrons from the 2DEG to the wire to accommodate the momentum mismatch. Conductance derived from the steady-state Boltzmann equations for the left- and right-moving electrons is $G = G_0/\sqrt{1 + 2\Gamma_{BS}/\Gamma_{2D}}$, where Γ_{2D} is the scattering rate per unit length between the 2DEG and either the right- of left-movers in the edge mode, and Γ_{BS} is the backscattering rate per unit length in the edge mode. The conductance of the system is lower than the conductance quantum and approaches it as the backscattering Γ_{BS} rate is reduced. The presence of e-e interactions in the 1D system can be described using the Luttinger liquid theory, which predicts an increased backscattering rate at low temperature. The scattering rate Γ_{2D} is suppressed at low temperatures due to the vanishing of the tunneling density of states. Both these facts lead to the reduction of the conductance at low temperature that was observed experimentally. For this model, the reduction of the conductance is not caused by the interactions inside the wire region, so, therefore, should be independent of the wire density, which was also confirmed by measurement. At the same time, conductance should also be wire length independent, which is in contradiction with experiment. In

the limit $T \to 0$, the Luttinger liquid theory predicts that $\Gamma_{2D} \to 0$, so for this model conductance should also vanish ($G \to 0$). In conclusion, both interacting and non-interacting models were incapable of explaining the observed conductance reduction measured down to $T = 300\,\mathrm{mK}$.

1.1.3 Evidence for Helical Nuclear Spin Order

Similar CEO wires were also studied by Scheller et al. [8]. It was shown that the conductance plateau of the last wire mode reaches $2e^2/h$ for $T \geq 10\mathrm{K}$, as expected for a spin-degenerate single-mode wire. The remaining question was how conductance behaves below 300 mK. To answer this question, Scheller et al. used specially-designed microwave filters and thermalizers [9] to lower electron temperatures in the CEO wire sample far below 100 mK. The wire conductance (g), measured as a function of the gate voltage (V_g) at different temperatures, is shown in Fig.2a. The height of the last conductance step δg is depicted on Fig.2b with a logarithmic temperature scale (linear scale in the inset). It clearly shows that the wire conductance saturates at $1e^2/h$ below $T \approx 100\,\mathrm{mK}$. This conductance reduction from $2e^2/h$ to $1e^2/h$ was observed in all available wires and, therefore, can not be explained as a sample specific phenomena.

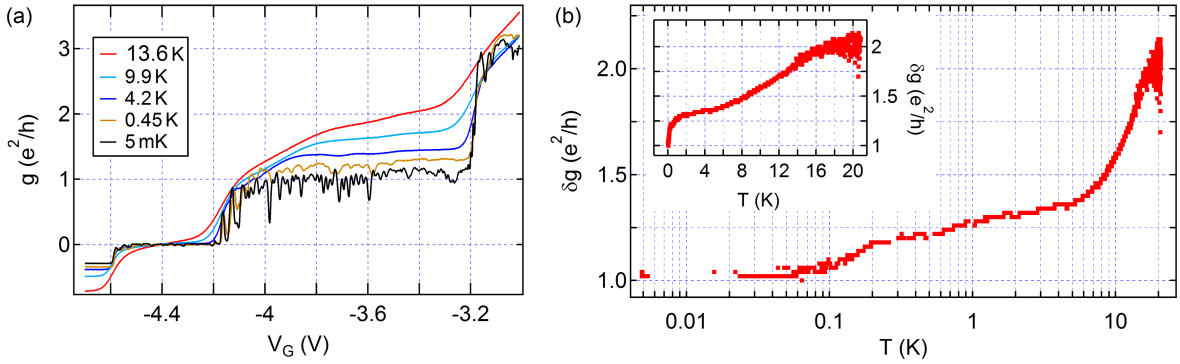

Figure 2: (a) Conductance of the double-wire sample as a function of the gate voltage measured at different temperatures. (b) Upper wire conductance step height as a function of temperature (adopted from [8]).

It was also shown that the conductance saturation was not caused by inability to cool electrons in the sample below $100\,mK$. The temperature extracted from the thermal activation of fractional quantum Hall states measured in the same device gave

an upper bound on the electron temperature of $27\,mK$, clearly below $100\,mK$. The electron temperature measured using metallic Coulomb blockade thermometers in the same refrigerator was reported to be $10.5 \pm 0.5\,mK$. The conductance through the last wire mode rises quickly as the magnitude of the bias voltage is increased and, for bias voltage $V_{SD} > 1\,mV$, approaches $2e^2/h$. This increase was attributed to resistive heating that raises locally electron temperature. Careful reexamination of all previously suggested models lead to the conclusion that only a recent theory by Braunecker, Simon, and Loss [10–12] can explain the observed reduction by a factor of 2 and subsequent saturation of the conductance for $T \lesssim 100\,mK$.

This theory predicts a helical nuclear spin ordering in the system with strong e-e interactions. Below a certain crossover temperature T^*, determined by the strength of e-e interactions, the nuclear spins transition to a new state of matter, and form a spiral or helimagnet. The ordering is caused by the effective RKKY (Ruderman-Kittel-Kasya-Yoshida) interaction between distant nuclear spins, mediated by strongly interacting electrons. The ordered nuclear spins generate an Overhauser field that acts on the electrons in the wire and opens gaps in the electron dispersion relation. This leads to partial electron spin polarization and freezes out one half of the conducting channels, which directly results in a two-fold reduction of the electrical conductance. The remaining gapless electron modes further strengthen coupling between nuclear spins, which closes the feedback loop. This feedback mechanism strongly increases the transition temperature T^*. The Luttinger liquid interaction parameter for the CEO wires made out of GaAs heterostructure was estimated to be as low as $g_c = 0.3-0.4$ [13]. For such a string e-e interactions the transition temperature T^* lies in the range of $200 - 600\,mK$, and is in qualitative agreement with the temperature, below which measured conductance saturated at e^2/h. The initial goal of this thesis was to observe gapped branches of the electron dispersion relation using tunneling spectroscopy.

1.1.4 Resonant tunneling in a Luttinger Liquid

Even though the Luttinger liquid is a well established theory that can be used to describe low-temperature transport properties of interacting electrons in quantum wires, only few experiments were able to extract important theory parameters. One of such parameters is the strength of e-e interactions $g_c \approx 1/\sqrt{1+U/2E_F}$, where U is the energy of Coulomb interaction between electrons and E_F is the Fermi energy of electrons in the wire. From this formula the interaction strength $g_c = 1$ for non-interacting electrons, and $0 < g_c < 1$ in the case of repulsive Coulomb interaction, so smaller values of g_c correspond to stronger interactions. One possible way to measure the strength of e-e interactions in CEO wires was shown by Auslaender et al. [14]. The Fermi energy in the wire is controlled using the surface gate and can be lowered to the point where the disorder potential exceeds the chemical potential in several places along the wire. This leads to the formation of tunnel-coupled 1D islands along the wire that show signatures of resonant tunneling in the conductance measurements. For current to flow at small DC bias through the chain of quantum dots, energy levels in all islands have to be aligned to the chemical potential of the source or drain. This is very unlikely to happen if the number of islands is larger than one. This suggests that the observed sharp resonances prior to complete conductance suppression can be attributed to Coulomb blockade resonances in a single 1D island. For even more negative gate voltages, additional islands will form and, as a result, electron transport will be completely blocked.

The conductance through the single quantum dot coupled to the Fermi-liquid leads can be described using the Landauer formula. In the temperature-broadened regime $k_BT \gg \Gamma_i$, with k_B the Boltzmann constant, T the temperature and Γ_i the energy level broadening, it is $G_{FL} = \frac{e^2}{h}\,\Gamma_i\,\frac{\pi}{4k_BT}\cosh^{-2}\left(\frac{\varepsilon_0-\mu}{2k_BT}\right)$, where μ is the chemical potential in the leads and ε_0 is the center of the resonance [15]. It can be shown that the area under the curve is proportional to Γ_i. In the conventional Coulomb blockade theory, Γ_i is given by the transparency of the barriers, and is temperature independent, so the

area under the resonance peak should also be temperature independent.

The picture will be different for a quantum dot connected to the Luttinger liquid leads. It was shown by Furusaki [16] that $\Gamma_i \propto T^{(1/g_c)-1}$, and should drop as a power of temperature. The value of g_c extracted for last two resonances are 0.82 and 0.74, and qualitatively agree with the fact that interaction strength should increase upon reduction of electron density in the wire. The finite bias spectroscopy confirms that contributions from the excited states to the conductance can be neglected for the temperature range studied in the experiment.

The strength of e-e interactions $g_c \approx 1/\sqrt{1 + U_c/\Delta E}$ can be also extracted from the level spacing ΔE and the charging energy U_c of the quantum dot [17]. This method gives $g_c \approx 0.4$, which is quite different from the value obtained in transport measurements. This disagreement was studied by Kleimann et al. [18], who concluded that these two methods probe the interaction strength in different regions of the 1D wire. The temperature dependence of the intrinsic level broadening is sensitive to the interaction strength along the source and drain leads, while the interaction strength extracted using excited-state spectroscopy gives the strength of interactions inside the island itself.

Measured power law behavior confirms that quantum wires fabricated using the CEO technique behave according to Luttinger-liquid theory with the e-e interaction strength parameter g_c ranging from 0.82 to 0.66.

1.2 Tunneling spectroscopy

The work presented in this thesis heavily relies on the tunneling spectroscopy that was developed by Auslaender et al. [19]. This type of spectroscopy is based on the fact that energy and momentum along the wire are conserved during the event of electron tunneling between two parallel wires. This allows one to directly measure the dispersion relation of electrons in the wires. In our work we use this technique to

study the evolution of the integer quantum Hall edge-state momentum as a function of magnetic fields applied perpendicular to the 2DEG.

1.2.1 Elementary Excitations in a One-Dimensional Wire

It has been known for a long time, that the motion of electrons in 1D wires can not be described using a single-particle theory, which works nicely in two and three dimensions. Instead, the description has to be based on the collective motion of all the electrons present in the 1D wire [20]. This collective motion can be grouped into collective spin modes and collective charge modes, which propagate with velocities v_p and v_s respectively. Due to the Coulomb interaction between electrons U, the charge mode velocity will be strongly modified compared to the non-interacting case: $v_p = v_F/g_c$, where $g_c \approx 1/\sqrt{1 + U/2E_F}$ is the strength of e-e interactions, v_F and E_F are the Fermi velocity and Fermi energy respectively.

Despite the strong modification of the excitation spectrum of the wire in the presence of e-e interactions, the conductance through the clean wire is predicted to be the same as in the non-interacting case. This makes it difficult do detect signatures of strong e-e interactions in the clean wires using regular transport measurements. The presence of impurities in the wire can reveal some information about interactions and was discussed in the previous chapter. Unfortunately, the lack of control over the disorder potential generated by impurities makes it difficult to control the system and interpret experimental results.

Alternatively, one can directly study the excitation spectrum of interacting wires. One possible way to do this is to use Raman spectroscopy. Unfortunately, this spectroscopy technique can only excite states with very low momenta. Auslaender et al. tackled the problem using a different approach [19]. To study the dispersion relation of electrons in the 1D interacting wire, they designed samples with a special geometry. The schematic of the sample is shown in Fig.3

The sample consists of two parallel tunnel-coupled quantum wires fabricated using the

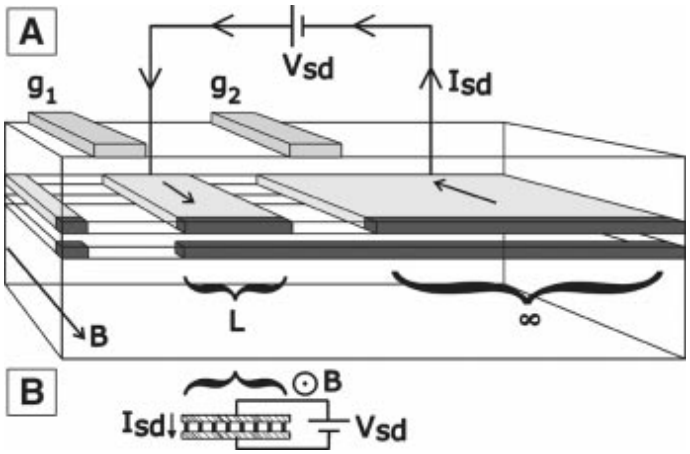

Figure 3: A double wire sample schematic (taken from [19]).

CEO technique. To fabricate such a device, a GaAs/AlGaAs double quantum well heterostructure with prefabricated surface gates is cleaved inside the MBE chamber. The fresh surface is immediately overgrown with another modulation doping sequence. There are two types of doping incorporated during the sample fabrication. First, a layer of silicon dopants is placed during the initial heterostructure growth and is located above the upper quantum well. This lead to the formation of a two-dimensional electron gas only in the upper quantum well. Second, an additional layer of dopants is incorporated during the overgrowth process, and generates a triangular electrostatic potential in the direction perpendicular to the cleavage plane. Electrons trapped in this confinement potential form 1D wire modes along the entire edge of the sample in both the upper and lower quantum wells. The 2DEG in the upper quantum well is in direct contact with the upper quantum wire and is used to contact the upper wire with ohmic contacts. The lower quantum wire is separated from the upper 2DEG and the upper wire by a 6 nm AlGaAs barrier and, thus, is only tunnel-coupled.

A long mean free path of electrons in the quantum wires assures that momentum along the wire is a good quantum number, meaning it is conserved during the tunneling process between the two wires. The magnetic field B applied perpendicular to the plane spanned by the wires gives an extra momentum kick $k_B = eBd/\hbar$, where e is the electron charge, d is the distance between the centers of the upper and lower wires, and $\hbar$ is the reduced Planck's constant. Control over the momentum kick using an in-

plane magnetic field is a key component of this tunneling spectroscopy.

The surface gates control the local electron density in sections of the 2DEG, and the upper and lower wires located directly beneath the gate. The first step to perform dispersion relation spectroscopy is to tune the double wire system into the tunneling regime, shown in Fig.3. To accomplish this, the surface gate g_2 is negatively biased to the point where the 2DEG and the upper wire are completely depleted beneath the gate. In this state, electrons have to tunnel twice to go from the source ohmic contact to the drain. Electrons enter the 2DEG at the source ohmic contact, propagate through the 2DEG, tunnel from the 2DEG or upper wire to the lower wire, propagate along the lower wire and tunnel back up on the other side of the gate g_2. The finite DC voltage bias between source and drain controls the energy transfer during the tunneling event. To simplify the interpretation of the experimental results, the left tunnel junction is made much more resistive than the right one. This is done by pinching both the upper and lower wires using a neighboring gate g_1, which makes the left tunneling junction much shorter and, correspondingly, much more resistive than the right junction. In this configuration, the DC voltage V_{sd} applied between source and drain will drop across the more resistive short junction and will provide an energy boost to the tunneling electrons.

The conservation of energy and momentum during the tunneling process from upper wire mode i to lower wire mode j in the presence of finite magnetic field B and finite source-drain voltage V_{sd} can be written as $E_{U_i}(k - k_B) = E_{L_j}(k) - eV_{sd}$, where $E_{U_i}(k)$ and $E_{L_j}(k)$ are the dispersion relations of the upper wire mode i and lower wire mode j, respectively. Additionally, tunneling can only take place if states are occupied in one wire and empty in another wire.

Assuming a parabolic dispersion relation for electrons in the upper and lower wires, the tunneling can only takes place in the regions highlighted in gray in Figure 4B. There are a couple of special points on this diagram. For example, at $B = 0$, tunneling can only happen for one particular value of bias voltage $V^*_{sd} = \left(E_{F,L_j} - E_{F,U_i}\right)/e$, where E_{F,L_j}

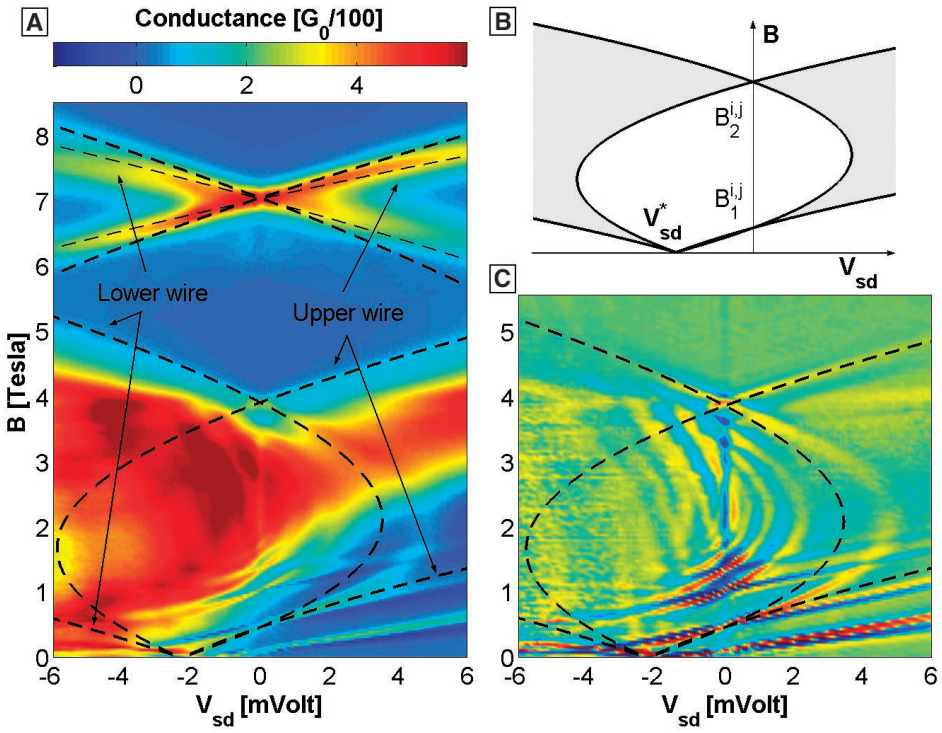

Figure 4: (A) Differential tunneling conductance as a function of bias voltage V_{sd} and magnetic field B. (B) A schematic with the regions of zero and non-zero tunneling currents depicted in wight and gray, respectively. (C) The section of panel (A) after subtracting a smoothly varying background [19].

and E_{F,U_i} are the Fermi energy of electrons in upper and lower wires respectively. This bias voltage shifts the upper wire dispersion vertically and is necessary to compensate for the density mismatch between two wires. For any other bias voltages the two dispersions do not cross each other, so the tunneling is completely suppressed. The further special points are $B_1^{i,j}$ and $B_2^{i,j}$ with $V_{sd} = 0$. The small magnetic field $B_1^{i,j}$ is necessary to match two co-propagating Fermi points of the upper and lower wires. The large magnetic field $B_2^{i,j}$ shifts the dispersion horizontally to such an extent, that two counter-propagating Fermi points coincides. For such a high magnetic field, an electron originally moving to the left in the upper wire moves to the right after tunneling into the lower wire.

In low temperature experiments it is quite common to use a lock-in amplifier to perform electrical measurements, due to the good signal to noise ratio obtained through this type of measurement. For this experiment, a small reference oscillation from the lock-in was superimposed with the DC voltage V_{sd}, and the resulting voltage was applied

to the source ohmic contact. The current flowing from the drain contact was sent to the input of the lock-in amplifier. A lock-in amplifier is only sensitive to the AC component of the incoming signal with frequency exactly equal to the frequency of the reference oscillation. In this case, the lock-in is measuring differential conductance, which is equal to the derivative of the tunneling current with respect to the applied source-drain voltage. The map of differential conductance measured for different values of magnetic field B and source-drain voltage V_{sd} is shown in Figure 4A.

The differential conductance is equal to zero in the regions of the B vs V_{sd} plane where tunneling is suppressed and is also small in the regions with almost constant current. It is only large along the curves that separate regions of high and low currents. These curves are given by the dispersion relations of the upper and lower wires (solid black in Figure 4B), so the tunneling conductance can be used to directly image the dispersion relations of elementary excitations in the 1D wires.

The dispersion relations calculated using a non-interacting model are shown as thick dashed lines in Figure 4A and C. It is clear that this model does not describe the data well. The measured dispersions can be fitted successfully only once the mass in a non-interacting model is renormalized to m^* with $m^* = 0.75\,m$, where m is the effective mass of electrons in GaAs. This suggests, that due to the interactions, collective excitations in the wire possess a different effective mass compared to non-interacting electrons. At the same time, the velocity of these collective excitations are also renormalzied: $v_p/v_F = m/m^*$, where v_F is the Fermi velocity of non-interacting electrons. In the case of a weak inter-wire coupling, Luttinger-liquid theory predicts that the velocity of excitations is $v_p = v_F/g_c$, where g_c is the e-e interaction strength that, together with the previous equation, yields $g_c = 0.75$. In conclusion, it was shown that momentum resolved tunneling spectroscopy is a perfect tool to study dispersion relations of collective excitations present in CEO wires due to strong e-e interactions.

1.2.2 Spin-Charge separation in one dimension

As already mentioned in the previous section, Coulomb interactions in 1D conductors lead to completely different excitation spectra than in two- or three-dimensions. The elementary excitations in 1D are the collective and highly correlated motion of all electrons present in the wire. These excitations carry either spin or charge and can be described using Luttinger liquid theory. Auslaender et al. [21] used momentum resolved tunneling spectroscopy to measure the velocities of the spin and charge excitations in CEO wires, and showed how these velocities are modified by the changes in electron density that directly controls the strength of e-e interactions.

The tunneling rate between the two wires depends on how easy it is to take an electron from one wire and add it to the other wire. At low temperatures and small interwire bias voltages, tunneling between two quantum wires can only happen in the vicinity of the Fermi points with the momenta $k_F = \pm\pi n/2$, where n is the 1D wire electron density. The Fermi momenta are not exactly the same in the upper and lower wires due to a small difference in the electron density between two wires. To obtain high tunneling currents, one of the Fermi points of the upper wire has to be aligned with one of the Fermi points of the lower wire. This can be done by applying an in-plane magnetic field $B_\pm = \hbar|k_{FU} \pm k_{FL}|/ed$, where d is the center to center distance between the upper and lower wires. This magnetic field compensates for the momentum mismatch. For magnetic fields B_-, the left moving electrons in the upper wire are momentum matched with the left moving electrons in the lower wire. Similarly, for $-B_-$, right moving electrons from the upper wire after the tunneling event have the same momenta as the right moving electrons at the Fermi level in the lower wire. The strong magnetic field $\pm B_+$ is necessary to match the counter-propagating electrons in the upper and lower wires.

For weak interwire interactions, the tunneling rate is proportional to the convolution of electronic spectral functions $A_{k,E}$ in the upper and lower wires. In the absence of e-e interactions, $A_{k,E} = 2\pi\delta(E - E(k))$, where $E(k)$ is the electron dispersion relation.

This singly-peaked function is typical for systems with non-interacting quasiparticles. In this case, the tunneling spectroscopy directly images the dispersion relations of quasiparticles (electrons with usual charge and spin and effective mass of GaAs) in the upper and lower wires.

In the case of strong e-e interactions the single quasiparticle peak is replaced by a double-peak structure, characteristic for Luttinger liquids. These two peaks correspond to the charge- and spin-density excitations. As was explained earlier, the momentum- and energy-resolved tunneling spectroscopy can only be performed in the sample with two tunnel-coupled quantum wires. For strong intra-wire interactions and small interwire interactions, tunneling spectroscopy reveals a pair of resonances for the upper and lower wires, which directly correspond to the spin- and charge-excitations in these wires.

For the CEO double wire sample studied in Ref. [21], intra- and inter-wire interactions can be estimated using the following equations: $V_{UU} \approx V_{LL} \approx (2e^2/\epsilon) ln(2\lambda_s/W)$ and $V_{UL} \approx (2e^2/\epsilon) ln(\lambda_s/d)$, respectively. Here ϵ is the wire's (GaAs) dielectric constant, W is the width of the wire mode and λ_s is the 2D screening length [22]. Substituting the experimental parameters into these formulas results in an inter-wire interaction that is comparable to the intra-wire interaction. In this case, the resonant tunneling does not probe the spin- and charge-excitations of upper and lower wires. Instead, the excitation spectrum of the coupled system is measured.

Using Luttinger liquid theory, Carpentier et al. [22] calculated the differential tunneling conductance for a system of coupled wires with strong intra- and inter-wire interactions. Figure 5 shows the calculated tunneling conductance around the point with the strong in-plane magnetic field B_+ that brings the counter propagating states into resonance.

The theory predicts a presence of six lines (white dashed lines on Fig. 5), along which differential conductance behaves non-analytically. Each quadrant has two lines that correspond to collective charge excitations with the velocity magnitudes v_{c1} and v_{c2}, and one line related to spin excitations with velocity of either v_{s1} or v_{s2}. The value

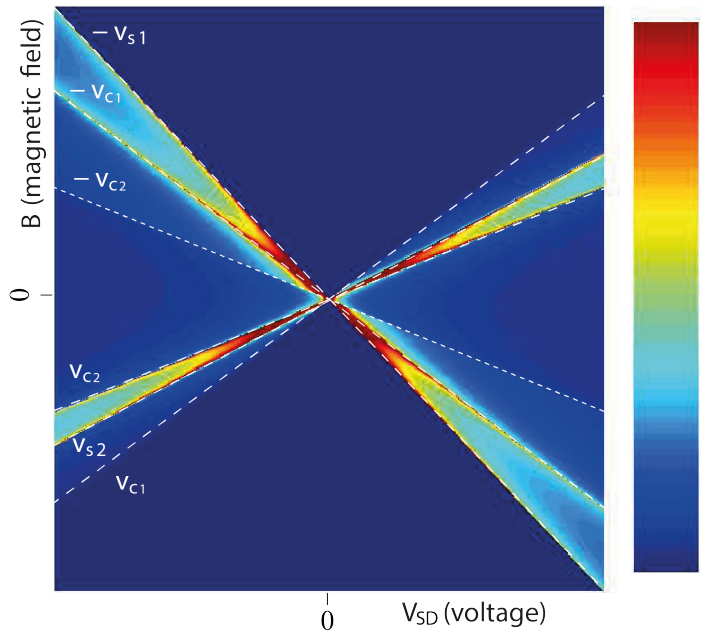

Figure 5: Calculated differential tunneling conductance as a function of in-plane magnetic field (vertical axes) and bias voltage (horizontal axes). The origin of the vertical axes corresponds to the magnetic field that brings counter-propagating Fermi points in the upper and lower wires into resonance at zero bias voltage (taken from [22]).

of the velocity is related to the slope of the line and can be calculated using the following equation: $v = d^{-1}(\partial B/\partial V_{SD})^{-1}_{V_{SD}=0}$. In the case of Fig. 5 velocities satisfy an inequality: $v_{s1}, v_{s2} < v_{c1} < v_{c2}$.

Experimental observation of the lines with different velocities directly confirms the presence of collective spin and charge excitations in the system. For the CEO double wires the presence of these lines was reported by Auslaender et al. [21].

The tunneling spectroscopy discussed in the previous section utilizes two gates to define the tunneling region across which the source-drain voltage drops. An additional gate placed between theses two gates can be used to control electron density in the upper and lower wires in the tunneling region. In this case, tunneling happens both in the region underneath the gate and in two adjacent ungated regions. To be predominantly sensitive to the tunneling events happening in the gated region, a small AC voltage was added to the DC voltage V_G that was applied to the central gate. The resultant oscillating component of the tunneling current was measured using stan-

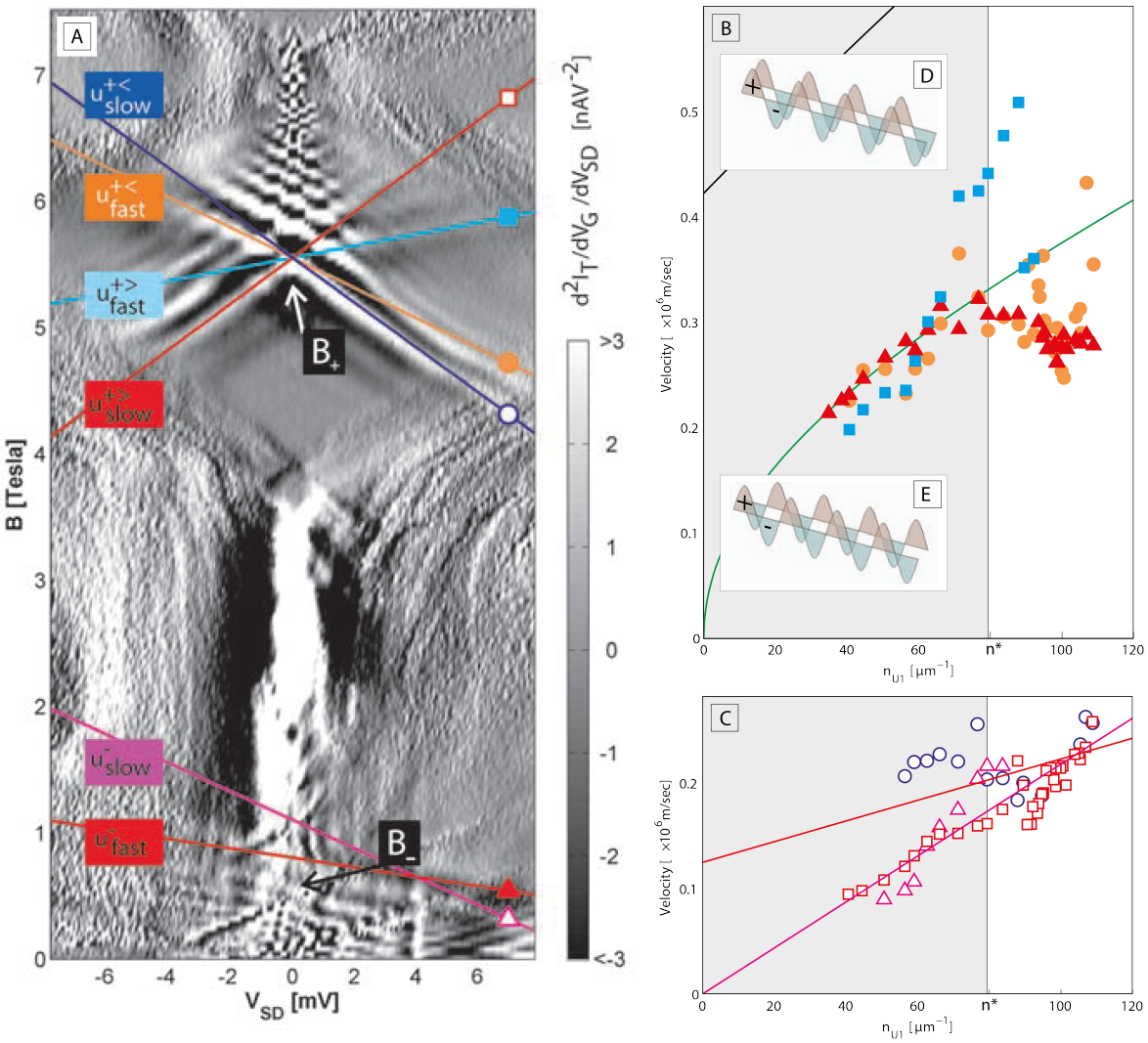

Figure 6: (A) Numerical derivative with respect to B of the measured trans-conductance $\partial I_T(V_{SD}, B)/\partial V_G$ as a function of magnetic field and bias voltage for one value of the gate voltage V_G. Changes in electron density influence the e-e interaction strings that determine the charge and spin excitation velocities. Different slopes are marked with colored lines. (B and C) Charge- and spin- excitation velocities, respectively, corrected to the band-filling effects as a function of the upper wire density. (D and E) Symmetric and antisymmetric charge excitations of the interacting upper and lower wires (taken from [21]).

dard lock-in techniques. Panel A in Fig.6 depicts typical tunneling trans-conductance $\partial I_T(V_{SD}, B)/\partial V_G$ differentiated along the magnetic field direction for clarity. Similar measurements were repeated for different values of the gate voltage V_G that controls electron density and, correspondingly, the strength of e-e interactions in the upper and lower wires.

Out of six theoretically predicted slopes, four were observed and highlighted using colored lines around the counter-propagating resonance point B_+. For the magnetic field

B_-, which brings co-propagating states into resonance, theory predicts the presence of four different slopes, two of which were experimentally observed (u^-_{slow} and u^-_{fast}).

Theoretically calculated velocities of the symmetric and antisymmetric charge excitations in a double wire system are shown in Fig.6B as black and green curves, respectively. Velocities of the excitations labeled with the subscript 'fast' in panel A after correction for the band-filling effect [23], closely follow the green curve for the range of densities $n_{U1} < n^*$ (shaded region), where only the lowest mode is occupied in the upper and lower wires. This leads to the conclusion that excitations labeled with filled circles, triangles and squares correspond to antisymmetric charge modes.

The data is completely absent for the faster charge excitations that correspond to the symmetric mode. This is expected near B_-, where tunneling processes produce asymmetric electron-hole excitations that propagate in the same direction. The question remains open, however, why symmetric excitations are completely absent near magnetic field B_+, as it is expected that in this case both symmetric and antisymmetric excitations should be present. Schematic illustrations of symmetric and antisymmetric excitations of upper and lower wires are shown on Fig.6D and E. Excess positive and negative charges for these two modes are marked with $''+''$ and $''-''$.

The velocities of the resonant rays labeled with the subscript 'slow' on Fig.6A, after correction for band-filling effects, are depicted in Fig.6C, and show a linear dependence on density and the bare Fermi velocity in the upper (magenta line $v_{sU} = v_{FU}/1.25$) and lower wires (red line $v_{sL} = v_{FL}/1.25$). Here v_{FU} is the upper wire Fermi velocity and v_{FL} is the lower wire Fermi velocity. A linear dependency and a coefficient in the denominator larger than one are expected for decoupled spin modes in upper and lower wires in the presence of back-scattering.

In conclusion, momentum resolved tunneling spectroscopy reveals the presence of decoupled spin and charge excitations in the tunnel coupled CEO quantum wires. These excitations propagate with velocities that are controlled by the strength of e-e interactions and can be described using Luttinger liquid theory.

1.2.3 Charge fractionalization

Luttinger-liquid theory also predicts that quantum wires with strong e-e interactions should carry excitations with a charge that is smaller than that of the free electron charge e. The first experimental evidence for charge fractionalization was observed in CEO quantum wires by Steinberg et al. [13].

An electron that tunnels into an interacting wire splits into the co- and counter-propagating charge excitations that carry the fractional charges fe and $(1-f)e$. Here f is a charge fraction that depends on the strength of e-e interactions g_c and is given by

$$f = (1 + g_c)/2 \tag{1}$$

For non-interacting electrons $g_c = 1$ and charge fractionalization is absent, so $f = 1$, meaning that after the tunneling electron only excites the co-propagating charge excitation. In the interacting case $g_c < 1$ and as a consequence $f < 1$, so after tunneling only the fraction $f \cdot e$ of the electron charge propagates in the same direction as the original electron and the rest of the charge $(1 - f)e$ is transferred into the counter-propagating charge excitation.

Different experiments were proposed to test the presence of this charge fractionalization. For example, studying high-frequency noise correlations [24], shot noise due to an impurity [25], or multi-terminal conductance measurements involving bulk contacts [26] all should reveal the presence of fractionalized charges. Steinberg et al. [13] utilized a different method that relies on the asymmetry between co- and counter-propagating currents induced by tunneling electrons in the double wire sample. To realize this experimentally, the surface gates were tuned into the regime where the upper wire was split into three sections: a short section ($10\,\mu m$) in the middle labeled source and two semi-infinite ($\approx 2\,mm$) drain sections to the left and to the right of the source. This was achieved with the surface gate voltages negative enough to deplete the 2DEG and upper wire but too small to deplete the lower wire. In such a way, the lower wire was

kept electrically connected along the entire edge of the sample.

The influence of an in-plane magnetic field B applied perpendicular to the wires on the relative position of the upper and lower wire dispersions was discussed in detail in the previous sections. Figure 7b shows typical differential tunneling conductance traces measured at zero DC bias voltage as a function of in-plane magnetic field B for the left and right drain contacts.

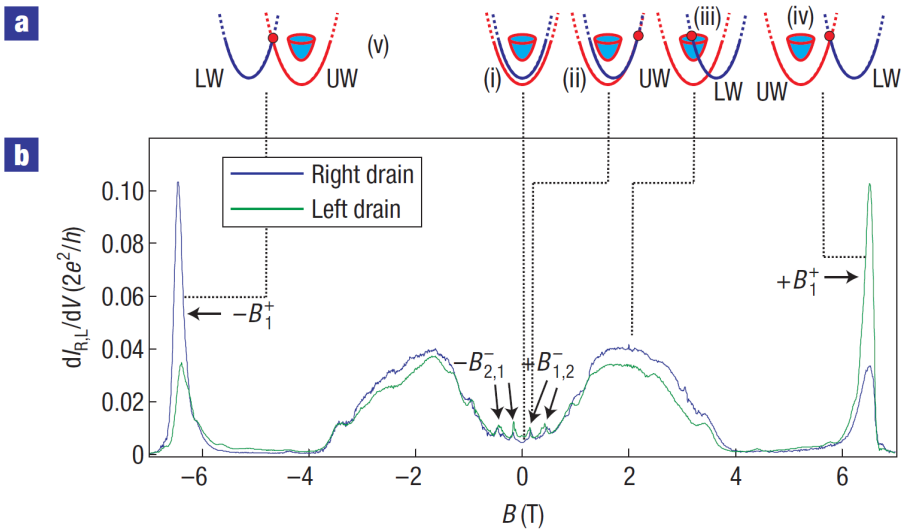

Figure 7: (a) Schematic illustration of the dispersion relations of the lowest mode in the upper wire (red), the 2DEG (paraboloid) and the lowest mode in the lower wire (blue) for different values of magnetic field B. (b) Differential conductance measured using right and left drain contacts as a function of the in-plane magnetic field (taken from [13]).

In the absence of e-e interactions at the magnetic field $+B_1^+$, right moving electrons from the upper wire end up moving to the left in the lower wire after tunneling. This leads to the higher conductance value measured with the left drain compared to the value measured using the right drain. A parameter $AS = (I_R - I_L)/(I_R + I_L)$ can be used to characterize the asymmetry between the left and the right drains.

Upon the tunneling event in the interacting wire, the electron charge is carried by two charge excitations, one propagating towards the left drain and another propagating towards the right drain. The finite backscattering in the wires and complicated process of coupling the interacting upper wire to the non-interacting 2DEG results in a more even distribution of the right- and left-moving charge excitations, which suppresses AS. The two terminal conductance G_{2T} measured between left and right drain can be

used to distinguish the charge fractionalization effect from these microscopic effects.

According to the Luttinger-liquid theory, the left- and right-moving electrons in the lower wire can have different chemical potentials. Using transmission probability β to characterize the tunnel-coupling between the upper and lower wires in the drain regions, it can by shown that $G_{2T} = g_c G_0 \beta/(2-\beta)$. In a similar way, the asymmetry parameter AS can be also expressed using β and f: $AS = (2f-1)\cdot\beta/(2-\beta)$. These equations have a similar factor $\beta/(2-\beta)$ that cancels out in the ratio

$$\frac{G_{2T}[G_0]}{AS} = \frac{g_c}{2f-1} \tag{2}$$

Here G_{2T} is expressed in units of G_0. This equation gives a direct way to extract the charge fractionalization parameter f using experimentally measurable quantities G_{2T} and AS, once g_c is known. It was shown in the previous section that the velocity of the charge excitations $v_c = v_F/g_c$ directly depends on g_c. From this equation e-e interaction strength is given by the ratio between the Fermi velocity v_F, which can be calculated from known electron density, and charge mode velocity v_c, that can be measured using tunneling spectroscopy. All these measurements were performed for different values of lower wire density that was tuned by side gate voltage or by illuminating the sample with light. The calculated value of the interaction parameter for the studied density range was found to be in the range $0.4 < g_c < 0.5$, consistent with the theoretical model from ref.[21]. In this case, the interaction strength was measured in an ungated section of the wire, where several modes and proximal 2DEG are present and screen the interactions. This weakens the interactions compared to the values measured using the resonant tunneling method or spectroscopy in the region under the gate, in which only the last wire mode is occupied. In addition, it turns out that the asymmetry parameter AS the and two-terminal conductance G_{2T} closely match each other for different values of lower wire density, so $AS = G_{2T}[G_0]$. Substituting this into equation (2) gives $(2f-1) = g_c$, which is equivalent to equation (1) obtained from the Luttinger-liquid theory. This results in the fractionalization ratios in the range of $0.7 < f < 0.75$.

1.3 Landau Level edge states

After the discovery of the topological insulator, a lot of attention was drawn towards the edge states that play the key role in the electrical transport properties of these materials. Additionally, a recent proposal by Bosco and DiVincenzo [27] suggests coupling qubits in a quantum computer using transmission lines [28] and resonators based on quantum Hall edge states.

The quantum Hall effect was the first system discovered with a non-trivial topology, and was realized in a two-dimensional conductor placed in a perpendicular magnetic field. Observation of Hall conductance quantized in integer multiples of e^2/h was reported by Klaus von Klitzing et al.[29] and was distinguished with the Nobel Prize in Physics in 1985. The original discovery was made using a MOSFET (metal-oxide-semiconductor-field-effect transistor) device with a 2DEG accumulated in the inversion layer formed at the Si/SiO_2 interface. The quality of the 2DEG, which can be characterized by the electron mobility, controls the width of the observed conductance plateaus. Mobility in the Si/SiO_2 devices is limited by impurities and disorder located close to the inversion layer. The strong magnetic field $B \approx 15\,\mathrm{T}$ and low temperature $T \approx 1.5\,\mathrm{K}$ were necessary to observe conductance quantization in such devices. Soon after, Tsui and Gossard [30] showed that conductance quantization can be observed at much lower magnetic fields $B \approx 4\,\mathrm{T}$ and at higher temperatures $T \approx 4\,\mathrm{K}$ for 2DEGs formed in GaAs/AlGaAs heterostructures, which can have substantially higher mobility. Partially, this is due to high similarity between the lattice constants of these two semiconductors. Another important factor is an ability to separate conduction electrons from their donor atoms by using so-called modulation-doping technique. Ability to grow 2DEGs with exceptionally high mobilities lead to the discovery of the fractional quantum Hall effect [31], with states that are formed due to strong e-e interactions in the 2DEG.

In a theoretical study, Halperin [32] showed that a 2DEG confined in an annular geom-

etry placed in a perpendicular magnetic field should host quasi-one-dimensional states at the perimeter of the sample. These delocalized states carry a current and are protected against a disorder potential of moderate strength. Later, the presence of these edge states was also confirmed by numerical tight-binding simulations [33].

A more elaborate theory of the edge states for a 2DEG confined with a soft confinement potential (Fig.8a,b) was proposed by Chklovskii et al. [34]. This theory includes a self-consistent electrostatic potential and predicts the formation of alternating strips of compressible, partially field circles in Fig.8a, and incompressible electron liquids along the entire circumference of the 2DEG. The main assumption of this theory is that the screening length is much shorter than all other length scales of the system.

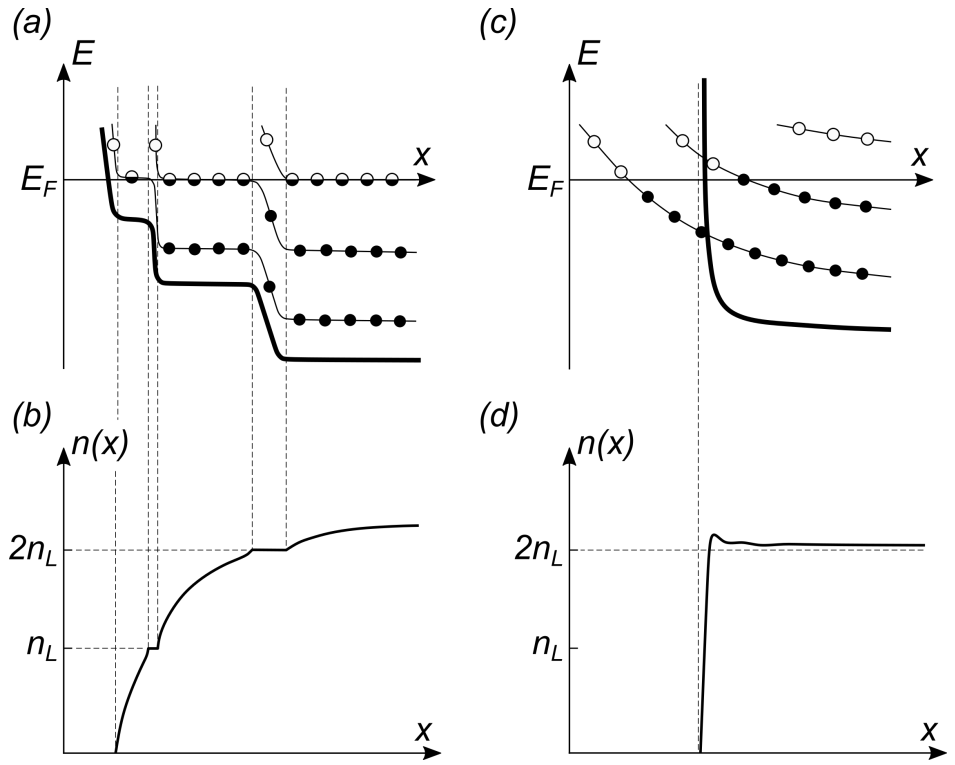

Figure 8: (a), (c) Bending of the Landau levels close to the sample edge for soft and steep confinement potentials, respectively. Solid, partially colored and empty circles represent filled, partially filled, and empty electron states. (b) Electron density profile for the case of a soft confinement potential. Plateaus correspond to the strips of incompressible liquids. (d) Electron density profile for a steep confinement potential (panels (a) and (b) adopted from [34]).

The width of the compressible and incompressible strips decreases as the confinement potential becomes steeper, so for a steep enough potential this assumption is violated and the proposed theory is not applicable anymore. Comparably soft confinement

potentials are realized in gate-confined or etched 2DEGs. The evolution of incompressible strips as a function of a magnetic field was studied experimentally [35] using a single-electron transistor (SET) fabricated on the surface of the GaAs/AlGaAs heterostructure. To achieve high electron mobility, the 2DEG was placed 90 nm below the surface of the sample, which directly limits the spatial resolution of this technique. As a consequence, only up to the two widest and innermost incompressible strips were clearly resolved. This experimental technique was also used to track the evolution of the chemical potential in the bulk of a 2DEG as a function of magnetic field [36], and shows a zigzag-like behavior, qualitatively agreeing with the theoretical calculations [37].

A big step forward in understanding the microscopic details of the quantum Hall effect was made with the help of several scanning-probe techniques. In one of these studies, the nanometre-scale electronic structures that exist in the quantum Hall regime were observed using sub-surface charge accumulation measurements [38]. In the work of McCormick et al. [39], an atomic force microscope was used as a local voltmeter to measure the Hall voltage profile along the entire width of the sample. This study confirms the presence of edge states with a width that agrees with the theoretical model of Chklovskii et al. [34]. Another beautiful study by Yacoby et al. [40] showed that a scanning SET can be used to simultaneously measure surface potential, compressibility, and Hall voltage with sub-micron resolution. The incompressible strips are clearly visible in the compressibility images that are correlated with the Hall voltage and surface potential images.

The case of non-interacting electrons confined with infinitely steep confinement potential (Fig.8c,d) was theoretically studied by MacDonald and Streda [41]. In this theory, different Landau levels bend upwards as the guiding center position approaches the edge of the sample and crosses the Fermi level at different locations, forming the edge states. The wave functions of these edge states are orthogonal to each other as they have distinct guiding center positions and, correspondingly, different momenta along the edge. At the same time, the spatial components of these wave functions in the di-

rection perpendicular to the sample edge have substantial overlap. The total electron density for this case is shown in Fig.8d. A small density increase prior to complete depopulation is caused by electrons from the lowest Landau levels with their guiding center position located beyond the sample edge, which is depicted by vertical dashed line [42].

The connection between these two distinct types of confinement potential was made by Chamon and Wen [43]. They were able to show how the edge states undergo reconstruction as the confinement potential decreases. The mechanism of edge state reconstruction is particularly interesting, as control over it is an important milestone on the road towards the quantum Hall-based quantum computing [44–46]. It turns out to be very difficult to form high mobility 2DEGs with a steep confinement potential, as such 2DEGs are usually located far away from gates and dopant layers, which define the steepness of the potential profile. The cleaved-edge overgrowth technique stands out, as it is the only known method to fabricate high-quality 2DEGs with steep confinement potentials in semiconducting heterostructures [47] . Unfortunately, this technique is quite sophisticated and allows fabrication of samples with only one edge out of four having a steep confinement potential.

The discovery of 2D-crystals opens a new era in the study of the quantum Hall effect, as electrons in these materials reside right at the surface and can be directly probed using various optical, electrical, and scanning probe techniques. One of such studies [48] shows how scanning tunneling microscopy (STM) and spectroscopy (STS) can be used to probe the local density of states in a single-layer graphene [49] flake, placed in a magnetic field. In this work, the graphene flake was directly placed on graphite, which results in a steep confinement potential with no edge state reconstruction. Unfortunately, bare 2D materials are very susceptible to surface defects and impurities, so special techniques (suspension [50], encapsulation [51]) have been developed to fabricate samples with high carrier mobility.

More recently, the focus has shifted towards the study of edge states in topological

materials. To name just a few, we will mention the study done by Drozdov et al. [52] of topological edge states in bismuth bilayers. Using STM (Fig.9a) and STS (Fig.9b) they were able to confirm the presence of theoretically predicted [53], one-dimensional topological edge states in the Bi-bilayer islands, which show up in this experiment as an increase in the density of states at alternating edges of hexagonal depression.

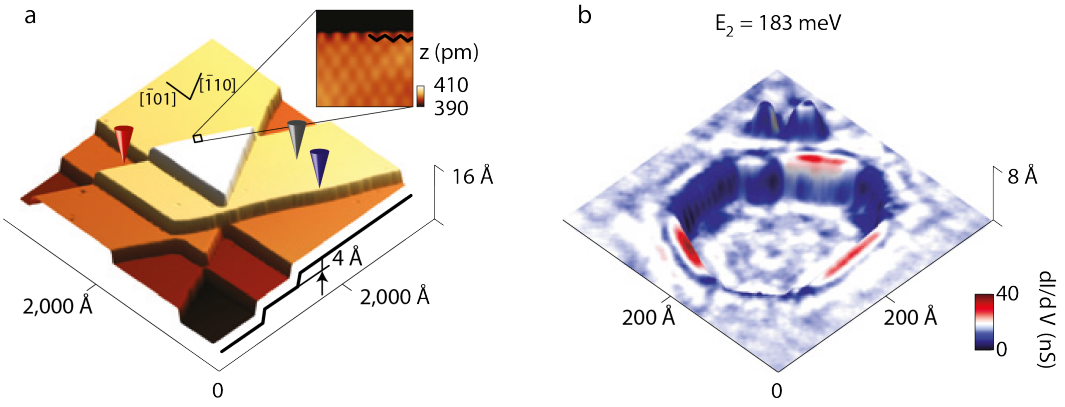

Figure 9: (a) STM topographic image of the Bi(111) surface. (b) Topography image of a hexagonal depression false-colored with differential conductance (adopted from [52]).

Using a similar technique, Peng et al. [54] was able to show the presence of topological states at the step edge of monolayer WTe_2, which, together with the superconducting property of the bulk, makes this system a promising platform for realizing topological superconductivity [55].

In this thesis, a quantum wire was used to study Landau level edge states formed in a 2DEG with steep confinement potential. The exceptional quality of the quantum wire and the 2DEG allows us to track edge states with very high precision through a wide range of magnetic fields. This technique is not restricted specifically to Landau level edge states and can be employed to study any other edge states.

2 Evolution of the quantum Hall bulk spectrum into chiral edge states

T. Patlatiuk*, C. P. Scheller*, D. M. Zumbühl

University of Basel, Klingelbergstrasse 82, CH-4056 Basel, Switzerland

D. Hill, Y. Tserkovnyak

Department of Physics and Astronomy, University of California, Los Angeles, California 90095, USA

G. Barak, A. Yacoby

Department of Physics, Harvard University, Cambridge, Massachusetts 02138, USA

L. N. Pfeiffer, K. W. West

Department of Electrical Engineering, Princeton University, Princeton, New Jersey 08544, USA

* These authors contributed equally to this work.

This chapter was published in Nature Communications **9**, 3692 (2018).

2.1 Abstract

One of the most intriguing and fundamental properties of topological systems is the correspondence between the conducting edge states and the gapped bulk spectrum. Here, we use a GaAs cleaved edge quantum wire to perform momentum-resolved spectroscopy of the quantum Hall edge states in a tunnel-coupled 2D electron gas. This reveals the momentum and position of the edge states with unprecedented precision and shows the evolution from very low magnetic fields all the way to high fields where depopulation occurs. We present consistent analytical and numerical models, inferring the edge states from the well known bulk spectrum, finding excellent agreement with the experiment – thus providing direct evidence for the bulk to edge correspondence. In addition, we observe various features beyond the single-particle picture, such as Fermi level pinning, exchange-enhanced spin splitting and signatures of edge-state reconstruction.

2.2 Introduction

Systems with topologically protected surface states, such as the quantum spin Hall insulator [56, 57] and many other topological insulators, are currently attracting great interest. Among the topological states, the integer quantum Hall effect [29] stands out since it was first discovered. It is the most simple case out of which others have emerged, and thus serves as a paradigmatic system. Accessing the surface states in a topological system separately and independently, however, has proven to be challenging for a number of reasons, including disorder, insufficient resolution or remnant bulk conductivity contaminating transport experiments. Local probes, such as scanning single electron transistors, could in principle overcome the bulk conductivity problem and have been intensely investigated in the context of quantum Hall systems [35, 40, 54, 58–64]. However, moderate spatial resolution and the requirement of large magnetic fields for discriminating among individual edge states have limited existing experiments

to low filling factors and prevented tracking the evolution of quantum hall edges all the way down to low fields.

Previously, tunneling spectroscopy of cleaved edge overgrowth wires has established the system as one of the best realizations of a 1D ballistic conductor, exhibiting distinct signatures such as quantized conductance [65], spin-charge separation [66], charge fractionalization [13] and indication of helical nuclear order induced by the strongly interacting electrons [8, 67]. Here, we use a vector magnet to independently control two orthogonal magnetic fields: one to form quantum Hall edge states and another to perform tunneling spectroscopy.

In this work, we use momentum resolved tunneling spectroscopy to track the guiding center (GC) positions of the quantum Hall edge states with nanometer precision. Over the magnetic field evolution, we observe first magnetic compression towards the sample edge, and then, at higher fields, motion into the bulk and magnetic depopulation of Landau levels (LLs). Note that in this work we are studying integer quantum Hall edge states and not the spin Hall effect or any other topological state. However, this technique is also applicable to the latter states. Using both an analytical model and numerical solutions for the evolution of edge states in the limit of hard wall confinement [41, 68, 69], we are able to match very well the tunneling spectroscopy fingerprint of the conducting edge states from the topologically gapped bulk phase and hence reveal their direct correspondence. Individual edge modes [70–72] are discernible down to unprecedented low magnetic fields $B_z \approx 10\,\mathrm{mT}$, where the bulk filling factor ν is about 500. Furthermore, we observe the chiral nature of edge states, as well as Fermi level pinning effects. In addition, interactions lead to signatures of edge reconstruction and exchange-enhanced spin-splitting at large in-plane magnetic fields. We emphasize that this spectroscopy is done at zero bias, thus eliminating heating or lifetime effects.

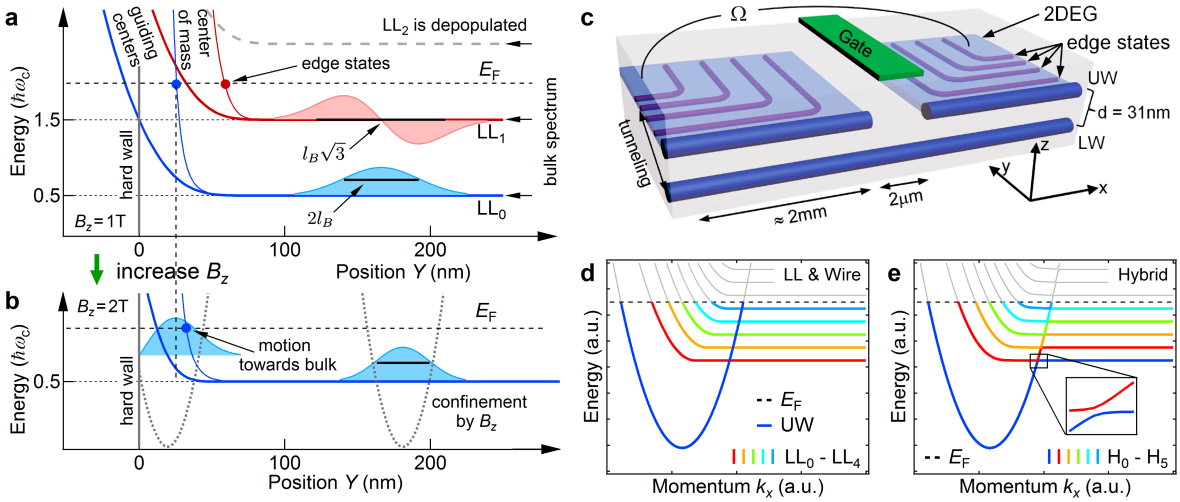

Figure 10: Bulk to edge correspondence. a, Energy evolution of the center of mass (CM) position (thin blue/red curves) and the guiding center (GC) position (bold blue/red curves) for the first two Landau levels LL_0 and LL_1. Here, LL_2 is above the Fermi energy and is depopulated. The confinement (hard wall) lifts the bulk LLs in energy, resulting in corresponding edge states (solid circles) when the CM is crossing the Fermi energy E_F. Note that the Fermi energy shown here is lower than in the experiment. **b,** Same as **a** for larger magnetic field B_z, where the width $2\sigma_n = 2l_B\sqrt{2n+1}$ of LL_n is squeezed and LL_1 was depopulated, with magnetic length l_B. **c,** Coordinate system (black) and sample schematic, showing the 2DEG in light blue, upper and lower quantum wire (UW/LW) in dark blue, top gate in green, and CM for integer quantum Hall edge states in purple. Ω indicates the conductance measurement. **d,** Simplified UW and LL dispersions calculated for independent triangular and hard wall confinement. **e,** Calculated dispersion for the combined confinement potential, resulting in hybridized states H_n with avoided crossings (see inset). Here, the bulk LL_0 transforms into the UW mode at the sample edge. Gray segments indicate empty states, colored ones are filled.

2.3 Results

2.3.1 Integer quantum Hall edge states for the hard wall confinement

A magnetic field B_z, applied perpendicular to a 2D electron gas (2DEG), quenches the kinetic energy of free electrons and condenses them into discrete LLs that are energetically separated by the cyclotron energy $\hbar\omega_c$. Here, $\omega_c = eB_z/m^*$ denotes the cyclotron frequency, e the elementary charge, $\hbar$ the reduced Planck constant, and m^* the effective electron mass. Upon approaching the sample edge the electrostatic confinement potential lifts LLs in energy and causes them to intersect with the Fermi energy, thereby forming a corresponding edge state for each bulk LL, see Fig. 10a and Supplementary Fig. 4. Here, we use the Landau gauge (vector potential $\boldsymbol{A} = 0$ at the edge), where the momentum k_x along the quantum wires is a good quantum number that fully characterizes each state. Given k_x, all other quantities may be calculated, such as the wave function center of mass (CM) as well as the GC position $Y = k_x l_B^2$, where $l_B = \sqrt{\hbar/(eB_z)}$ denotes the magnetic length. Throughout the paper, the filling factor is defined as $\nu = 2n + g$, where $n = 0, 1, 2, ...$ is the orbital Landau level index, and $0 \leq g < 2$ is the spin occupancy.

At elevated B_z, shown in Fig. 10b, the cyclotron splitting is enhanced. As a consequence the highest LLs are energetically lifted above the Fermi energy and thus magnetically depopulated of electrons, compare Fig. 10a and b. In addition, increasing B_z reduces the magnetic length, thereby squeezing the remaining LL wave functions by magnetic compression and moving the corresponding edge states closer to the sample edge. This holds up to a certain point, when the edge state starts suddenly moving back into the bulk just before being magnetically depopulated, see Fig. 10b.

A sample schematic is depicted in Fig. 10c and consists of two parallel GaAs quantum wells, separated by a thin AlGaAs tunnel barrier. The upper quantum well hosts a high mobility 2DEG, while the bulk of the lower quantum well remains unpopulated. Cleavage of the sample and subsequent overgrowth results in strongly confined 1D-

channels in both quantum wells (see methods section and refs. [2, 13, 65, 66, 73–78] for more details), termed upper wire (UW) and lower wire (LW) in the following. The LW is used as a tunnel probe to spectroscopically image the integer quantum Hall edge states of the upper quantum well at effectively zero bias voltage.

A simplified picture for the complete dispersion for the upper system is shown in Fig. 10d. It consists of a single localized wire mode UW (dark blue), resulting from the triangular confinement at the sample edge, and the LL spectrum in presence of hard wall confinement and perpendicular magnetic field B_z. Solving the combined electrostatic problem (hard wall confinement with triangular potential near the edge) hybridizes the LL spectrum and quantum wire modes at commensurate conditions where energy and momentum are matched, see Fig. 10e. As a consequence the bulk LL_0 transforms into the lowest quantum wire mode at the sample edge. While each LL like edge state in Fig. 10e acquires an additional node in the wave function in comparison to the hard wall spectrum of Fig. 10d, the intersection with the Fermi energy E_F is hardly changed [79, 80], giving almost the same effective momentum k_x. Therefore, the simplified dispersion of Fig. 10d is used in the following to describe the magnetic field evolution of edge states.

The tunneling regime is obtained by setting the top gate in Fig. 10c to deplete the 2DEG and all UW modes beneath it while preserving a single conducting mode in the LW. This divides the upper system electrically into two halves but preserves tunnel coupling on each side to the LW. Due to translational invariance of UW and LW (away from the top gate, where tunneling occurs), momentum is conserved during the tunneling event, and can be controlled by means of the Lorentz force. In particular, in presence of an in-plane magnetic field B_y applied perpendicular to the plane spanned by the two wires (see coordinate system in Fig. 10c), tunneling electrons experience a momentum kick $\Delta k_x = -edB_y/\hbar$ along the x-direction of free propagation, thus effectively shifting the wire dispersions with respect to each other [13, 66, 75, 76]. Here, d denotes the tunneling distance along the z-direction. The resulting zero-bias tunneling conductance is large

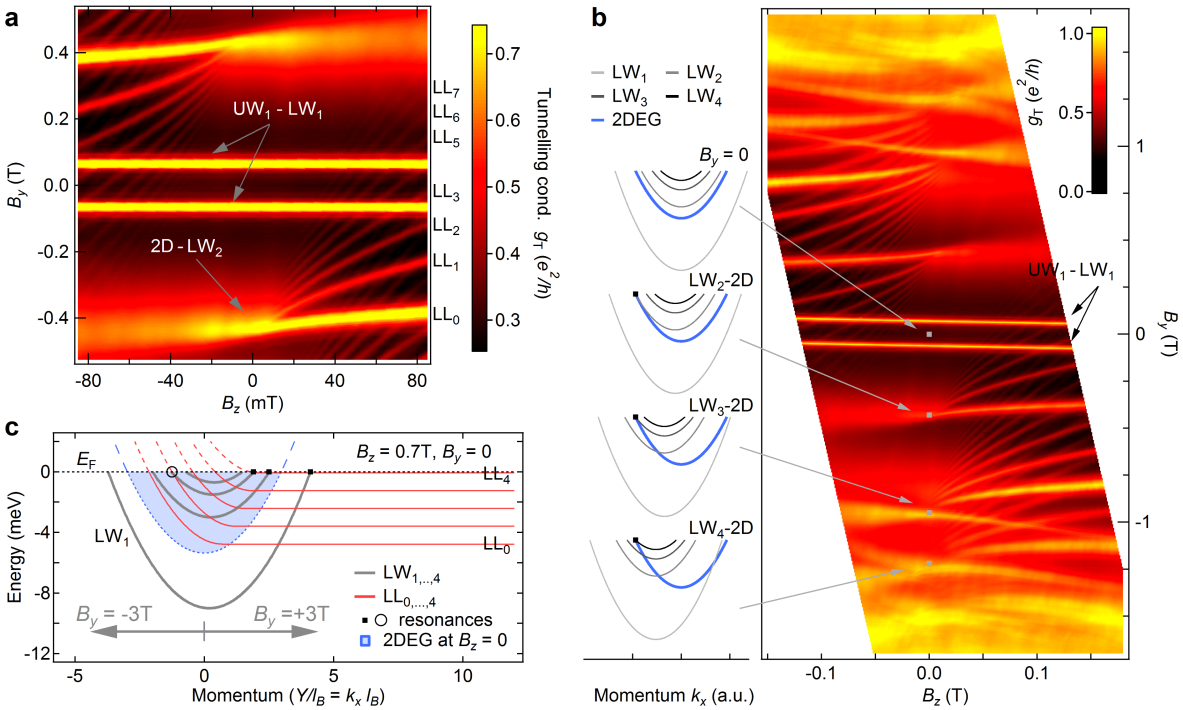

Figure 11: **Formation and B-field evolution of the chiral integer quantum Hall edge states. a,** Differential tunneling conductance as a function of in-plane magnetic field B_y and perpendicular magnetic field B_z at $\approx 10\,\mathrm{mK}$. The 2D-wire transitions break up into multiple curves and fan out with increasing B_z, see also Supplementary Fig. 2. Horizontal resonances at small $|B_y|$, associated with wire-wire tunneling, are not affected by B_z. **b**, Larger B_y range than **a**, showing 6 fans corresponding to tunneling to modes LW_2, LW_3, and LW_4. Due to the chiral nature of the states, the fans are not seen in the data when only B_z is reversed. The sketches depict the resonance condition (black dots) at $B_z = 0$. **c**, Schematic representation of quantum wire (gray) to LL (red) tunneling at $B_z = 0.7\,\mathrm{T}$. B_y shifts the lower wire dispersion in relation to the LLs, as indicated by gray arrows of corresponding length. The blue filled parabola indicates the 2DEG dispersion for $B_z = 0$, projected onto the k_x axis. Black dots and black circle indicate resonant tunneling to bulk states and edge state, respectively.

whenever Fermi-points of upper and lower system coincide, see also Supplementary Fig.1a. In a similar fashion, each LW mode can also be brought into resonance with any given LL. However, in contrast to the quantum wires, the effective momentum of edge modes $k_{x,\mathrm{LL_n}}$ of the LLs depends on B_z.

2.3.2 Formation and evolution of the edge states

Fig. 11 shows the measured differential tunneling conductance as a function of magnetic fields B_z and B_y. Two horizontal features are visible that correspond to resonant tunneling (energy and momentum conservation) between co-propagating electrons of the first upper and lower wire mode, UW_1 and LW_1, respectively. Since the electron

density in UW_1 and LW_1 is very similar, only little momentum transfer and correspondingly small $|B_y|$ is required to bring the modes into resonance. These resonances are independent of B_z because the Y coordinates of both UW_1 and LW_1 modes are very similar. In addition to wire-wire tunneling, extensively studied in the past [13, 66, 75–78], sharp tunneling resonances of a different origin [70–72] are observed that split into fans of discrete curves in presence of a perpendicular field and separate with increasing field strength. For each fan, about 10 curves can be resolved down to $B_z \gtrsim 10\,\mathrm{mT}$, see Fig. 11. As we will show, these fans correspond to resonant tunneling between quantum Hall edge states and the LW modes which are acting as a momentum selective spectrometer. The fan structures observed here track the momentum evolution of edge states with B_z and thereby produce a fingerprint of the conducting edge states. This is in contrast to the conventional Landau fan that simply is an expression of the bulk filling factor as a function of 2DEG density and B_z.

The wire modes are supporting states propagating in both negative and positive x-direction, irrespective of the perpendicular field, and give transitions extending over both positive and negative B_z, see also Supplementary Fig. 10. The quantum Hall edge states, on the other hand, are chiral and are thus propagating only in one direction for a chosen sign of B_z along a given edge. The corresponding LL dispersions are therefore not symmetric under reversal of k_x, and the fan structures become directional. Indeed, the fans are seen only for one sign of B_z around a given B_y, e.g. in the lower right in Fig. 11a but not the lower left. The opposite sign of B_z also supports a fan but only when B_y is inverted at the same time, i.e. when the total B-field is switching sign (Onsager's reciprocity [81]), see upper left in Fig. 11a. This directly indicates the chiral nature of these edge states.

Besides fan structures in Fig. 11a, there are additional fans originating at different B_y values, see Fig. 11b where a larger field range is displayed. These other fans result from tunneling to other modes of the LW. Since each of the different modes in the LW has a different density and thus a different Fermi momentum, an overall momentum shift

results which displaces the fans along B_y, as illustrated in the sketches of Fig. 11b, where the resonance condition at $B_z = 0$ is shown (origin of the fans).

In order to quantitatively understand the field evolution of the fan structures, the LL dispersions have to be considered, which depend on the electrostatics at the edge [34, 58, 82–87]. For the present samples, the cleavage exposes an atomically sharp edge, that is immediately overgrown by means of lattice matched molecular beam epitaxy [73, 74]. The resulting hard wall confinement potential gives rise to the LL dispersions of Fig. 11c (red) [68, 69], shown along with the quantum wire modes in the lower well (gray) and the 2DEG at $B_z = 0$ (blue). Lowering B_z reduces the bulk LL energy splitting $\hbar\omega_c$ and hence introduces a more dense LL structure while leaving the LW modes unaffected (due to their strong transverse confinement). The in-plane magnetic field B_y, on the other hand, is assumed to not directly affect the LLs, but only shift their dispersion in relation to the LW.

The fan structures at positive B_Z in Fig. 11b can then be understood in terms of momentum conserving edge state tunneling using one of the LW left Fermi points as a spectrometer, see Fig. 11c, where the case of LW3 is marked with an open circle. Thus, each fan represents a map of the momenta of the LL edge states at the Fermi energy, and thus, via the GC-momentum relation $Y = k_x l_B^2$, a precise map of the GC positions of the edge states. Upon approaching $B_z = 0$, the effective momentum of edge states, i.e. the intersection of LLs with the chemical potential, approaches the $B_z = 0$ Fermi wave vector $-k_{\mathrm{F,2D}}$ of the 2DEG. During this process edge states associated with LLs of increasing orbital index subsequently come into co-propagating resonance with LW_2 at $B_y = 0$.

In the following section, the range in perpendicular magnetic field is extended (Fig. 12) in order to study the field evolution of edge states and their magnetic depopulation at large B_z. For better visibility, we plot the second derivative with respect to B_y of the differential tunnel conductance in Fig. 12a. A large number of interpenetrating resonances are visible, extracted in Fig. 12b for clarity, and grouped into bundles according

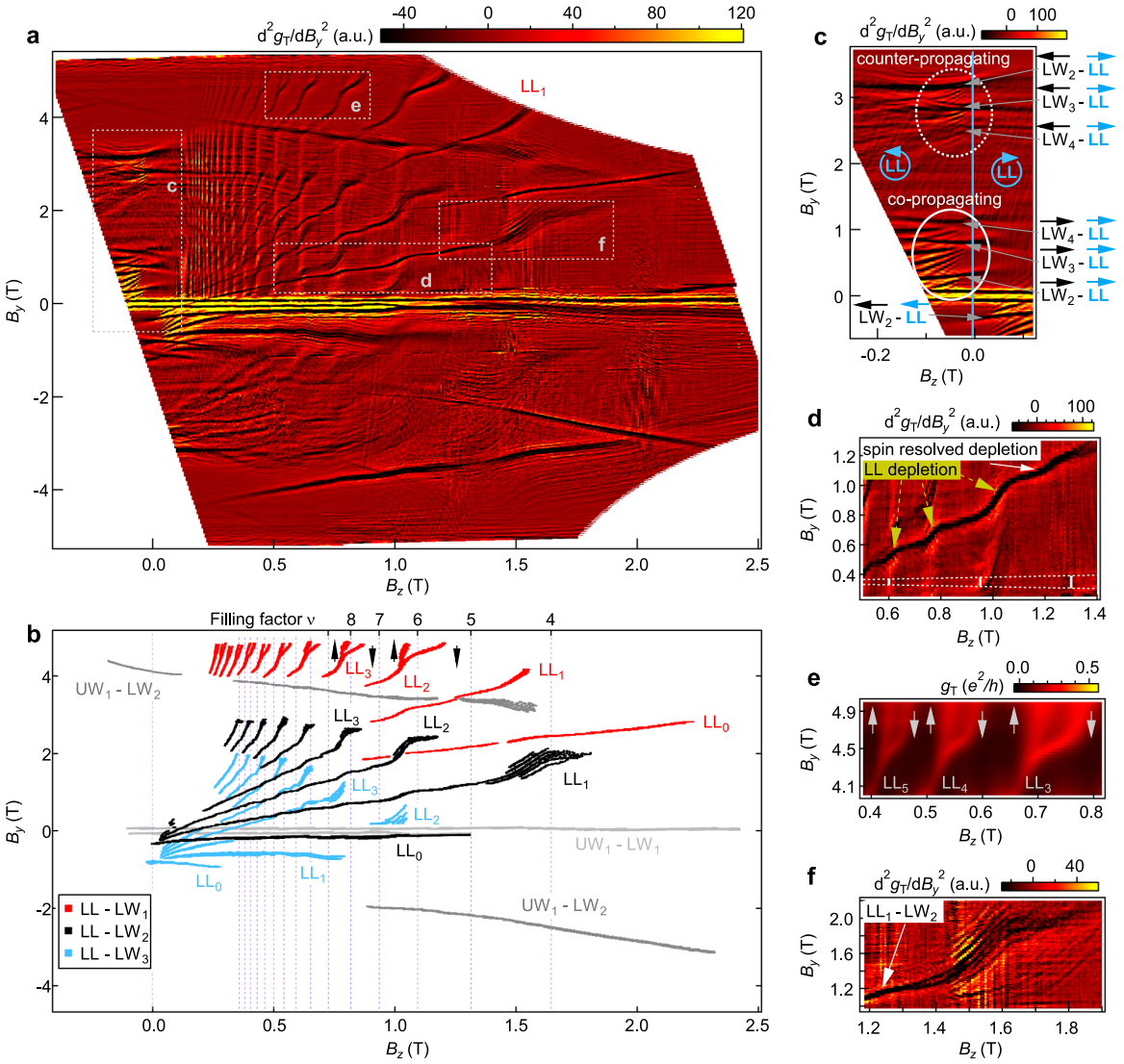

Figure 12: **Magnetic depopulation and spin splitting of integer quantum Hall edge states. a,** Second derivative with respect to B_y of the differential tunnel conductance (d^2g_T/dB_y^2) as a function of magnetic fields B_y and B_z. **b**, Extracted resonance positions from **a**. Red, black, and light blue data correspond to tunneling between edge modes and the first (LW_1), second (LW_2) and third (LW_3) lower wire mode. **c,d,e,f,** Zoom in of **a** for regions of interest: **c,** Landau fans for $B_z < 0$ (counter-clockwise edge states $\Leftrightarrow$ right moving edge state at cleaved edge), imaged with co-propagating (white solid ellipse) and counter-propagating wire modes (white dashed ellipse).**d,** Jumps in the resonance position whenever the bulk filling changes. The three vertical bars of growing height indicate a distance of 2 nm in real space. The height ΔB_y of the bar is given by $\Delta B_y = \Delta Y B_z/d$, where ΔY is the distance in real space. Thus, the real space resolution is improving with increasing magnetic field B_z. **e,** LL spin splitting clearly visible even in undifferentiated raw data (tunneling conductance g_T). **f,** branching out of resonances at the transition to magnetic depopulation.

to their different origin, i.e. red, black, and light blue data indicate co-propagating tunneling to the first three LW modes, LW_1, LW_2, and LW_3, respectively. The LL edge states can also be mapped in a counter-propagating fashion (Fig. 12c), e.g. where the wire state and edge states are propagating in opposite directions. To achieve momentum conservation in this case, a relatively large momentum kick needs to be provided by the magnetic field, and these transitions thus appear at larger B_y.

In addition to edge state−wire tunneling, intra−wire transitions are seen and color coded in gray in Fig. 12b. As the wave functions for LW_1 and UW_1 are very similar, their CM positions nearly sit on top of each other and hence there is no resulting momentum kick $\Delta k_x = e\Delta y B_z/\hbar$ due to the perpendicular field. Here, Δy denotes their lateral displacement. As a consequence, the corresponding resonances (light gray) appear as horizontal lines. In contrast to this, transitions involving different wire modes, e.g. UW_2 and LW_1 (dark gray data in Fig. 12b), appear with a slope that reflects the different center of mass positions of the participating wave functions.

Returning to LL tunneling, we note a few important points. First, all LL resonances terminate on the right end at a specific bulk filling factor when magnetic depopulation removes the corresponding edge state from the sample, clearly seen for the black data in Fig. 12b. In particular, tunneling involving LL_2 with $n = 2$ is observed up to $B_z \approx 1.1\,\mathrm{T}$, terminating at the corresponding bulk filling factor $\nu = 6$, labeled on the top axes in Fig. 12b. Here, spin occupancy $g = 2$ because of a spin-unresolved case. The resonances for LL_3 with $n = 3$ are already lost above $B_z \approx 0.8$ at $\nu = 8$, independent of which LW mode is used as a spectrometer (compare red, black and light blue data in Fig. 12b).

2.3.3 Spin splitting and Landau level depopulation

A set of bright vertical features appears in the upper half of Fig. 12a (corresponding to the dashed vertical lines of integer filing factors in Fig. 12b), whose position is coincident with the disappearance of LL resonances. These features are even more

visible in Supplementary Fig. 5. These result from probing the flat part of the LL dispersion i.e. they reflect the bulk filling factor, and account for the majority of the measured tunneling signal in Fig. 12 prior to differentiation of the data. For example at $B_z = 0.7\,\mathrm{T}$, shown in the level schematics of Fig. 11c, LL_4 is aligned with the chemical potential causing a resonance with the right Fermi-points of LW_1, LW_2, and LW_3 as indicated with black dots. While applying a positive in-plane magnetic field shifts the LW dispersions to the right and hence preserves resonant tunneling, this condition is lost for sufficiently negative B_y. Consequently, the vertical lines, corresponding to magnetic depopulation of a LL in the bulk, appear predominantly at positive B_y.

Beyond the vertical lines, the smooth evolution of LL tunneling resonances from Fig. 11 develops shoulder-like structures at larger B_z, clearly seen in Fig. 12d. The shoulders appear exactly at the transition between bulk filling factors (vertical lines in Fig. 12b) and are attributed to Fermi level pinning to LLs and impurity states, respectively, previously only accessible through investigation of the bulk 2DEG properties [88, 89]. Here, we also note that the momentum resolution and the corresponding real space resolution of this spectroscopy technique improves with perpendicular magnetic field (white bars in Fig. 12d) and reaches the nanometer range for fields above 1 T. The resonance width depends on the degree to which momentum conservation is broken during tunneling, i.e. breaking of translational symmetry due to disorder and the finite size of the tunneling region. Finally, also, any variation of the tunneling distance between the upper and lower system, such as single-atomic steps in the growth plane or other crystal defects, will add to the observed broadening.

While each LL carries two spin resolved sub-bands, energetically split by the total Zeeman energy given by magnetic fields B_z and B_y, the corresponding difference in Fermi wave vectors is too small to be resolved by means of this spectroscopic method. However, at large in-plane magnetic fields, the interplay between Hartree term and exchange interactions [90] may lead to the formation of spin polarized strips where spin split sub-bands are also separated in real space [91]. As a consequence, tunneling

resonances split up for the red data in Fig. 12e and the spectroscopy becomes spin selective.

2.3.4 Analytical model of resonant tunneling

In the last part of this article, we develop an analytical model [41, 68, 72, 79], and in addition provide numerical predictions (see supplement) for the evolution of LLs in the limit of hard wall confinement using a 1D single-particle Schrödinger solver. The perpendicular magnetic field introduces an additional local parabolic confinement, centered at each GC position Y, hence condensing bulk electrons into discrete LLs with well known Hermite-Gaussian wave functions. We assume that upon approaching the hard wall, LLs remain at their bulk energy $E_n^{\mathrm{bulk}} = \hbar\omega_{\mathrm{c}}\left(n+\frac{1}{2}\right)$ until the tail of the wave function intersects with the hard wall ($Y \approx \sigma_n$ for $\mathrm{LL_n}$, with σ_n the half width of the LL wave function). When moving Y even closer to the edge or beyond, the hard wall retains the wave functions within the sample, thus separating in space the GC position $Y = k_x l_B^2$ and the wave function center of mass (CM) position, see Fig. 10a,b and Fig. 13a. As as consequence, LLs acquire kinetic energy and are simply lifted up the parabolic magnetic confinement until they cross the Fermi energy, thereby forming the conducting edge states (Figs. 10a,b and Supplementary Figs. 3 and 4). Using these approximations, the LL dispersion $E_n[k_x]$ reads:

$$E_n[k_x] = E_n^{\mathrm{bulk}} + \frac{\hbar^2}{2m^*}\Theta[\sigma_n - Y]\left(\frac{\sigma_n}{l_B^2} - k_x\right)^2, \tag{3}$$

where $\Theta[x]$ is the Heaviside function. The condition for resonant tunneling is obtained by equating the LL spectrum at the Fermi energy with the lower wire dispersion $\epsilon_{k_x}^{(l)}$, shifted in k_x-direction to account for the momentum kick $eB_y d$ (tunneling to the lower system in presence of B_y) and $eB_z\Delta y_i$ (displacement Δy_i of the $\mathrm{LW_i}$ wave function CM with respect to the cleaved edge):

$$\epsilon_{k_x}^{(l)} = \frac{\left(\hbar k_x - eB_y d - eB_z\Delta y_i\right)^2}{2m^*} + \epsilon_0^{(l)}. \tag{4}$$

Here, $\epsilon_0^{(l)}$ is an energy offset that accounts for the difference in band edges of 2DEG and respective lower wire mode with respect to the common Fermi energy. Combining Eqns (3), (4) we obtain the evolution of the tunneling resonances as a function of B_y and B_z,

$$\frac{eB_y d}{\hbar} = \sqrt{\frac{2n+1}{l_B^2}} - \sqrt{k_{\mathrm{F,2D}}^2 - \frac{2n+1}{l_B^2}} + \gamma_i - \frac{\Delta y_i}{l_B^2} \tag{5}$$

where $\gamma_i = \sqrt{k_{\mathrm{F,2D}}^2 - 2m^*\epsilon_0^{(l)}/\hbar^2}$ is a quantum wire mode dependent overall momentum shift.

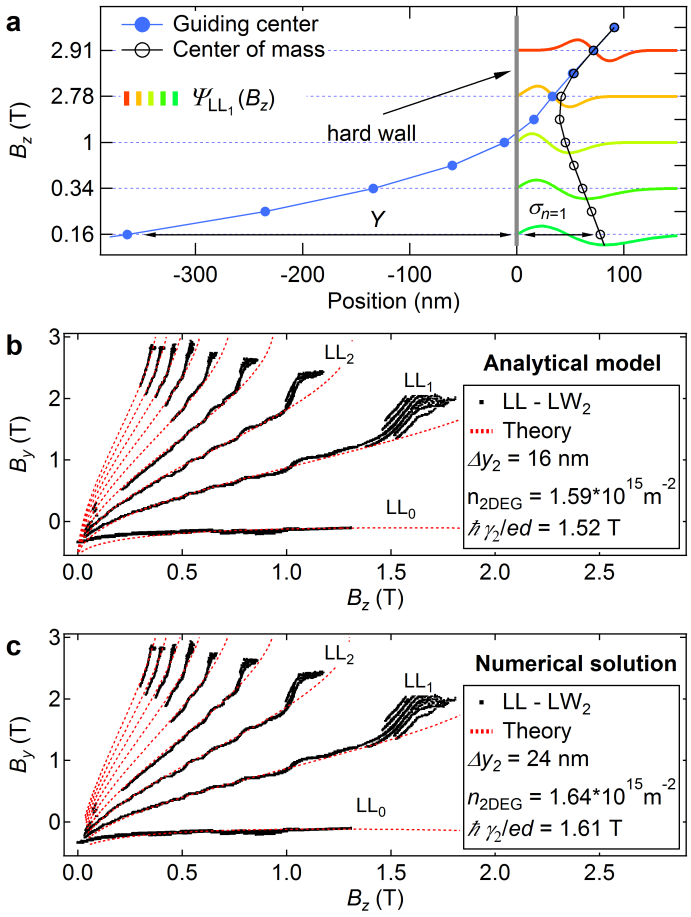

Figure 13: **Comparison of experiment and theory. a,** Landau Level wave functions for particular values of B_z chosen to visualize the important stages of magnetic field evolution. Note that the resulting vertical scale is highly nonlinear. The wave functions are obtained from a numerical Schrödinger solver, showing magnetic compression of the wave function and subsequent depopulation. The hard wall confinement completely separates wave function CM and GC position, the latter residing outside the physical sample for most of the B-field range. Hybridization of LLs and UW_1 would result in an additional node for LL wave functions at the Fermi energy. In **b,c** experimental data are compared to theoretical predictions from an analytical model and to numerical solutions from a single-particle Schrödinger solver, respectively.

2.4 Discussion

Both the numerical and the analytical models capture the experimental tunneling resonances very well and result in very similar fitting parameters, shown in Fig. 13b,c for LL tunneling to LW_2 (black data from Fig.12). We note that equally good fits are obtained for tunneling to other lower wire modes as well, using the same 2DEG density $n_{2DEG} = k_{F,2D}^2/2\pi$ and increasing quantum wire displacement Δy_i for higher modes (see Supplementary Fig. 5), as expected – thus lending further support to the models. We emphasize that both models consistently deliver the CM positions, with similar nanometer precision as the GC positions extracted directly from the spectroscopy. This makes it possible to plot a full map of the magnetic field evolution of the edge states, see Fig.13a. Throughout the process of increasing magnetic field Bz, the electron wave function is progressively compressed (from green to red curves). There are two stages of the edge state motion as magnetic field Bz increases: first, motion of the center of mass towards the hard wall (empty circles for $B_z < 2.78\,\mathrm{T}$) and motion away from the hard wall at larger fields, see also Supplementary Fig.3. During the latter stage, the center of mass merges with the guiding center position (black and blue curves approach and then coincide for larger B_z in Fig.13a), followed by depopulation of the corresponding LL.

Despite the good match between experiment and non-interacting single-particle theory, there remain minor discrepancies. In particular the shoulder structures at the transitions between integer bulk filling factors (Fig. 12d), and the spin splitting observed at large in-plane magnetic field (Fig. 12e) are not captured by the model. Furthermore, at the transition to magnetic depopulation, individual resonances are observed to branch out, clearly visible for e.g. the LL_1-LW_2 transition in Fig. 12f. Splitting of single resonances could arise e.g. from edge reconstruction or may also result from the formation of stripe or bubble phases.

In summary, we employed momentum-resolved tunneling spectroscopy to image the

evolution for the lowest $\approx$ 10 integer quantum Hall edge states of a GaAs 2DEG with nanometer resolution, and down to magnetic fields of $B_z \gtrsim 10\,\mathrm{mT}$ ($\nu_{\mathrm{bulk}} \approx 500$). We directly observe the chiral nature of integer quantum Hall edge states, as well as magnetic depopulation at the respective bulk filling factor. In addition, spin splitting is observed at the transition to depopulation. Theoretical predictions assuming the topologically gapped bulk spectrum and hard wall confinement reproduce very well the experimental data over the entire range of magnetic field, thus confirming the bulk to edge correspondence.

In the future, also fractional quantum Hall edge state can be investigated with the spectroscopy technique presented here. The present sample exhibits clearly visible $\nu = 4/3$ and $\nu = 5/3$ fractional states in conventional transport measurements. Imaging the fractional states by means of this highly sensitive momentum-resolved tunnel spectroscopy would be of great interest and can be addressed in future experiments. Fractional states are stabilized by electron-electron interactions and are thus believed to exist only in the vicinity of the respective filling factor, in contrast to integer edge states that persist at all fields up to their magnetic depopulation. Because of power law exponents determining the tunneling conductance from the fractional quantum Hall edge states [47, 92–95], a pronounced DC bias voltage dependence is expected for these states. This also makes it very interesting to explore another experimental knob, bias voltage, which controls the energy transfer during the tunneling event.

Beyond fractional states, the technique described here can also be applied to other topological insulator materials. In those systems where a wire exhibiting tunneling can be integrated or placed in parallel, edge states, both 1D or 2D in nature, can also be studied with this method with unprecedented resolution in a weakly invasive way. We note that ultra clean wires, such as used here to probe the edge states, are not necessary, in fact, thus opening the door to studying a variety of topological materials and their exotic edge states with this new tunneling spectroscopy.

2.5 Acknowledgements

We thank Carlos Egues, Bertrand Halperin, Daniel Loss, and Jelena Klinovaya for very helpful discussions and we thank M. Steinacher and S. Martin and their teams for technical assistance. This work was supported by the Swiss Nanoscience Institute (SNI), NCCR QSIT, Swiss NSF, and the European Microkelvin Platform (EMP). A. Y. was supported by the NSF Grant No. DMR-1708688. The work at Princeton University was funded by the Gordon and Betty Moore Foundation through the EPiQS initiative Grant GBMF4420, and by the National Science Foundation MRSEC Grant DMR 1420541.

2.6 Author Contributions

T.P., C.P.S, D.M.Z conceived the experiment, analyzed the data and wrote the manuscript. T.P. and C.P.S. performed the experiments and numerical calculations. D.H. and Y.T. developed and carried out the theoretical work. G.B., A.Y., L.N.P., K.W.W. designed and fabricated the sample. All authors discussed the results and commented on the manuscript.

2.7 Competing interests

The authors declare no competing interests.

2.8 Methods

2.8.1 Device layout

The device used for this study is produced by means of the cleaved edge overgrowth method. It consists of a lower, 30 nm wide GaAs quantum well, separated by a 6 nm

thick AlGaAs tunnel barrier from the upper, 20 nm thick GaAs quantum well [75]. A silicon doping layer above the upper quantum well provides free charge carriers, resulting in the formation of a 2DEG in the upper quantum well while the lower well remains unpopulated. The sample with prefabricated tungsten top gate is then cleaved inside the growth chamber and immediately overgrown on the sample edge (including a Si doping layer). Due to the additional side dopants, charge carriers are attracted to the sample edge, thereby forming strongly confined 1D channels (in upper and lower quantum well) along the entire cleaved edge. The 1D channels support a few (5 or less) transverse modes with sub-band spacing up to 20 meV and mean free path exceeding 10 μm [65]. Ohmic indium solder contacts to the 2DEG allow for transport studies. While the upper 1D system is well coupled to the 2DEG, the lower 1D channels are only weakly tunnel coupled, thus allowing for tunnel spectroscopy measurements.

2.8.2 Measurements setup

Tunneling spectroscopy measurements are recorded with standard low frequency (5-10 Hz) lock-in technique with typically 6 μV AC excitation. All measurements are done at effectively zero DC bias using a specially designed low noise current preamplifier with active drift compensation (Basel Electronics Lab) ensuring $V_{DC} \lesssim 5\,\mu V$.

Significant efforts were taken in order to obtain low electronic temperatures [9, 96–101]. The present device is mounted on a home-built silver epoxy sample holder inside a heavily filtered dilution refrigerator with 5 mK base temperature. Roughly 1.5 m of thermocoax wire is used in combination with two stages of home-built silver epoxy microwave filters [9] to efficiently filter and thermalize each measurement lead, resulting in electronic sample temperatures around 10 mK.

2.8.3 Numerical solution

Numerical solutions are obtained by solving the 1D Schrödinger equation using Numerov's method. The hard wall confinement forces the electronic wave functions to be zero at that boundary. The perpendicular magnetic field gives an additional parabolic confinement. Its minimum is shifted away from the hard wall by the GC position Y. The energy of a given solution is then changed iteratively until a vanishing wave function at the hard wall is obtained.

2.8.4 Data acquisition

A vector magnet (8 T solenoid and 4 T split-pair) is used to provide the external magnetic field for spectroscopy measurements. Exceptional device stability is required in order to perform those extremely time consuming B-field vs B-field maps in the main article. In particular, Fig 12a is composed of 3 individual data sets with a total measurement time of roughly 6 weeks. In order to reduce the measurement time, here the magnetic field B_z was scanned in a zig-zag fashion, i.e. taking data during ramping up and ramping down of B_z. However, due to the finite inductance of the magnet, a hysteretic behavior of the applied B-field results, which was accounted for by performing a non-linear correction to the measured data. The empty white spaces in Fig 12a (round corners) are due to the accessible combined field range of the vector magnet. A slight sample misalignment with respect to the $y-$ and $z-$direction is accounted for by tilting the experimental data in Figs. 11-13

2.9 Data and Code availability

The data of all the Figures of the main manuscript and the relevant code are available on a Zenodo repository (https://doi.org/10.5281/zenodo.1251622).

2.10 Supplementary Information

2.10.1 Momentum resolved tunneling spectroscopy

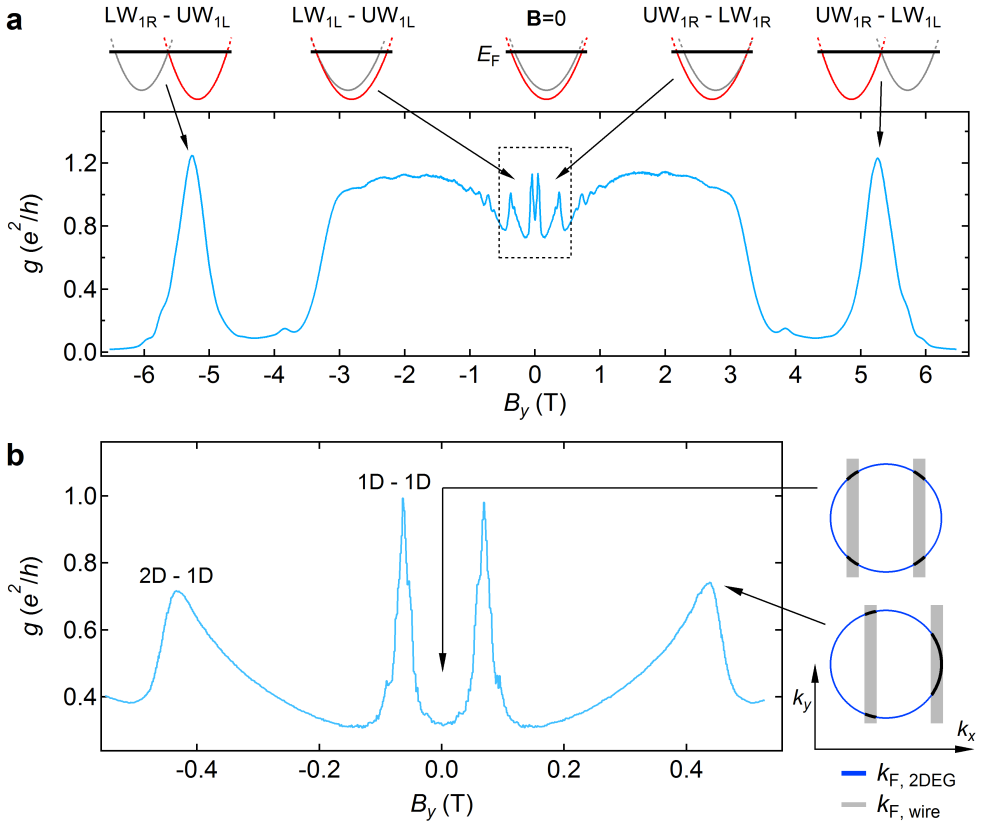

Figure 14: **Momentum resolved tunneling spectroscopy. a,** The zero bias tunneling conductance as a function of in-plane magnetic field B_y peaks whenever upper and lower wire Fermi-points overlap, indicated by black arrows. UW (LW) dispersions are shown in red (gray) for different magnetic fields. Black solid bars indicate the Fermi energy. **b,** Zoom - in of dashed rectangle in **a,** showing symmetric wire transitions and asymmetric 2DEG-wire transitions. Sketches schematically depict the wave function overlap (black) in momentum space at the Fermi energy between 2DEG (dark blue circle) and lower wire modes (gray lines).

2.10.2 Landau level formation

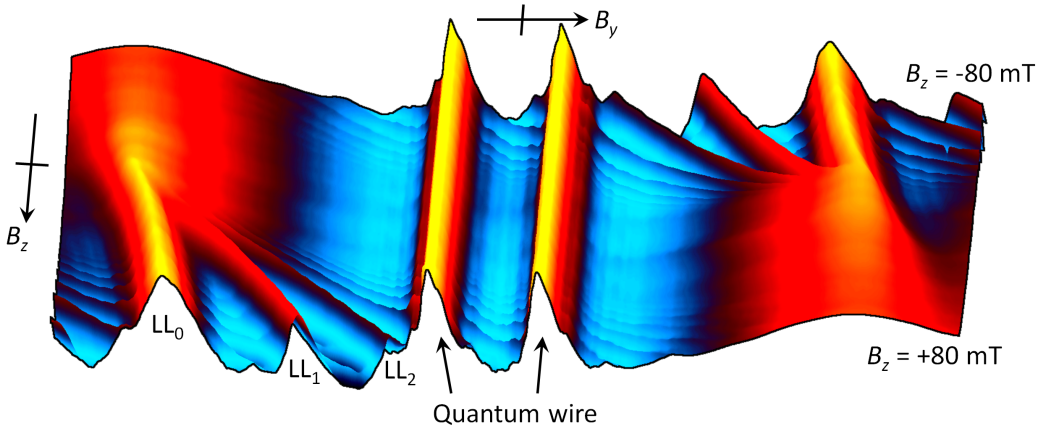

Figure 15: **Landau level formation. a,** Measured tunneling conductance as a function of magnetic fields B_y and B_z. The 2DEG to quantum wire transition is observed to fan out into individual resonances in presence of a small perpendicular magnetic field, signaling the formation of discrete edge states. The underlaying Landau levels, LL_0, LL_1, and LL_2 for the first three edge states are indicated.

2.10.3 Numerical solutions for hard wall confined Landau levels

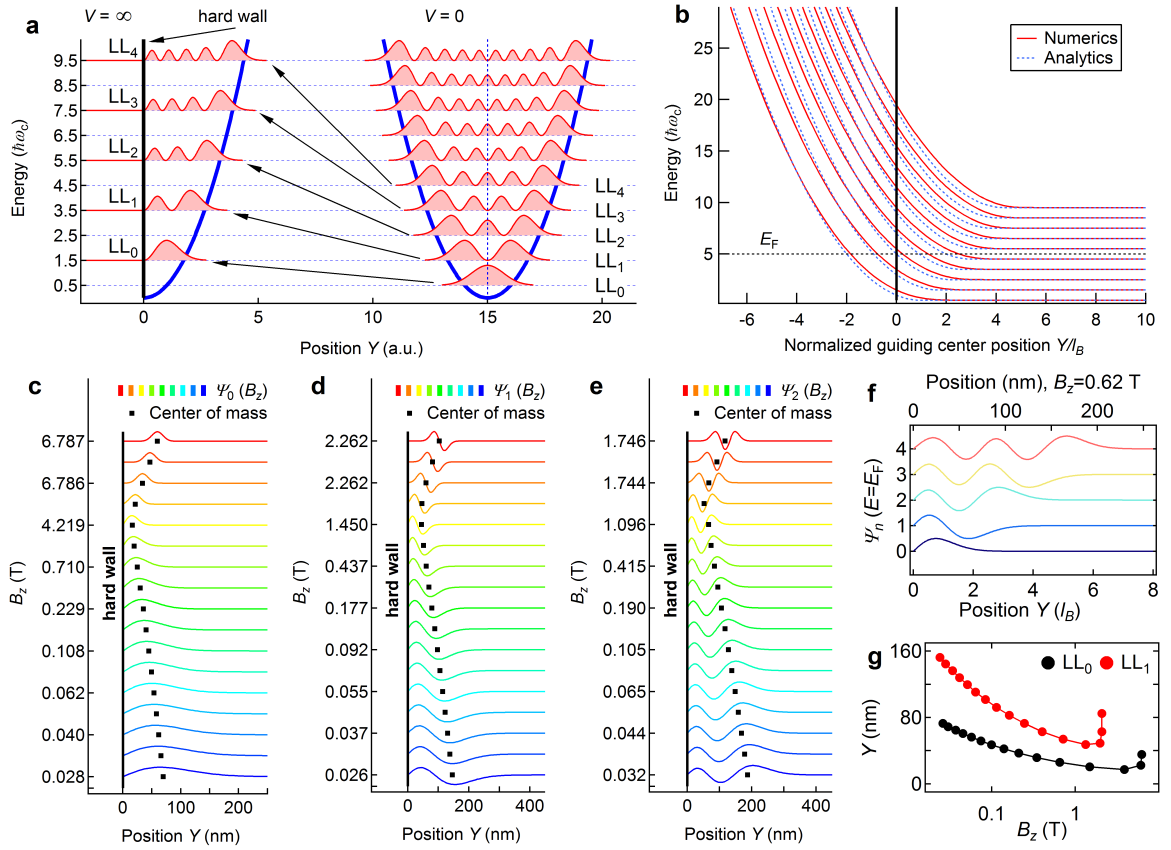

Figure 16: **Numerical solutions for hard wall confined Landau levels.** **a**, LL wave functions squared (red) in the bulk, and for the case when the GC is placed exactly at the edge of the sample (bold black). Blue parabolas denote the magnetic field confinement. **b**, Numerical (red) and analytical solution from the main text (blue) for the energy evolution of LLs as a function of GC position close to the hard wall. **c-e** Evolution of the electron wave function at the Fermi energy with perpendicular magnetic field B_z of LL_0, LL_1, and LL_3, respectively. Hybridization with the upper quantum wire (solution of the Schrödinger equation for same confinement problem) would lead to an additional node in the wave function, as illustrated in Fig.1**e** of the main manuscript. **f** Wave function for all five LLs at $E_F = 5\hbar\omega_c$ ($B_z \approx 0.62\,\mathrm{T}$ for the present sample). **g** Center of mass (CM) B_z evolution for the lowest two LLs.

2.10.4 Edge states at the hard wall

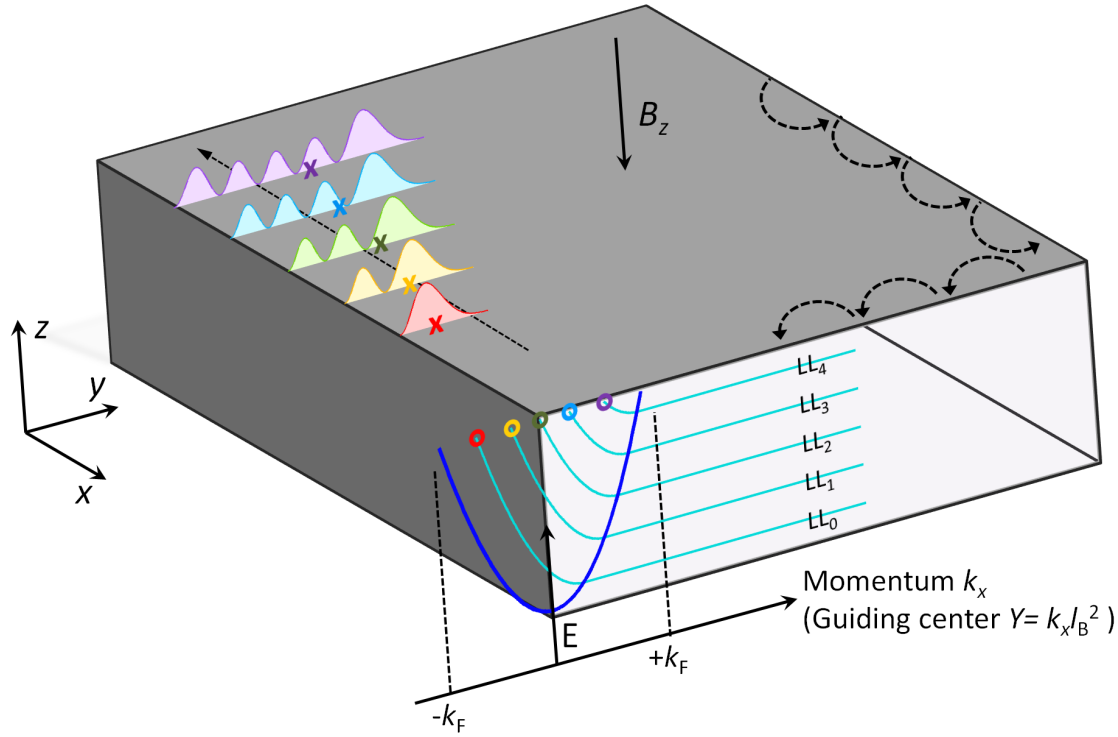

Figure 17: **Edge states at the hard wall.** Schematic representation of the sample showing the Landau level dispersions in light blue for states propagating along the negative x-direction at the left sample edge (see black coordinate system). The edge states are formed at the intersection with the Fermi level. The corresponding momenta (GC positions) are indicated by colored circles. The wave functions squared are also shown and reside entirely within the sample. The hard wall confinement separates the GC positions of edge states (colored circles) from their wave function CM positions (colored crosses) at the sample edge. Classical cyclotron orbits are shown as dashed semi circles.

2.10.5 Raw data of Fig.3a from the main text.

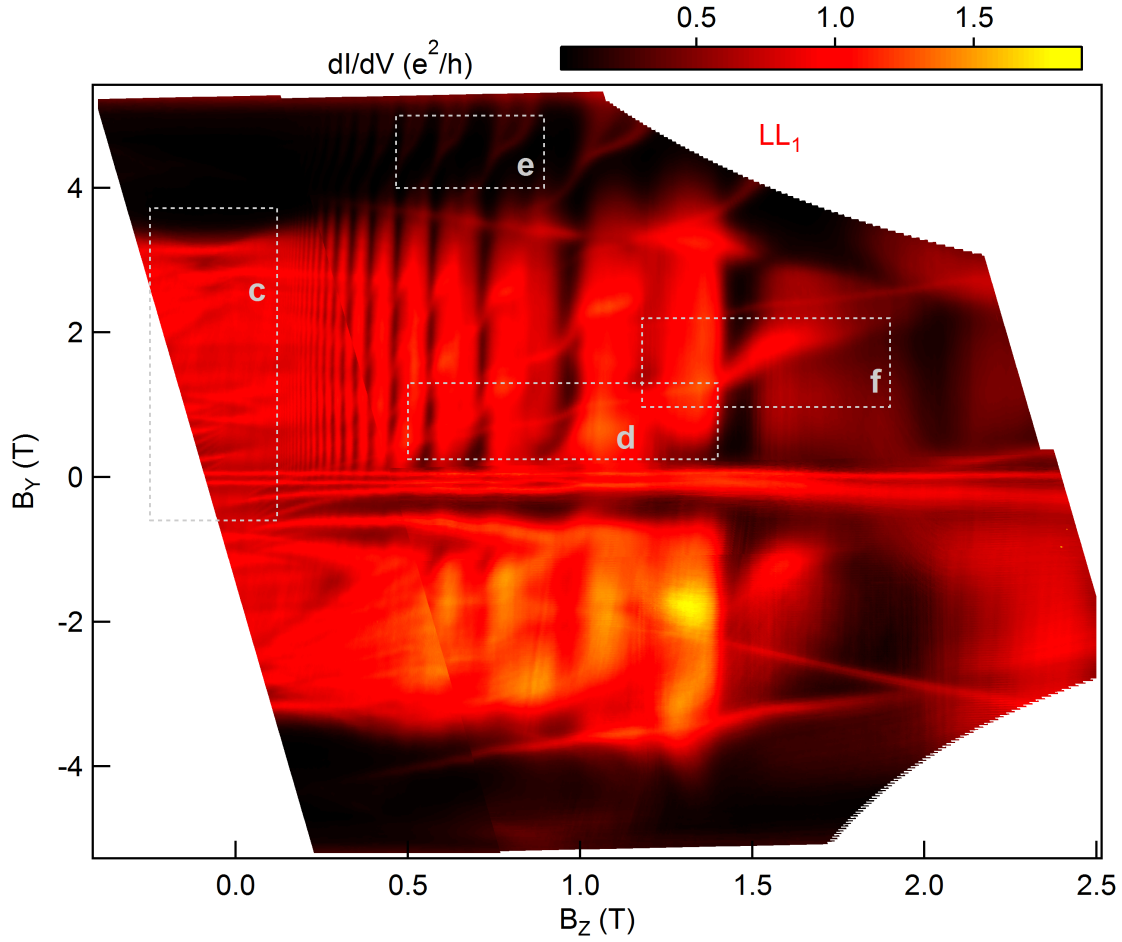

Figure 18: **Raw data of Fig.3a from the main text.** Differential conductance measured using standard lock-in technique as a function of perpendicular (B_z) and in-plane (B_y) magnetic fields. Small tilt corrects the slight misalignment of the sample with respect to the magnet axes. The data in Fig. 3a of the main manuscript was differentiated twice with respect to B_y compared to the set shown here.

2.10.6 Landau Level tunneling to different quantum wire modes

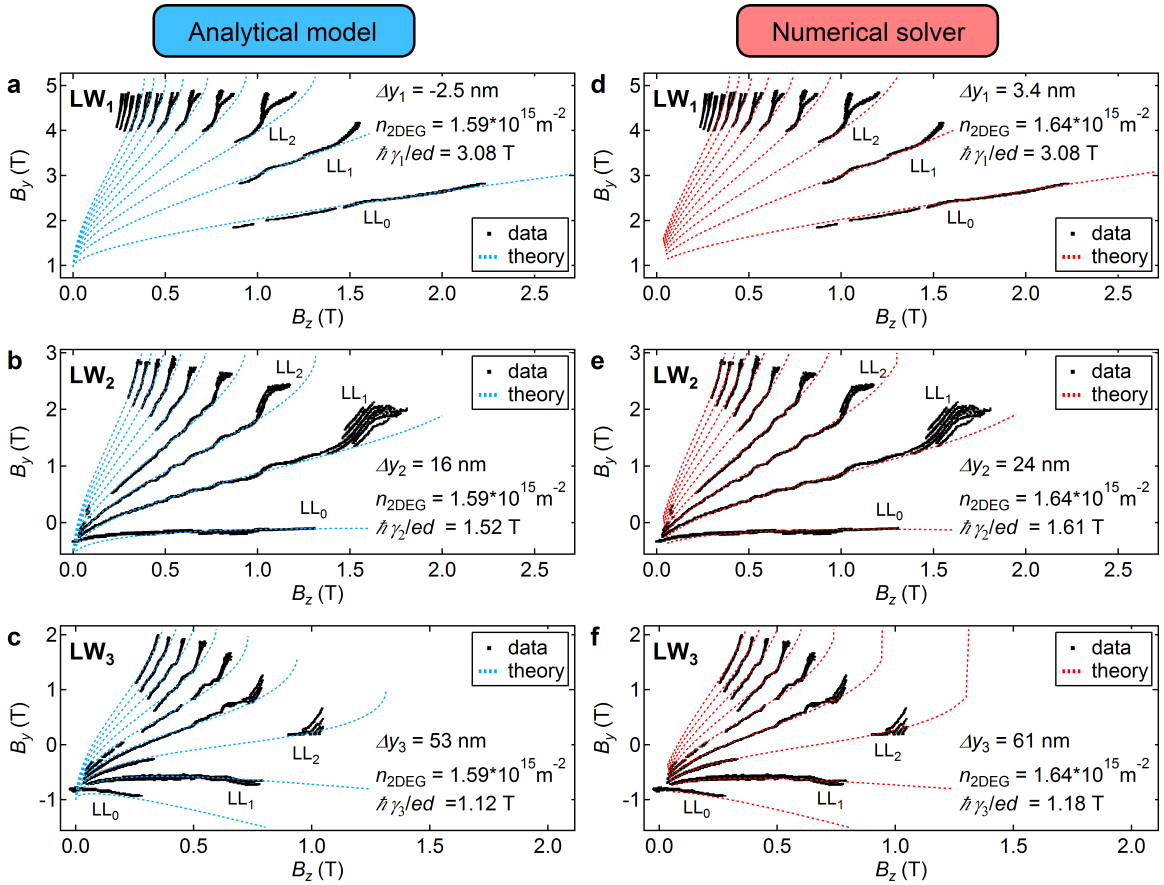

Figure 19: **Landau Level tunneling to different quantum wire modes.** Extracted resonances (black) for tunneling between Landau levels and the lowest quantum wire modes LW_1, LW_2, and LW_3 are shown in the top, middle and bottom panels, respectively. Superimposed are theoretical predictions using the analytical model from the main article (blue, panels **a-c**) as well as numerical calculations (red, panels **d-f**) performed with a one dimensional single particle Schrödinger solver.

2.10.7 Tunneling spectroscopy at zero perpendicular magnetic field.

Tunneling spectroscopy in cleaved edge overgrown quantum wires [73, 74] allowed for extraction of the quantum wire dispersion relation [75] and has revealed a number of exciting phenomena such as spin charge separation [66], charge fractionalization[13], and interaction effects beyond the Luttinger liquid picture [102]. The CEO wires are ballistic [103], exhibit clear conductance quantization [65], and show a number of other Luttinger liquid signatures [14], such as e.g. ubiquitous power laws [77, 78] or interaction induced helical order of electronic and nuclear spin system [8, 67, 104]. As such CEO wires can serve as ideal momentum selective tunnel probes for the investigation of 1D systems such as the edge states in the integer quantum Hall regime.

In the tunneling spectroscopy configuration, shown in Fig. 1**c** of the main article, a surface gate depletes the two dimensional electron gas (2DEG) beneath and the adjacent upper wire (UW), while leaving a single conducting mode in the lower wire (LW), located beneath the UW. A magnetic field B_y, applied perpendicular to the plane spanned by the UW and LW (i.e. in the plane of the 2DEG), introduces a momentum kick to tunneling electrons, thereby shifting UW and LW wire dispersions with respect to each other. Supplementary Fig. 1 shows the zero bias tunneling conductance as a function of B_y, which peaks whenever upper and lower wire Fermi-points overlap (black arrows). Four such peaks are seen, corresponding to tunneling between counter-propagating electrons in the first UW and LW mode (either left or right movers) at $B_y = \pm 5.25\,\mathrm{T}$ or tunneling between co-propagating electrons at $B_y = \pm 65\,\mathrm{mT}$, in agreement with earlier experiments [13, 75]. A zoom-in for the low magnetic field region is shown in Supplementary Figure 1**b**. In addition to the co-propagating wire-wire transitions, appearing as symmetric peaks (symmetric with respect to their peak position) around $B_y = \pm 65\,\mathrm{mT}$ there is a second set of asymmetric peaks at $B_y = \pm 0.4\,\mathrm{T}$ with a sharp cut-off towards larger fields and a long tail at small field $|B_y| < 0.4\,\mathrm{T}$. While those peaks were previously assigned to tunneling among higher modes in the upper and lower quantum wire [13], the asymmetric peak shape suggests yet another origin. The

peak shape may be qualitatively explained with a 2DEG to quantum wire transition, where the zero bias tunneling intensity is given by the overlap (black segments in the schematics of Supplementary Fig. 1**b**) in momentum space of a Fermi circle from the 2DEG and a pair of vertical lines from the quantum wire with well defined momentum $\pm k_{\mathrm{F}}$ along the x-direction only, the direction of free propagation.

This scenario is confirmed in Supplementary Fig. 2 and Fig. 2 of the main article, where the 2DEG to quantum wire transition is observed to fan out into individual lines (Landau level formation) in presence of a perpendicular magnetic field B_z, while transitions among quantum wires remain unaffected.

2.10.8 Landau levels in Landau-gauge: Introduction and terminology.

In order to introduce the proper terminology the simple quantum mechanical problem of a free electron in the x-y plane, subject to a strong perpendicular magnetic field B_z, is briefly reviewed. We choose Landau gauge with the vector potential $\mathbf{A} = (-B_z \cdot y, 0, 0)$ giving a magnetic field $\mathbf{B} = \nabla \times \mathbf{A} = (0, 0, -B_z)$, and the sample edge runs along the x-direction. The Hamiltonian of the system reads

$$\hat{H} = \frac{(\mathbf{p} - e\mathbf{A})^2}{2m^*} = \frac{\hat{p}_y^2}{2m^*} + \frac{1}{2}m^* (\hat{p}_x + eB_z y)^2 \tag{6}$$

Here, $\mathbf{p}$ denotes the momentum operator with components $\hat{p}_x$ and $\hat{p}_y$, e is the elementary charge, and m^* the effective electron mass. Since $\hat{H}$ and $\hat{p_x}$ commute, $\hat{p_x}$ can be replaced by its eigenvalue $\hbar k_x$:

$$\hat{H} = \frac{\hat{p}_y^2}{2m^*} + \frac{1}{2}m^*\omega_{\mathrm{c}}^2 \left(y + \underbrace{k_x \cdot l_B^2}_{Y} \right)^2 \quad , \tag{7}$$

where we have introduced the cyclotron frequency $\omega_{\mathrm{c}} = eB_z/m^*$, the magnetic length $l_B = \sqrt{\hbar/eB_z}$, and $\hbar$ is the reduced Planck constant. The system consists of standard quantum harmonic oscillators, shifted in y-direction by the guiding center (GC)

position Y, giving rise to the well known energy spectrum $E_n = \hbar\omega_c(n + 1/2)$, and hermite-gaussian wave functions Ψ_n, see Supplementary Figure 3. We note that the GC Y intimately links the effective momentum along the x-direction to the y-displacement from the edge through $k_x = Y/l_B^2$, which is key to the momentum resolved LL spectroscopy performed here. This can simply be understood in terms of the classical Lorentz force: Upon e.g. moving an electron closer to the edge by an amount Δy it is subject to the Lorentz force $F = e\frac{\Delta y}{\Delta t}B_z = \frac{\hbar\Delta k_x}{\Delta t}$ and hence experiences a momentum kick $\Delta k_x = \Delta y\frac{eB_z}{\hbar} = \Delta y/l_B^2$.

Upon approaching the edge with the GC position Y, the hard wall introduces a sharp cut-off to the parabolic magnetic confinement. Placing the GC exactly at the hard wall, one obtains a particularly simple case, where the odd bulk LLs provide the exact solution for the "half-parabola" confinement problem (due to their node at the GC position), i.e. $\mathrm{LL}_n \rightarrow \mathrm{LL}_{2n+1}$ at the edge, see Supplementary Figure 3**a**.

2.10.9 Numerical solutions for Landau levels at sharp edges

In order to calculate the continuous evolution of LLs and their wave functions, we numerically solve the Schrödinger equation using Numerov's method for the parabolic confinement (from the magnetic field), partially chopped off by the hard wall (depending on the GC position).

We normalize the energy by substituting $\hbar\omega_c = 1$ and the spatial coordinate by setting $l_B = 1$. This transforms the 1D Schrödinger equation into a unit-less form, which is then solved in the real space interval $y = [0, 25]l_B$ (within the physical sample) for different GC positions $Y = [-7, 10]l_B$ (Supplementary Figure 3**b**). For a physical solution the wave function has to be zero at the hard wall and far inside the sample (exponential damping due to the magnetic field confinement), hence $\Psi(0) = 0$ and $\Psi(25) = 0$. For each GC position the energy is changed iteratively until a solution is found that satisfies the right boundary condition $\Psi(25) = 0$ with sufficient precision ($\Psi(25) \ll 1$ for a normalized wave function). However, in order to obtain faster

convergence, a more complicated method is implemented. Here we set $\Psi(0) = \Psi(25) = 0$ and calculate the wave function from both sides. This requires stitching together of the two halves such that the total wave function remains continuously differentiable. The procedure allows us to calculate the evolution of energy and wave functions versus the GC position (Supplementary Figure 3**b-g**).

Supplementary Figure 3**b** shows the numerically obtained energy evolution for the first 10 LLs (red) along with predictions from the analytical model (blue) described in the main text. While the analytical model generally agrees very well with the numerics, there are some discrepancies at low B-field (i.e. when the Fermi energy E_F is much larger than the cyclotron energy $E_\mathrm{c} = \hbar\omega_\mathrm{c}$) and close to depletion of individual LLs in the bulk.

Since all spectroscopy experiments performed here are done at zero bias, tunneling only involves electronic states close to E_F. Hence, we are interested in the GC position Y_n where LL_n intersects with the Fermi energy (Supplementary Figure 3**b**). Tracking these intersections as a function of B_z allows one to predict the real-space evolution of integer quantum hall edge states, shown in Supplementary Figure 3**c-e** on a non-linear scale for LL_0, LL_1, and LL_2, respectively. Since the total width σ_n of the n^{th} edge states scales with the magnetic length, $\sigma_n \approx 2l_B\sqrt{2n+1}$, LLs are slowly compressed towards the hard wall upon increasing B_z. However, once the respective filling factor is reached the corresponding LL moves abruptly back into the bulk and is magnetically depopulated (lifted above E_F). This is clearly visible in Supplementary Figure 3**g**, where the center of mass (CM) position (black dots in Supplementary Figure 3**c-e**) for LL_0 and LL_1 is shown as a function of B_z.

Comparing the wave functions of different edge states for $E_\mathrm{F} = 5\hbar\omega_\mathrm{c}$ (Supplementary Figure 3**f**), we note their spatial overlap, while corresponding GCs in Supplementary Figure 3**b** are well separated. This suggests massively improved measurement sensitivity by means of momentum resolved spectroscopy compared to real-space imaging of edge states using local probes.

The results of the numerical simulations are summarized in the schematic 3D representation of the sample shown in Supplementary Figure 4. The Landau level dispersions are plotted on the sample front side and describe propagation along the sample edge (x-direction, see coordinate system). The GC positions for the different edge states (intersection of the dispersion with the Fermi energy) are indicated with colored circles and reside outside the physical sample for edge states associated with Landau levels of low orbital index. The wave functions, on the other hand, are contained within the sample for all edge states, leading to a separation of GC position (colored circles) and edge state CM position (colored crosses) in samples with hard wall confinement.

2.10.10 Comparison of theory and experiment

Here we compare experimental data for tunneling to the first three lower wire modes (Fig. 3 in the main article) to both, theoretical predictions using the numerical Schrödinger solver described in detail in the previous section, and predictions using the analytical model introduced in the main text.

While calculating the LL dispersion in Supplementary Figure 3**b** requires only one free parameter, namely the 2DEG density n_{2DEG}, two additional parameters have to be introduced in order to compare theoretical predictions and experimental data. On one hand, each quantum wire mode has its specific density and consequently differing Fermi wave-vector. The corresponding momentum mismatch of quantum wire and 2DEG (i.e. the tunneling condition at $B_z = 0$) is compensated with the in-plane magnetic field B_y, thus vertically shifting Landau fans in the $B_y - B_z$ measurement plane for different wire modes (see Fig. 2 and Fig. 3 in the main article). On the other hand, the wire wave functions are of finite width and hence the mode-specific CM position y_n is slightly displaced from the hard wall towards the bulk of the sample, while the LL dispersions in Supplementary Figure 3**b** are calculated with respect to the sample edge. The displacement gives raise to an additional momentum kick $\hbar k = e y_n B_z$, linear in B_z, which for small y_n appears like a rotation of fan structures around the origin $\mathbf{B} = (0, B_y, B_z) = 0$.

A comparison between theoretical predictions and experimental data is shown in Supplementary Figure 6. While both, numerical solutions and analytical model agree well with the measured data, there are some discrepancies at low B_z, in particular for the analytical case. In addition, both theoretical models do not take the spin degree of freedom into account and hence do not reproduce the spin splitting, seen for large in-plane magnetic field $B_y \gtrsim 4.5\,\mathrm{T}$ in Supplementary Figure 6**a,d** and Fig. 3**e** in the main text.

Investigating the fitting parameters, we note that the 2DEG density $n \approx 1.6 \cdot 10^{15}\mathrm{m}^{-2}$

turns out to be the same for all data sets (for both, analytical and numerical model). This strongly supports the theoretical models used here, since the 2DEG density should not depend on the specific wire mode used as a spectrometer for imaging of the quantum hall edge states. Besides investigation of Landau levels, the fits in Supplementary Figure 6 allow us to reconstruct the quantum wire mode structure, i.e. determine their CM position. For the triangular confinement potential at the sample edge, the quantum wire modes rapidly decrease in sub-band spacing with increasing mode index, while their width (extension of the wave function) is expected to significantly increase. Indeed, the CM position for LW_1 is located very close to the sample edge, whereas the position for the second and third lower wire mode are displaced much more from the hard wall, see fitting parameters in Supplementary Figure 6. We note that for the analytical model Δy_1 turns out negative, which is unphysical for a sample with hard wall, i.e. this model effectively describes a situation with slightly weaker confinement.

3 Template-Assisted Scalable Nanowire Networks

M. Friedl[1], K. Cerveny[2], P. Weigele[2], G. Tütüncüoglu[1], S. Marti-Sanchez[3], C. Huang[4], T. Patlatiuk[2], H. Potts[1], Z. Sun[4], M. O. Hill[4], L. Güniat[1], W. Kim[1], M. Zamani[1], V. G. Dubrovskii[5], J. Arbiol[3,6], L. J. Lauhon[4], D. M. Zumbühl[1], and A. Fontcuberta i Morral[1]

[1] Laboratoire des Matériaux Semiconducteurs, École Polytechnique Fédérale de Lausanne, EPFL, 1015 Lausanne, Swizterland

[2] Department of Physics, University of Basel, Klingelbergstrasse 82, CH-4056 Basel, Switzerland

[3] Catalan Institute of Nanoscience and Nanotechnology (ICN2), CSIC and BIST, Campus UAB, Bellaterra, 08193 Barcelona, Catalonia Spain

[4] Department of Materials Science and Engineering, Northwestern University, Evanston, Illinois 60208, United States

[5] ITMO University, Kronverkskiy pr. 49, 197101 St. Petersburg, Russia

[6] ICREA, Pg. Lluís Companys 23, 08010 Barcelona, Catalonia, Spain

This chapter was published in *Nano Lett.* **18**, 2666-2671 (2018).

3.1 System Introduction

In the past few years, much progress has been made toward fabricating and scaling up qubit density to build universal quantum computing systems that could potentially outperform classical computers by quantum schemes [105–109]. The ideal qubit should combine long coherence times, fast qubit manipulation, and small size, while maintaining scalability to many-qubit systems. Long coherence times are fundamentally challenging to achieve in various qubit systems due to the presence of numerous forms of environmental noise, requiring operating temperatures in the range of a hundred millikelvin [110, 111]. A system, which has been proposed to be much more robust against such perturbations, is the topological qubit [112, 113]. This type of qubit, for example, composed of Majorana Fermions (MFs) [112, 114] or parafermions (MPFs) [115, 116], would have the inherent property of being topologically protected and would, thus, exhibit exceptionally long coherence times. Signatures of MF states have been observed experimentally in, among other systems, III-V semiconductor nanowires (NWs) in close proximity to an s-wave superconductor [117–119], while a few other groups have reported anomalous MF signatures in similar systems [120–122]. In general, these studies have focused on using III-V materials, such as InAs and InSb, due to their high spin-orbit coupling strength and g factor [123]. Current efforts are focused on performing the first manipulations of MFs to further verify theoretical predictions, for which low-disorder, connected 1D branches are required [124]. Gold-free and defect-free NW branches made of a high purity, high spin-orbit III-V material would be an ideal platform for manipulating MFs. Excellent progress has been made toward this goal with reports on the growth of monocrystalline gold-assisted InSb NW branches, which display a weak antilocalization due to the large spin-orbit interaction of the material, as well as a hard superconducting gap [125, 126]. Scalability is another important aspect of any future computation system, and on this front, the Riel group has recently demonstrated patternable ballistic InAs NW crosses through template-assisted growth on silicon [127].

Despite recent progress, a few challenges still exist with current methods to produce branched structures. The fabrication of NW networks and intersections has been explored for many years for classical computing by overlapping individual wires [128–130]. For MF applications, the stringent requirement of maintaining coherent transport across the intersection means that, currently, the most popular NW cross structures rely on the intersection of two gold-catalyzed NWs grown along two different <111> B directions, leading to an interface-free junction [131–135]. After growth, free-standing crosses are obtained, which then need to be transferred onto a separate substrate for further device fabrication, limiting the ultimate scalability. A scalable scheme would instead enable the NW growth and intersections to be realized directly on the final device substrate. At the same time, for future device integration, the use of gold seeds poses a problem for compatibility with CMOS technologies [134]. Here, we demonstrate a new approach to grow gold-free branched In(Ga)As NWs at the wafer scale by using GaAs NMs as templates.

Defect-free GaAs NMs of exceptional quality constitute the ideal templates for further In(Ga)As NW growth [136, 137]. Such structures have been successfully grown by, both, metal-organic chemical vapor deposition (MOCVD) and molecular beam epitaxy (MBE) using a gold-free selective area approach [138, 139]. The NMs are patternable at the wafer scale and can, additionally, be fabricated in the form of Y-shaped structures by growing along the three <11-2> directions on GaAs (111) B substrates [138]. When the growth of these GaAs NMs is followed by InAs, the InAs accumulates at the top of the NMs, forming In(Ga)As NWs along the NM vertex, as depicted schematically in Fig.20a.

Shown in Fig.20b is the progression of the NW growth, which initiates as InGaAs and then evolves to pure InAs for longer growth times. Combining the concepts of patterning NMs into Y-branches and performing In(Ga)As NW growth on top of GaAs NMs, Y-shaped In(Ga)As NW junctions can be obtained, as shown in Fig.20c,d. Our approach thereby enables the growth of gold-free branched NWs at the wafer scale.

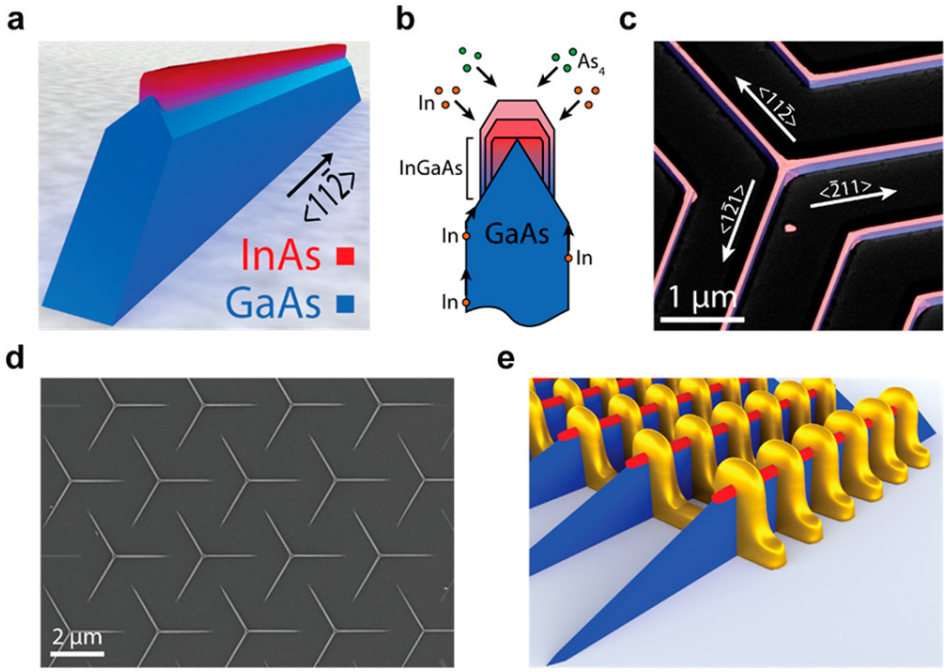

Figure 20: Growth of NWs on NMs. (a) Model of a single GaAs/InAs NM/NW structure. (b) Diagram showing NW growth progression. (c) A 30° tilted scanning electron microscope (SEM) image of a branched NM/NW structure taken with an energy-selective backscattered electron detector for z-contrast. The image is false-colored for visibility and annotated with relevant substrate directions. (d) SEM image of branched NW structures grown in a regular array. (e) Model of an array of contacted linear NM/NW structures used in magnetotransport measurements.

In this Letter, as the first step toward building MF devices based on this approach, we demonstrate the growth of low-defect linear Al(Ga)As NWs based on GaAs NMs. Magnetotransport measurements on an array of nanowires (depicted schematically in Fig.20e) demonstrate weak localization in the diffusive regime, suggesting quasi-1D quantum transport. This makes such NWs ideal candidates for future quantum computing schemes.

3.2 Nanomembranes as a Platform

Membranes with top ridges parallel to the substrate were grown, as described previously [139]. The InAs NWs were then grown for 200 s at an As_4 flux of 8×10^{-6} Torr, an In rate of 0.2 Å/s and a substrate temperature of 540 °C. This optimized substrate temperature yielded continuous InAs growth on top of the NMs. The details can be found in the Supporting Information. A Si dopant flux of 10^{13} atoms/cm^2/s was also

introduced to increase the conductivity of the NWs.

The NW morphology, composition, and structural quality were extensively characterized by correlated analysis using various electron microscopy techniques. These included electron energy loss spectroscopy (EELS) and atomic-resolution aberration-corrected annular dark field scanning transmission electron microscopy (ADF - STEM). The results were then coupled with geometrical phase analysis (GPA) to give strain information [140, 141], which, in turn, was fed into a semi-empirical model to understand the formation of the NWs from a theoretical standpoint.

Analysis of focused ion-beam (FIB) lamellas prepared perpendicular to the NW axis by ADF-STEM and correlated EELS (Fig.21a-c) show that 50 nm diameter InAs NWs form on the 250 nm tall GaAs NMs. The InAs material preferentially accumulates along the top ridge of the GaAs NM, forming the NW, which is primarily InAs with a 20 nm thick intermixed InGaAs region at its base. (See the Supporting Information for details.) This InGaAs region likely occurs due to strain-mediated intermixing with the GaAs NM below, as has been observed in InAs quantum dots on GaAs [142]. It is important to note that we observe no In signal from the NMs; the faint signal seen in the EELS map is believed to be created during the FIB cutting by a combination of redeposition of the TiO_x protective layer and surface diffusion of the highly mobile In adatoms. Looking instead at the NW facets, as seen in Fig.21d, the resulting InAs NW structures are terminated by two (110) facets on the sides and have a single flat (111) top facet. The appearance of this (111) facet, instead of the two {113} facets as in the GaAs NMs, can be explained by the higher As_4 flux used in the InAs NW growth [143, 144].

No defects were observed when viewing this transverse lamella in atomic-resolution ADF-STEM mode. As strain along the NW axis was predicted to be more difficult to relax than in the transverse direction, a second FIB lamella was prepared parallel to the axis of the NW and also imaged using atomic-resolution ADF-STEM. Here, a few misfit dislocations were observed near the InAs/GaAs interface, with an estimated

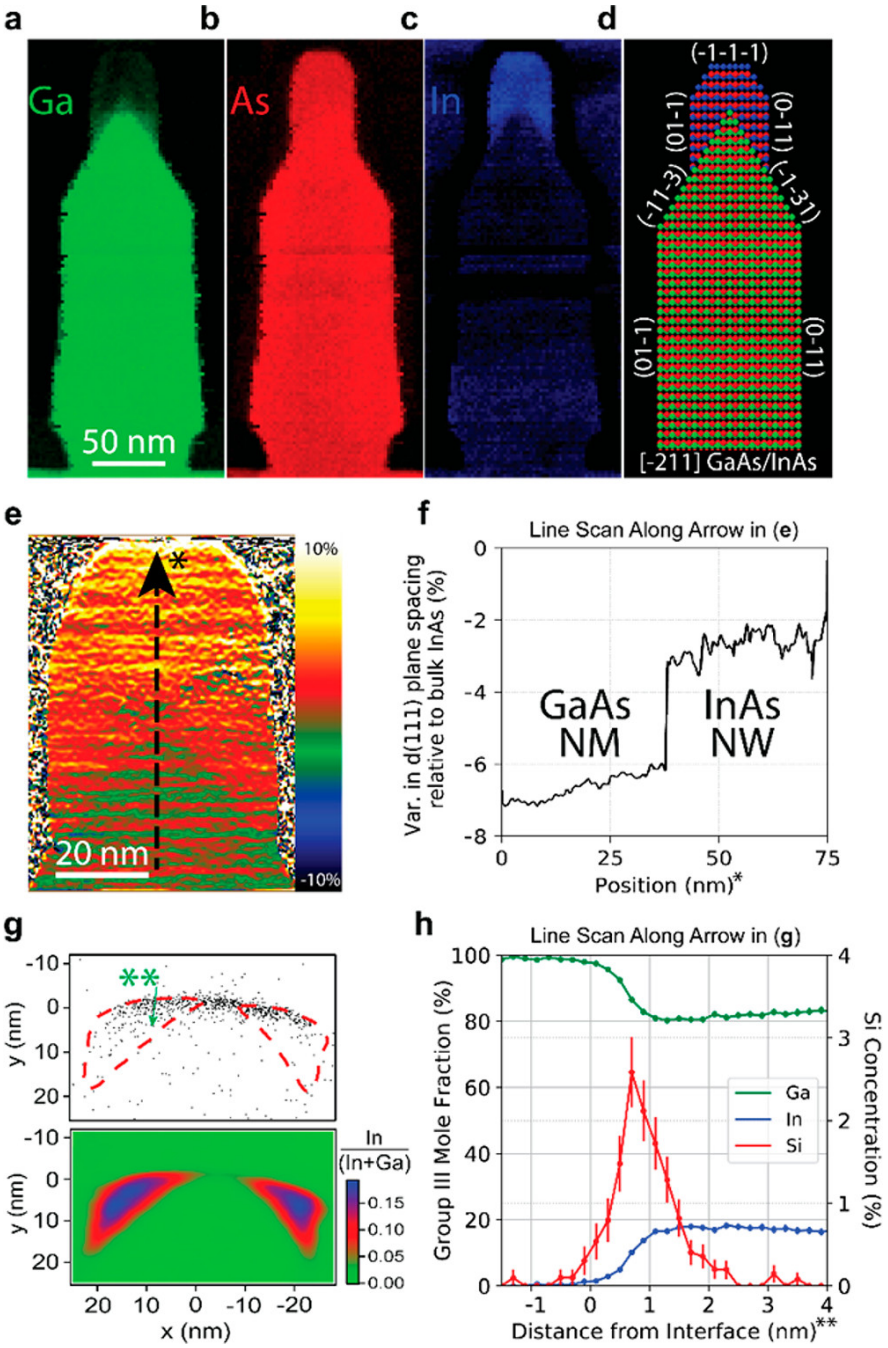

Figure 21: TEM and APT analysis. (a-c) EELS maps with elemental contrast of a NM/NW cross section. Note that the overlap of the In EELS signal with the Ti signal from the TiO_x capping layer has caused an anomalous background of In within the NM, which is not physical. (d) Atomic model showing faceting of the NM/NW heterostructure. (e) GPA map of the InAs NW region. (f) Line scan along arrow in panel e. (g) APT map of scaled-down NWs used in electrical measurements showing In concentration (lower map) and accumulation of Si dopant atoms (black dots) at the surface of the NW with In isoconcentration lines as a guide to the eye (upper map). Note that, since the NWs were capped with GaAs for APT analysis, the measured In concentration can be considered as a lower bound for the uncapped structures. (h) Proxigram line scan along the dashed arrow in panel g showing Si accumulation on the NW top facet and In concentration within the NW.

density of approximately 100/μm, as described in the Supporting Information. This constitutes a 40 % reduction in dislocation density with respect to the equivalent 2D growth of InAs on GaAs and at least three times improvement with respect to the twin density typically observed in self-catalyzed InAs NWs [145–147].

Turning now to explaining the morphology of the structures, an analytical model shows that the surface and strain energy minimization play the most important role in driving the NW to adopt the observed shape (Supplementary Information). By taking advantage of the atomic resolution offered by ADF-STEM images, GPA was performed on the initial FIB lamella cut perpendicular to the NW axis. Looking specifically at the (111) plane spacing, a substantial 2-3 % residual compressive strain is observed within the NW as shown in Fig.21e, with the corresponding line scan given in the Fig.21f. Using this strain value, a semiquantitative model was developed to describe the NW formation energy, taking into account the InAs/GaAs surface energies and the InAs elastic strain energy. The total energy of the system was then minimized with respect to the NW aspect ratio. Interestingly, the experimentally observed aspect ratio coincides with that of the theoretical minimum energy shape, suggesting that the NW shape is simply driven by energy minimization (see Supplementary Information for details).

3.3 Electrical Transport in the Mesoscopic Regime

To bring the NWs into the 1D electrical transport regime, they were downscaled to 20 nm diameters by narrowing the GaAs NMs by using smaller SiO_2 openings and shorter growth times for less lateral growth. The resulting NWs were smaller, both, laterally and vertically, resulting in intermixed InGaAs NWs, as depicted for small diameter NWs in the growth progression diagram in Fig.20b. These results were confirmed by performing atom probe tomography (APT), which additionally yielded information about the Si dopant distribution.

The APT analysis confirmed the presence of an InGaAs NW„ while also uncovering

signs of dopant rejection during crystal growth, causing an accumulation of Si atoms at the NW surface. Figure 21g shows a typical APT map of the In mole fraction and Si dopant distribution. A quantitative composition profile of the NW surface was extracted in the proximity histogram (proxigram) shown in Fig.21h. In this sample, the NW group III mole fractions are 17 % In and 83 % Ga. (Additional maps in Supplementary Information section.) Analysis of different InGaAs samples by APT tomography under similar conditions shows a slight tendency toward preferential In evaporation. In addition, a GaAs capping layer was deposited on the PT sample after the NW growth, which may have enhanced the Ga intermixing [148]. For these reasons, we consider the In mole fraction in this NW as a lower bound. Although a Si flux was present during InAs NW growth, the Si atoms are not homogeneously distributed throughout the NW (Fig.21g). The Si atoms instead appear to accumulate preferentially at the (111) growth interface, resulting in a quasi-remotely doped structure.

The electrical properties of the NWs were explored through multi-contact resistance measurements on an array of NWs, for which an example device is shown in Fig.22a. An array of 34 NWs, comparable to those on which APT was performed, was used for these tests as a way to obtain the average response for many devices. Standard four-point measurements were then carried out at room temperature before moving to low-temperature magnetoconductance transport experiments.

Room-temperature transmission line measurements, shown in Fig.22b, gave linearly scaling and repeatable resistances, suggesting that a good-quality contact was achieved. A control sample without InAs NWs (as shown in green in Fig.22b) shows an increase of resistance by five orders of magnitude, directly proving that the observed conduction occurs due to the InAs deposition. Device behavior remained linear and ohmic down to 4.2 K, albeit with an increased contact resistance.

Magnetoconductance measurements at 1.5 K revealed a zero-field minimum of conductance consistent with weak localization (WL) behavior, as shown in Fig.22c [149]. The

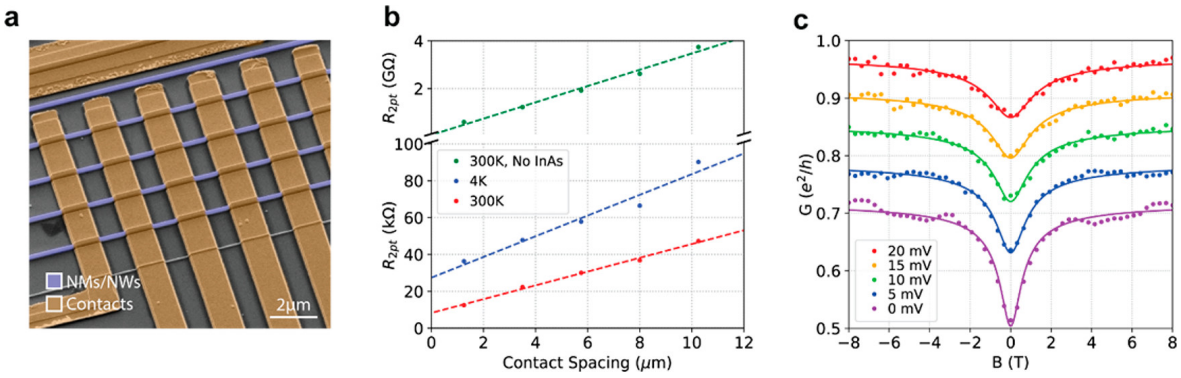

Figure 22: Magnetotransport measurements. (a) False-colored SEM image of four InAs/GaAs NW/NMs contacted in parallel. (b) Transmission line measurement to extract contact resistance and resistivity (per NW) at 4 and 300 K, in comparison with NMs without the InAs deposition step. (c) Average differential conductance per NW as a function of magnetic field perpendicular to the NWs for a range of bias voltages measured at 1.5 K for a 1.25 μm long NW segment. The traces for biases above 0 mV are offset for clarity.

conductance of the devices was measured under constant bias, while the magnetic field was applied perpendicular to the substrate and was swept from -8 to 8 T. This analysis indicated conduction in the quasi-1D transport regime and elucidates important quantum figures of merit, such as coherence length l_ϕ, mean free path l_e, and spin-orbit length l_{so}.

A coherence length l_ϕ of 130 nm and a lower bound on the spin-orbit length l_{so} were obtained by fitting the experimental data. The system was assumed to be in the diffusive regime with the electron mean free path $l_e \ll W$, with W being the width of the conducting channel, estimated from the APT results to be about 20 nm. In this regime, l_e is thus constrained to be a few nanometers due to the large amount of dopant and surface scattering. A simple quasi-1D model for the quantum corrections to the conductivity in the diffusive limit (details in Methods) gives an excellent agreement with the data and yields l_ϕ 130 $\pm$ 4 nm near zero bias, as shown in the solid traces in Fig.22c. In the absence of weak anti-localization and adding spin-orbit coupling to the model (see Supplementary Information section), a lower bound for l_{so} of 280 nm is estimated. Some small variations in the conductance at large magnetic fields are noticable, presumably signatures of conductance fluctuations, which are strongly suppressed due to averaging from the parallel NW arrangement as well as the relatively

short coherence length.

These initial results show that the electron confinement at the top of NWs grown on NMs is sufficient to produce quasi-1D conduction. These NWs could, therefore, be viable hosts for Majorana bound states, provided that two main potential obstacles are addressed. First, a NW made of higher spin-orbit material, such as pure or nearly pure InAs or InSb, will be required; i.e., intermixing should be reduced or eliminated. This will be apparent by the observation of weak anti-localization instead of weak localization. Second, impurity, interface, and alloy scattering need to be reduced, such that l_e transitions from the diffusive to the ballistic transport regime.

3.4 Conclusion and Outlook

The fast-growing field of quantum computing and the promise of robust, topologically protected qubits with III-V NWs drives the pursuit of scalable approaches to branched NW networks. We have described a path forward, using GaAs NMs as templates for the In(Ga)As NW growth. By exploiting strain in the highly mismatched InAs/GaAs system, continuous, low-defect NWs were formed. We have further observed weak localization, demonstrating that such NWs can provide sufficient confinement to achieve quasi-1D conduction. Our gold-free wafer-scale approach to branched NWs serves as a platform for future investigations into 1D transport and quantum computation with III-V NW networks with many exciting possibilities. From the MBE growth perspective, using GaSb NMs already described by other groups to grow InSb NWs would be interesting due to the higher g-factor of InSb [123, 150]. Alternatively, suitable plastic strain relaxation, for example, by interfacial misfit array formation [151] may enable GaAs NMs to be viable templates for InSb NW growth. At the same time, the growth of new kinds of structures with additional functionalities is another avenue to explore, including, for example, research into parafermion devices by stacking multiple NWs on top of each other [116]. The wealth of intriguing new possibilities and approaches offered by template-assisted III-V NW growth makes this method an

important step toward realizing a scalable quantum computing scheme based on NW topological qubits.

3.5 Methods

3.5.1 Substrate Preparation

Undoped GaAs (111) B substrates were prepared by first depositing 25 nm of SiO_2 by the plasma enhanced chemical vapor deposition (PECVD). This was followed by e-beam lithography, using ZEP resist and low-temperature development to achieve low line edge roughness [152]. Subsequent dry etching with fluorine chemistry was used to etch the SiO_2 down to the GaAs surface, and a final wet etch in a dilute buffered HF solution helped remove any remaining oxide. This yielded openings varying from 30 to 100 nm in width and 10-20 μm in length, depending on the e-beam pattern.

3.5.2 Growth

The nanostructures were grown in a DCA D600 Gen II solid-source MBE. The optimal growth of the GaAs/InAs NM/NW heterostructures was found to be at a temperature of 630 °C/540 °C (as measured by the pyrometer), As flux of $4 \times 10^{-6}/8 \times 10^{-6}$ Torr and Ga/In deposition rates of 1.0/0.2 Å/s, respectively. The NMs were typically grown for 30 min (180 nm nominal 2D thickness), while the InAs NWs were grown for 200s (4 nm nominal 2D thickness).

3.5.3 (S)TEM

The cross sections of the NMs were prepared by FIB milling normal to the substrate surface and investigated by ADF-STEM in a probe corrected FEI Titan 60-300 keV microscope operated at 300 keV. The elemental maps were obtained by using an EELS coupled to a Tecnai F20 microscope.

3.5.4 Contacting

Conctacts were patterned by e-beam lithography followed by dual-angle evaporation of 14/80 nm of Cr/Au for good side-wall coverage. Before metallization, an O_2 plasma clean and a 6 min ammonium polysulfide etch at 40 °C were used to ensure a clean, oxide-free contact [153].

3.5.5 Quantum Transport Model

The conductance of the NW is described as

$$\Delta G = -\frac{2e^2}{hL}\left(\frac{1}{l_\phi^2}+\frac{1}{l_B^2}\right)^{-1/2}, \tag{8}$$

where L is the spacing between the contacts and l_B is the magnetic dephasing length given by $l_B = \sqrt{D\tau_B}$, with D as the diffusion constant ($D_{1D} = v_F l_e$ for 1D diffusion). In this limit, the magnetic dephasing time τ_B is given by $\tau_B = 3l_m^4/W^2D$, where $l_m = \sqrt{\hbar/eB}$ is the magnetic length [149, 154, 155].

3.5.6 GaAs Capping

After the growth of the NW/NM heterostructures, a 30 nm GaAs cap was deposited in situ by MBE at 400 °C. In the middle of this GaAs cap, the In shutter was opened for 10 s, making a few-monolayer insertion of $In_{0.16}Ga_{0.84}As$, indicating the midpoint of the GaAs cap. The NW/NM heterostructures were then coated with a 110 nm GaAs layer [156] using ion-beam sputtering at 9 kV and 7.5 mA for 1 h. The capping layer protected the sample from damage caused by the ion beam during FIB.

3.5.7 Atom probe tomography

A standard lift-out method [156, 157] was performed in a FEI Helios dual-beam FIB microscope with a micromanipulator and the as-prepared wedge-shaped samples were

welded onto Si microposts. Finally, the needle-shaped APT specimens were obtained by ion-beam annular milling. APT was performed with a local-electrode atom-probe (LEAP) 4000X Si tomograph (Cameca, Madison, WI) at a sample temperature of 40 K and a background pressure of 3×10^{-11} Torr. An ultraviolet focused laser with a wavelength of 355 nm was used to evaporate the sample atoms into ions, at a pulse rate of 250 kHz and detection rate of 0.7 %. The pulse energy was gradually changed from 1.2 pJ to 0.8 pJ during the evaporation process. The data was recontructed using IVAS 3.8.1 to provide a 3D composition profile. SEM images of the nanotips taken in the FIB were used to guide the choices of the reconstruction parameters.

3.6 Supporting Information

3.6.1 Growth Details

The InAs NWs were grown by MBE on top of defect-free GaAs NMs. The growth of the NMs was performed according to an approach published previously, using selective area epitaxy [158]. Following the growth of the GaAs NMs at 630 °C, the substrate temperature was decreased to 540 °C and InAs was overgrown on top of the GaAs NMs. During the InAs growth, an arsenic flux of 8×10^{-6} Torr was used along with an indium rate of 0.2 Å/s. This was typically grown for 200 s, yielding a nominal depositied InAs thickness of 4 nm.

3.6.2 Temperature Dependence of InAs

As a first step during the growth optimization, two temperature series were performed. Some representative SEM images from these series are shown in Fig.23. Here, we see that at low temperatures the InAs grows as clusters on the sides/edges of the membrane rather than as a single coherent wire. This side growth is possibly due to the fact that at low temperatures the adatoms have shorter diffusion lengths and, thus, are not able to find the optimal (lowest energy) positions, i.e. on the vertex. As the temperature

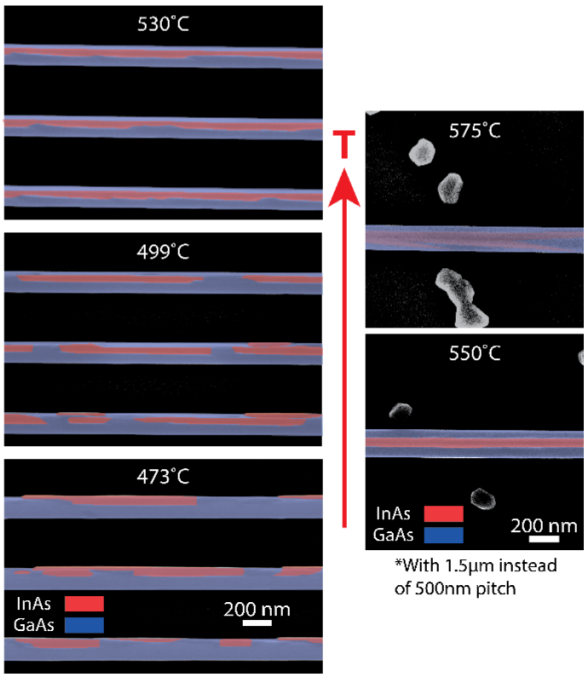

Figure 23: **Temperature Dependence on InAs Growth** Top-view SEM images showing temperature dependence of InAs growth on top of GaAs NMs. False-colored to show InAs islands as confirmed by energy-dispersive spectroscopy (EDS) measurements.

is increased, the InAs islands begin to merge and a coherent nanowire begins to form above 530 °C.

In a second series, on a substrate with NM pitches of 1500 μm, the growth temperature was increased further to observe the limit of the NW growth. At temperatures above about 550 °C, the InAs no longer grows on the NMs. The optimal growth temperature for achieving continuous coherent InAs NWs has, therefore, been found to be in the range of 540-550 °C.

3.6.3 Width/Pitch Dependence of InAs

The influence of the GaAs NM geometry on the nanowire growth was also explored on a single substrate grown at 530 °C. This comparison is shown in Fig.24. From this analysis, we see that thinner membranes stabilize the nanowire, making it more uniform. Increasing the pitch also improves the uniformity of the InAs NWs, though this is likely due to the fact that the NMs are thinner at larger pitches. NMs at larger pitches, due to less efficient arsenic capture, grow more slowly in, both, height and

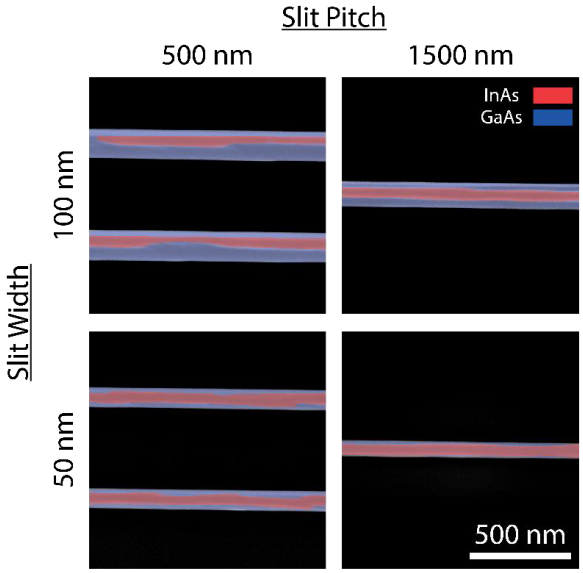

Figure 24: **Geometry Dependence on InAs Growth** Top-view SEM image comparison of InAs NW coverage of the GaAs NMs for various pitches and widths of the openings in the SiO_2 mask. The InAs/GaAs has been false-colored for visibility.

width. The optimal NM geometry is, therefore, achieved at large pitches (>1 μm) with mask openings as thin as possible, in order to achieve very thin GaAs NMs. For sufficiently thin NMs, the InAs covers the whole top surface of the GaAs NM and grows as a single NW with uniform thickness.

3.6.4 Raman Spectroscopy

Raman spectroscopy was performed on an InAs/GaAs device, in order to measure strain. This was performed using 488 nm laser excitation at a power of 200 μW and 1 μm spot size. A representative spectrum is shown in Fig.22, where five main peaks can be distinguished and are summarized in the table in Fig.26.

Here, the expected SO phono peak was calculated assuming a cylindrical InAs nanowire with a diameter of 30 nm [160]. From the table, it can be seen that most peaks are measured within about 4 cm^{-1} of the expected frequency. However, the InAs LO peak shows a significant shift of 7 cm^{-1} due to strain [161]. Additionally, the shape of the LO phonon peak is broader than the expected Lorentzian fit, which we take as evidence of inhomogeneous broadening due to inhomogeneous strain that is also seen in finite

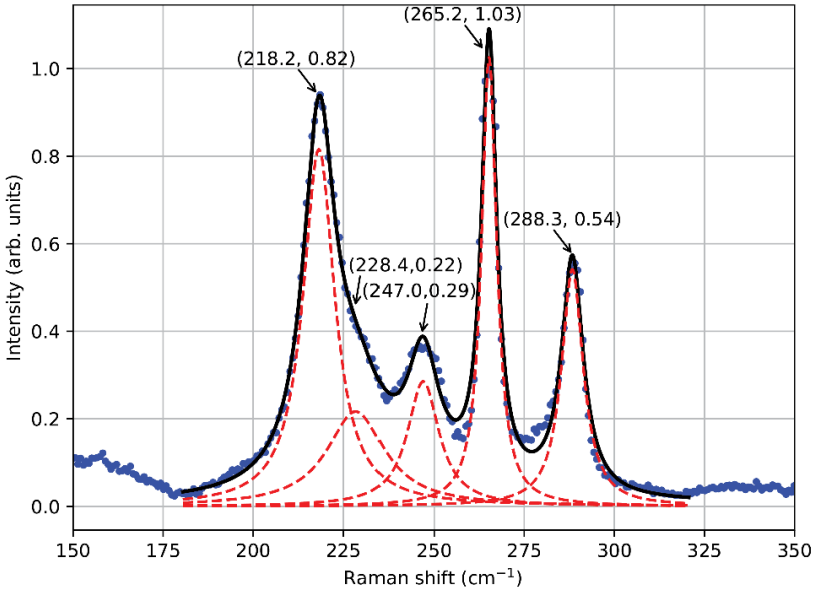

Figure 25: **Raman Spectrum of InAs NW on GaAs NM.**

Peak Name	Expected	Found
InAs TO	217.8 cm^{-1}	218.2 cm^{-1}
InAs SO [1]	240.0 cm^{-1} (bulk) 226.6 cm^{-1} (60 nm NW)	228.4 cm^{-1}
InAs LO	233.9 cm^{-1} 240.2 cm^{-1} [2]	247.0 cm^{-1}
GaAs TO	267.7 cm^{-1}	265.2 cm^{-1}
GaAs LO	291.2 cm^{-1}	288.3 cm^{-1}

Figure 26: **Table of expected and measured Raman peaks.** [159, 160]

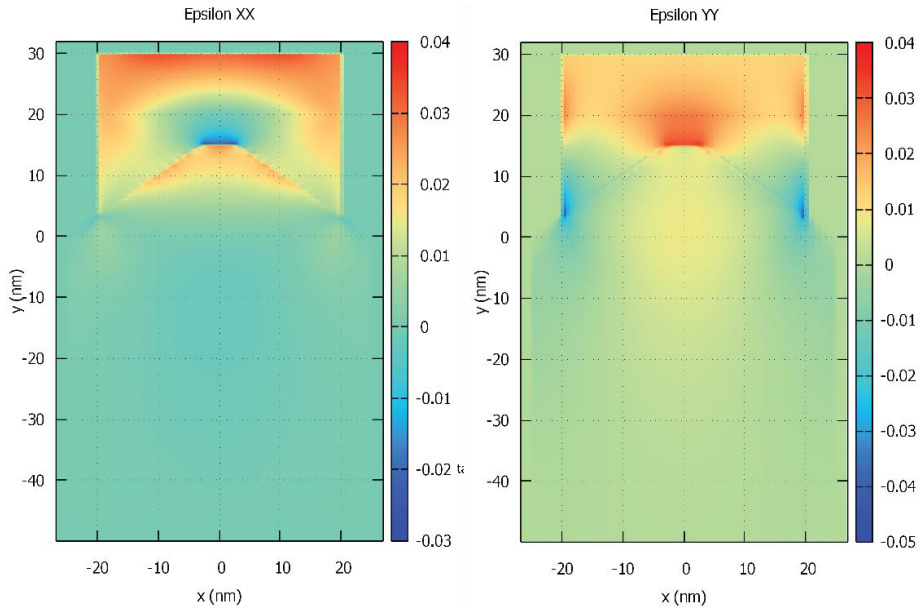

Figure 27: **Simulations of strain tensor in x and y directions.**

differences simulations (see Fig.27).

3.6.5 Strain Simulations

The strain and electrical properties of the InAs nanowires were simulated using nextnano^3 (v1.9.2), a Schrödinger-Poisson-current finite differences solver [162]. The simulation was set up allowing for relaxation of the structure into the air spaces around the NW/NM. An unstrained GaAs substrate was imposed on the system at the base of the simulation.

The resulting strain tensor maps are shown in Fig.27. It can be seen that the strain in the InAs nanowire is about 2-3 % on average. This agrees well with what was seen in HR-STEM GPA and Raman spectroscopy.

Note that, while the actual GaAs NMs are hundreds of nanometers tall, the simulations used a 50 nm tall NM to reduce the computational expense. This approximation is justified because, as seen in the simulations, below about 30 nm from the top of the NM, there is nearly no strain remaining in the GaAs NM.

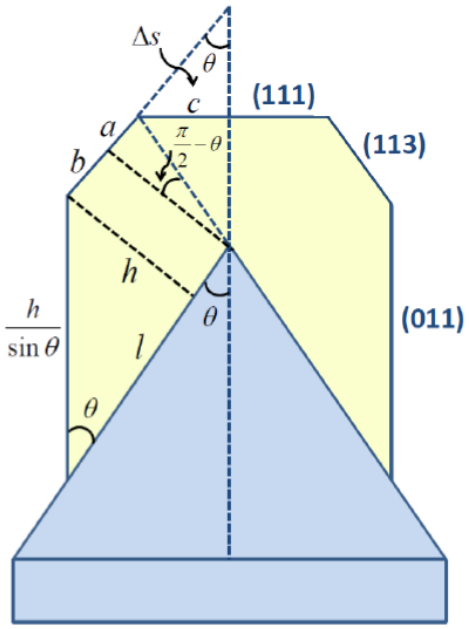

Figure 28: **NW model geometry** System geometry showing the geometrical parameters used in modelling the free energy of forming the InAs NW.

3.6.6 Growth Model

We provide a model to explain the preferential accumulation of InAs on the top ridge of the NM. Consider the NM/NW geometry shown in Fig.28 in the cross-sectional view perpendicular to the NM.

We assume that the InAs NW facets are composed of vertical, horizontal, and inclined facets of the (011), (111), and (113) families, respectively (see Fig.28), and that the inclined NW facets are replaced by the horizontal facets at the crossing point of the initial NM facets with the inclined NW facets, as suggested by Fig.21 of the main text. From geometrical considerations, we have $a = h\cot 2\theta$ and $b = l - h\cot\theta$, with θ as the taper angle of the NM, hence

$$b + a = l - h(\cot\theta - \cot 2\theta). \tag{9}$$

The (131) facet of the InAs of width $b+a$ and surface energy $\gamma^{(131)}_{InAs}$ replaces the initial facet of the GaAs NM of width l and surface energy $\gamma^{(131)}_{GaAs}$. Additionally, the NW formation creates the InAs-GaAs interface of width l and interfacial energy $\gamma^{(131)}_{InAs-GaAs}$. We

also create the vertical facet of height $h/\sin\theta$ having the surface energy $\gamma_{InAs}^{(011)}$, and the horizontal facet of width c and surface energy $\gamma_{InAs}^{(111)}$. From geometrical considerations,

$$c = h\frac{\sin\theta}{\sin 2\theta}. \tag{10}$$

Summarizing all these surface energy terms and using $\cot 2\theta = (1/2)(\cot\theta - \tan\theta)$ and $\sin 2\theta = 2\sin\theta\cos\theta$ in (8) and (9), respectively, the surface energy change per length $2d$ (where d is the length of the initial NM) equals

$$\Delta F_{surf} = \left[\gamma_{InAs-GaAs}^{(131)} + \gamma_{InAs}^{(131)} - \gamma_{GaAs}^{(131)}\right] l + \left[\frac{\gamma_{InAs}^{(011)}}{\sin\theta} - \frac{1}{2}\gamma_{InAs}^{(131)}(\tan\theta + \cot\theta) + \frac{\gamma_{InAs}^{(111)}}{2\cos\theta}\right] h. \tag{11}$$

Grouping the brackets into C_1 and C_2, we can write

$$F = C_1 l + C_2 h. \tag{12}$$

Clearly, the C_1 term gives the surface energy change in the (131) direction and is positive in the non-wetting and negative in the wetting cases, respectively. The C_2 term should always be positive and is associated with the InAs facets in contact with vapor.

The surface area of half the NW cross-section s equals the area of the parallelogram lh minus the area of the upper triangle Δs. The latter is given by $h^2/(8\sin\theta\cos\theta)$. Therefore,

$$s = lh - \frac{h^2}{8\sin\theta\cos\theta}, \tag{13}$$

where the second term is less than 10 % of the first one in our geometry and can be neglected in the first approximation.

To account for the effect of strain relaxation, we use the simplest formula [163–165]

$$\Delta G_{elastic} = \lambda \epsilon^2 V \frac{1}{1 + \alpha h/l}, \tag{14}$$

showing that the elastic energy (for the reduced strain ϵ due to dislocations) rapidly decreases ($\alpha \ll 1$) with increasing the aspect ratio h/l with respect to the 2D film of the same volume V. Using $V \approx 2dlh$ and dividing it by the facet length $2d$, we arrive at the equation expressing the free energy of forming the InAs NW of width l and height h on top of the GaAs NM

$$\Delta F(l, h) = C_1 l + C_2 h + \frac{C_3 lh}{1 + \alpha h/l}. \tag{15}$$

This free energy is defined per unit length of the structure. The C_1 term gives the surface energy change upon covering the GaAs (131) facets with InAs and is proportional to the NW width l. The C_2 term ($C_2 > 0$) stands for the surface energy of all other InAs facets and is proportional to the NW height h. The last term gives the elastic energy of the InAs NW, proportional to the NW cross-sectional area $s \approx lh$, with C_3 being the elastic energy per unit volume for the reduced mismatch [163], and α describing the stress relaxation with the aspect ratio h/l[163–165]. In fact, the NW cross-sectional area s equals $lh - \epsilon h^2$ due to the development of the horizontal (111) InAs top facet seen in Fig.21 of the main text, but the ϵh^2 term is typically less than 10 % and we omit it to simplify the analysis. We also assume that the term associated with the dislocation energy is roughly the same for any aspect ratio, which should be valid for large enough volumes of deposited InAs, with the NW heights already well above the critical thickness for forming misfit dislocations ($\sim 1.2\,\mathrm{nm}$) [164].

To access the preferred shape of InAs on top of GaAs, we minimize equation (14) at a fixed $s = lh$, corresponding to a fixed volume of deposited InAs [166]. Introducing $f = \Delta F/b$, the result is given by

$$\frac{df}{dh} = 1 - \frac{A}{x} - \frac{vs^{1/2}}{(1 + \alpha x)^2}, \tag{16}$$

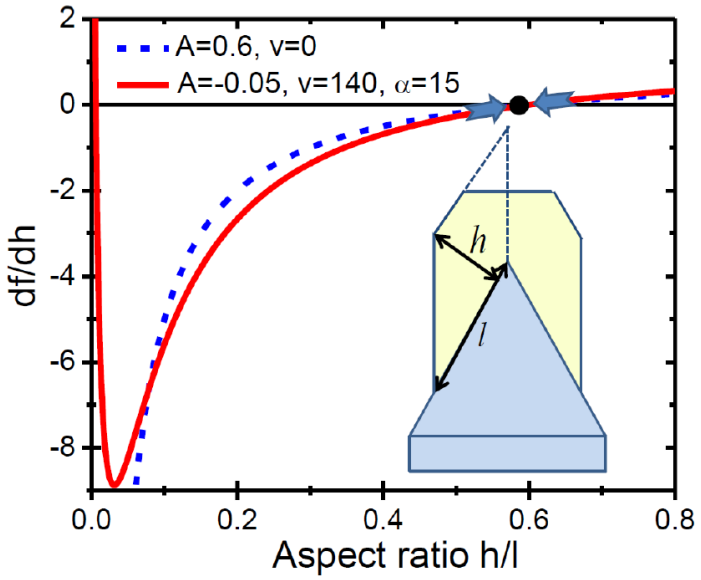

Figure 29: **Change in free energy of formation with aspect ratio** Graphs of the df/dh versus aspect ratio obtained in the non-wetting ($A > 0$) and wetting ($A < 0$) cases from equation (9). The zero point at $h/l \approx 0.6$ corresponds to the minimum free energy of forming the NW, because its derivative is negative for smaller and positive for larger aspect ratios. The real curve is expected to be the one in the wetting case, where the system surpasses an energetic barrier at a small x as in the Stranski-Krastanow growth. The value of $v = 140$ corresponds to the parameters of InAs with the reduced mismatch $\epsilon = 0.03$. The inset shows the geometry, the approximation $s \approx lh$ used in the calculations neglects the truncation of the full parallelogram in the top part of the NW.

with $A = C_1/C_2$ as the normalized surface energy change in the (131) plane, $v = 2\alpha C_3 s^{1/2}/b$ as the strain-induced factor that increases with the amount of deposited InAs, and $x = l/h$ as the aspect ratio of the NW. The preferred aspect ratio is now defined by the stable zero point of df/dh, corresponding to the minimum free energy.

Figure 29 shows two possible cases with the preferred $x \approx 0.6$, as observed in Fig.21 in the main text. We believe, however, that our GaAs/InAs system is initially wetting, that is, the surface energy favors 2D growth of InAs on GaAs, while 3D structures emerge only after the formation of a continuous wetting layer, as in the Stranski-Krastanow growth [165]. Therefore, the system is described by the solid line in Fig.29. In this case, reaching a high aspect ratio on the order of 0.6, which is necessary to form the NWs on top of the NMs, can only be due to strain relaxation and requires a high value of the strain-induced v factor of about 140. The c coefficient equals $\lambda\epsilon^2$, with $\lambda = 1.22 \times 10^{11}$ J/m^3 as the elastic modulus of InAs and ϵ as the reduced lattice mismatch. With the experimentally $\epsilon = 0.03$, this yields $v = 140$ at $\alpha = 15$ for a

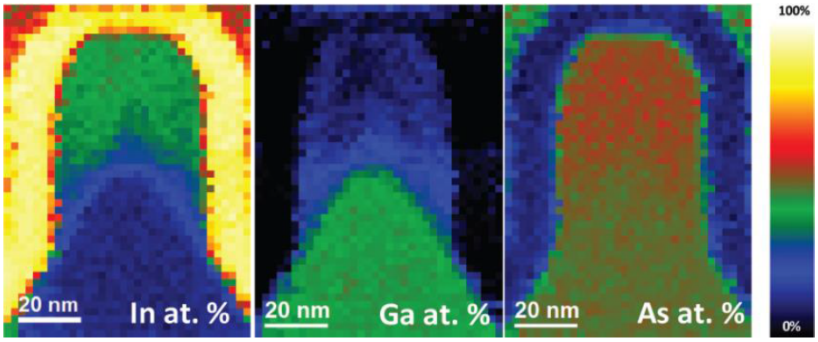

Figure 30: **Detailed compositional maps** Compositional map of InAs NM on GaAs NM for In, Ga, and As separately.

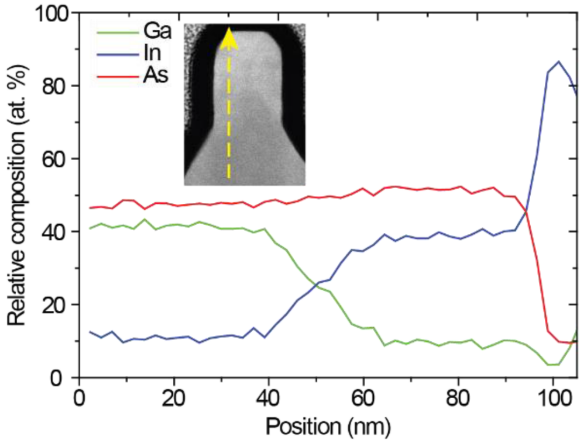

Figure 31: **EELS line scans** Compositional line scan from the GaAs NM into the InAs NW, showing relative concentrations of Ga, In, and As.

plausible value of $C_2 = 0.091$ J/m^2 [164].

3.6.7 TEM Compositional Line Scan

Looking at the EELS maps in more detail, a compositional map and line scan are shown in the Fig.30 and Fig.31, respectively.

From the line scan, we first notice that the amount of indium in the GaAs region and gallium in the InAs region never goes below ~10 %. This is suspicious and is likely an artifact of the EELS measurement, possibly caused by indium/gallium adatom migration induced by the 200 keV electron beam. An additional contributor to the indium signal could be the titanium in the TiO_2 capping layer. The two elements are difficult to differentiate, as the titanium $L_{2,3}$ edges overlap with the indium $M_{4,5}$ edges.

The scan also shows a region between about 40 nm and 60 nm where gallium is present in the InAs NW. APT measurements have ruled out Ga cation diffusion during the FIB preparation process. Due to the 100 ° difference in growth temperature between the GaAs and InAs and the necessary cool-down period between the two growths, we do not expect any free gallium adatoms on the surface to contribute to the formation of this InGaAs region. Rather, it is likely that stress drives diffusion of some gallium atoms from the NM into the InAs NW during NW growth to accomodate the high lattice mismatch. This observation suggests such strain might be used to overcome the miscibility gap that is present in unstrained $In_xGa_{(1-x)}As$ below about 800 K [167, 168].

3.6.8 InAs Crystal Quality

The crystal quality of the InAs NWs were further assessed by TEM imaging from the side of a GaAs/InAs NM/NW structure. Figure 32a provides an example atomic resolution ADF-STEM analysis from a roughly 70×70 nm^2 region near the base of the InAs NW. Geometrical phase analysis (GPA) of (-1-1-1) dilatation (see Fig.32b) reveals the presence of a double twin that appears to originate at the InAs/GaAs interface and propagates through the InAs layer.

The GPA structural map of the (-1-11) planes in Fig32c allows us to identify misfit dislocations, highlighted in red. Figure 32d applies a rotation filter that further highlights these misfit dislocations. The appearance of misfit dislocations in the axial direction, along the NW, is expected because the strain can not be as easily relaxed compared with the radial case. This is believed to be the reason that no misfit dislocations were observed in the transversal atomic resolution ADF-STEM cross sections. On the other hand, in the longitudinal cross-section, one can count seven misfit dislocations in this roughly 70 nm-long region. Using this value as an initial guess, we estimate that this structure has on the order of 100 misfit dislocations per micrometer.

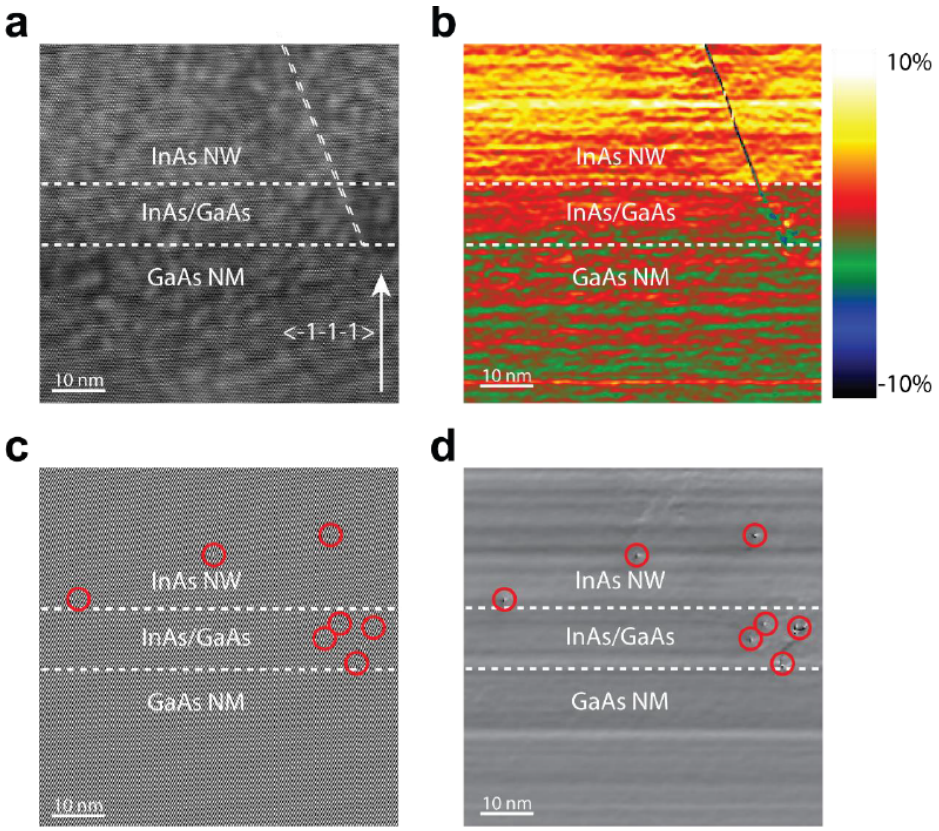

Figure 32: **TEM defect analysis (a)** Atomic resolution ADF-STEM image taken from a <0-11> zone axis at the base of the InAs NW on a GaAs NM showing two twins originating at the heterojunction and propagating into the InAs NW. **(b)** GPA analysis of image in **(a)** looking at dilation of (-1-1-1) planes. Here, the twin is clearly visible and the color contrast enables us to distinguish the InAs from the GaAs region. **(c)** Structural map of (-1-11) planes in image **(a)** allowing us to see the presence of misfit dislocations, highlighted in red. **(d)** Rotation filter of (-1-11) planes from image **(a)**, allowing us to more accurately distinguish misfit dislocations.

3.6.9 Magnetotransport Model

The conductivity dependence on magnetic field was fit with the following weak localization model for the quantum correction to the classical conductivity in the quasi 1D diffusive limit [169–171]

$$\Delta G = -\frac{2e^2}{hL}\left(\frac{1}{l_\phi^2}+\frac{1}{l_B^2}\right)^{-1/2}, \tag{17}$$

where L is the length of the wire between contacts, l_ϕ the phase coherence length, and l_B the magnetic dephasing length. l_B relates to the magnetic relaxation time τ_B as

$$l_B = \sqrt{D\tau_B}, \tag{18}$$

with $D = v_F l_e$ for 1D wires. In our system, in the diffusive limit where $l_e \ll W$, with W the conducting channel width, and $W \ll l_\phi$ (quasi-1D transport), τ_B is given as [170, 172–174]

$$\tau_B = \frac{3l_m^4}{W^2 D}, \tag{19}$$

where $l_m = \sqrt{\hbar/eB}$. This regime constrains l_e to maximally a few nanometers, which is in good agreement with the expected spacing between dopants. We estimate from a 3D doping concentration of 10^{27} per cubic meter a 1D concentration of 10^9 per meter, thus roughly one dopant per nanometer. The fits for the data yielded the values shown in the following table for l_ϕ in this limit.

Bias [mV]	l_ϕ [nm]	± [nm]
0	134	4
5	97	2
10	84	2
15	73	2
20	66	2

The accuracy of the fits for l_ϕ in this diffusive limit need to be taken with a degree of caution. When spin-orbit length, l_{so}, and mean free path, l_e, are included into the formalism, one has [169]

$$\Delta G = -\frac{e^2}{hL}\left[3\left(\frac{1}{l_\phi^2}+\frac{4}{3l_{so}^2}+\frac{1}{l_B^2}\right)^{-1/2}-\left(\frac{1}{l_\phi^2}+\frac{1}{l_B^2}\right)^{-1/2}-3\left(\frac{1}{l_\phi^2}+\frac{4}{3l_{so}^2}+\frac{1}{l_e^2}+\frac{1}{l_B^2}\right)^{-1/2}+\left(\frac{1}{l_\phi^2}+\frac{1}{l_e^2}+\frac{1}{l_B^2}\right)^{-1/2}\right]. \tag{20}$$

The data was fit for a range of values for l_{so}, which result in slightly varying l_ϕ between 130 and 160 nm, that fall off quickly with addition of voltage bias. When $l_{so} \to$ inf, the diffusive limit is recovered, as expected. The spin-orbit strength extracted from these fits is somewhat weak, corresponding to larger spin-orbit lengths than otherwise known from InAs [175, 176]. This is likely due to a combination of the gallium content in the wires and motional narrowing in the diffusive limit, with a mean free path on the order of nanometers. The complete lack of weak-antilocalization in the data is consistent with very weak spin-orbit interaction, thus, a large l_{so}. A 2D conductance map is shown in Fig.33, which shows the dependence of conductivity on both magnetic field and applied DC bias.

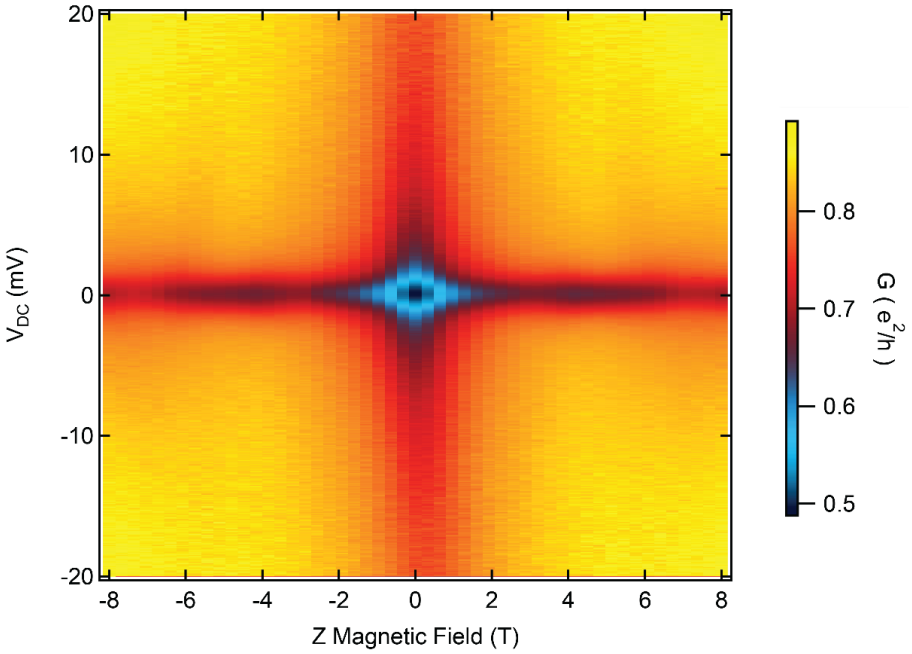

Figure 33: **Conductivity map as a function of magnetic field and bias voltage** Color scaling is differential conductance in units of e^2/h. The decrease in conductance around zero magnetic field is clearly manifested.

3.6.10 Atom probe tomography mass spectra

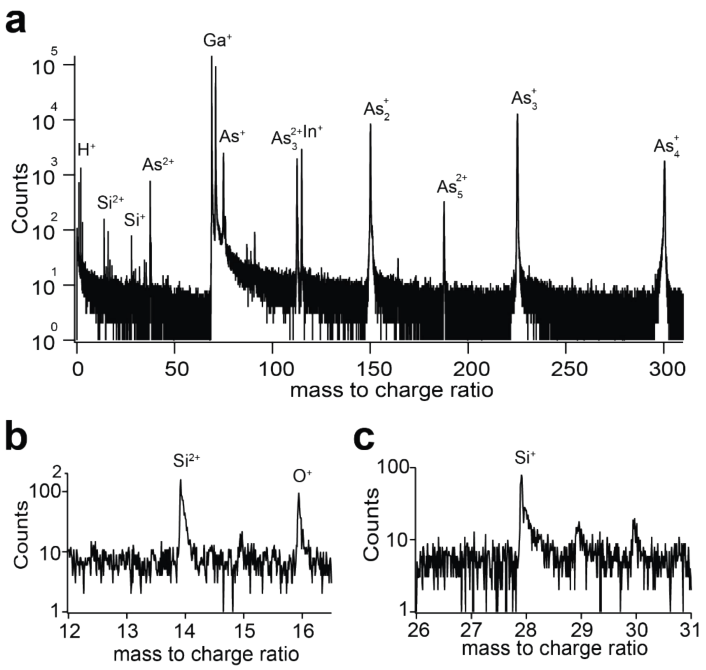

Figure 34: **APT mass spectra.** (a) Mass spectrum of InAs NW on GaAs NM for the atom probe tomography reconstruction shown in Figure 2g and Figure 2h in the main text. The acquisition conditions are described in the Methods section of the main text. (b), (c) Regions from the spectrum in a showing $^{14}Si^{2+}$ and $^{28}Si^{+}$ peaks, respectively. Peaks at m/q = 14, 14.5, 29 and 30, which include counts from Si isotopes, were not included in the reconstruction shown in Fig.21h due to overlap with other unidentified species.

4 Sub-gap bound-states in normal metal-insulator-superconductor junctions

M. Palma[1], L. Casparis[1,2], C. P. Scheller[1], T. Patlatiuk[1], L. Chirolli[3], D. Maradan[4], A. V. Feshchenko[5], M. Meschke[5], J. P. Pekola[5] and D. M. Zumbühl[1]

[1] *Department of Physics, University of Basel, CH-4056 Basel, Switzerland*

[2] *Center for Quantum Devices, Niels Bohr Institute, University of Copenhagen, 2100 Copenhagen, Denmark*

[3] *IMDEA-Nanoscience, Calle de Faraday 9, E-28049 Madrid, Spain*

[4] *Physikalisch-Technische Bundesanstalt (PTB), Bundesallee 100, 38116 Braunschweig, Germany*

[5] *Low Temperature Laboratory, Aalto University, FI-00076 Aalto, Finland*

This chapter is prepared for publication.

4.1 Abstract

We present the investigation of current steps appearing in the subgap region of the I-V characteristic of a NIS junction. The steps are manifestation of Andreev bound states enhanced by the disorder and geometry of the junction. Some of the steps show thermal broadening from 100 mK down to 4 mK, serving as primary thermometry. Numerical calculation captures the steps and the subgap conductance, which dependence on the disorder and on the geometry. Magnetic field characterization shows further a minigap, which decreases in magnetic field.

4.2 Introduction

Aluminum oxide tunnel junctions are basic building blocks for Josephson junctions, superconducting qubits [177] and many other applications including thermometry [99, 178, 179] and on-chip refrigeration [179–181]. A figure of merit for the quality of superconducting tunnel junctions is the Dynes paramter $\gamma = R_N/R_G$, defined as the ratio of normal state resistance R_N to the resistance in the superconducting state R_G. Ideally, the single particle current is fully suppressed within the superconducting gap. However, defects within the junction and the adjacent metal leads drastically reduce their quality and lead to decoherence in superconducting qubits [182–187]. Furthermore, external sources such as elevated sample electron temperature as well as remanent electromagnetic radiation, giving rise to photon assisted tunneling (PAT) [188], lead to single particle processes (quasiparticle poisoning) - fatal for both superconducting qubits and majorana experiments [189–193].

In this Letter, we investigate hard gap normal metal-insulator-superconductor (NIS) tunnel junctions at low temperatures [9, 100, 101], measured in heavily filtered and shielded dilution refrigerators where PAT is negligible. In addition to a small linear leakage current, we observe sharp current steps of small amplitude in the subgap regime, which can be used as a primary thermometer, in excellent agreement with regular NIS

thermometry [99], but cooling as low as 4 mK on a nuclear refrigerator [101]. In an in-plane magnetic field, the steps exhibit Zeeman splitting with a g-factor of 2 and display a parabolic magnetic field evolution consistent with a diamagnetic shift. The current steps appear at random energies (bias voltage) that varies upon thermal cycling of the device, in contrast to Shapiro steps in superconductor - insulator - superconductor (SIS) junctions that follow a well defined sequence, suggesting a prominent role of the sample specific disorder configuration.

We can model the steps as geometric resonances within the weakly disordered normal metal giving enhanced Andreev reflection due to multiple reflections at the otherwise rather opaque NIS interface. The model shows that disorder is a possible microscopic origin for Dynes-type linear leakage current in a regime where PAT is negligible.

The devices under investigation consist of two rectangular 40 nm thick Aluminum slabs with triangular tip pointing towards each other; see Fig.35a. After in-situ thermal oxidation, the sample is overgrown with a 20 nm, 50 nm, or 150 nm thick Cu layer of the same geometry but under different tilt angle (shadow mask evaporation [99, 194]) leading to the formation of a central resistive tunnel junction of area 380x400 nm^2, see inset of Fig.35a. Roughly half of the samples studied here are additionally equipped with a 50 nm thick gold ground-plane to shunt high frequency noise, which is separated by a 100 nm AlO_x barrier [188] from the rest of the device as shown in the sample schematic of Fig.35b.

The experiments are performed in two different dilution refrigerators with base temperatures of about 9 mK and 5 mK, respectively. The former refrigerator is equipped with a parallel network of nuclear refrigerators (NRs), which employs magnetic cooling to reach roughly $T_{\mathrm{Cu}} \sim 1$ mK in the Cu nuclear refrigerant. The cooling scheme relies on the standard adiabatic nuclear demagnetization technique, which was adapted for direct cooling of nanostructures [96, 97, 100]. The performance of the Cu NRs was extensively studied in previous works [96, 97, 100], giving a very good estimate of the electronic temperature of the NRs after each demagnetization for a given final B-field.

The latter dilution refrigerator, on the other hand, is equipped with a vector magnet thus allowing for in-plane magnetic field $B_{||}$ measurements with compensated out of plane magnetic field $B_{\perp}$.

Fig.35c shows typical current-voltage traces for device NIS_1, measured at various refrigerator temperatures T_{Cu} and zero magnetic field. All devices under investigation display a hard gap behavior, shown in the inset of Fig.35c for NIS_1. Zooming into the subgap regime (main panel) reveals a linear background current that exceeds the theoretical predictions for coherent Andreev processes in resistive NIS tunnel junctions by roughly two orders of magnitude [195]. In addition, small current steps are observed that are located symmetrically around zero bias thus reflecting the electron-hole symmetry in the superconductor. We note that similar current steps are seen for all 8 devices investigated here. The current steps are strongly temperature dependent and smear out at elevated T_{Cu}, in contrast to the linear, Dynes type leakage current that remains unaffected within the studied temperature regime.

In order to quantitatively analyze the measurements we fit the sum of two Fermi functions (symmetric with respect to mid-gap) on top of a linear slope to the data and find that step position and amplitude, as well as the Dynes parameter γ, are not temperature dependent. Therefore those parameters are held fixed for further analysis, leaving the broadening δV of the Fermi function as the only fit parameter. Since the resistance in the subgap regime is much larger than any series resistance arising from the leads, the full applied voltage drops across the tunnel junction. Thus δV is converted directly to an electronic temperature T_{step} using $|e|\delta V = k_B T_{\mathrm{step}}$, where e is the elementary charge and k_B the Boltzmann constant. Indeed, the extracted T_{step} agrees well with T_{Cu} in the temperature range between 9 mK and 100 mK, see red squares in Fig.35d. Since no calibration is needed, the subgap steps can serve as a primary thermometer.

In order to verify the correct temperature reading of T_{step}, we compare it to another primary on-chip thermometer: Close to the superconducting gap the current

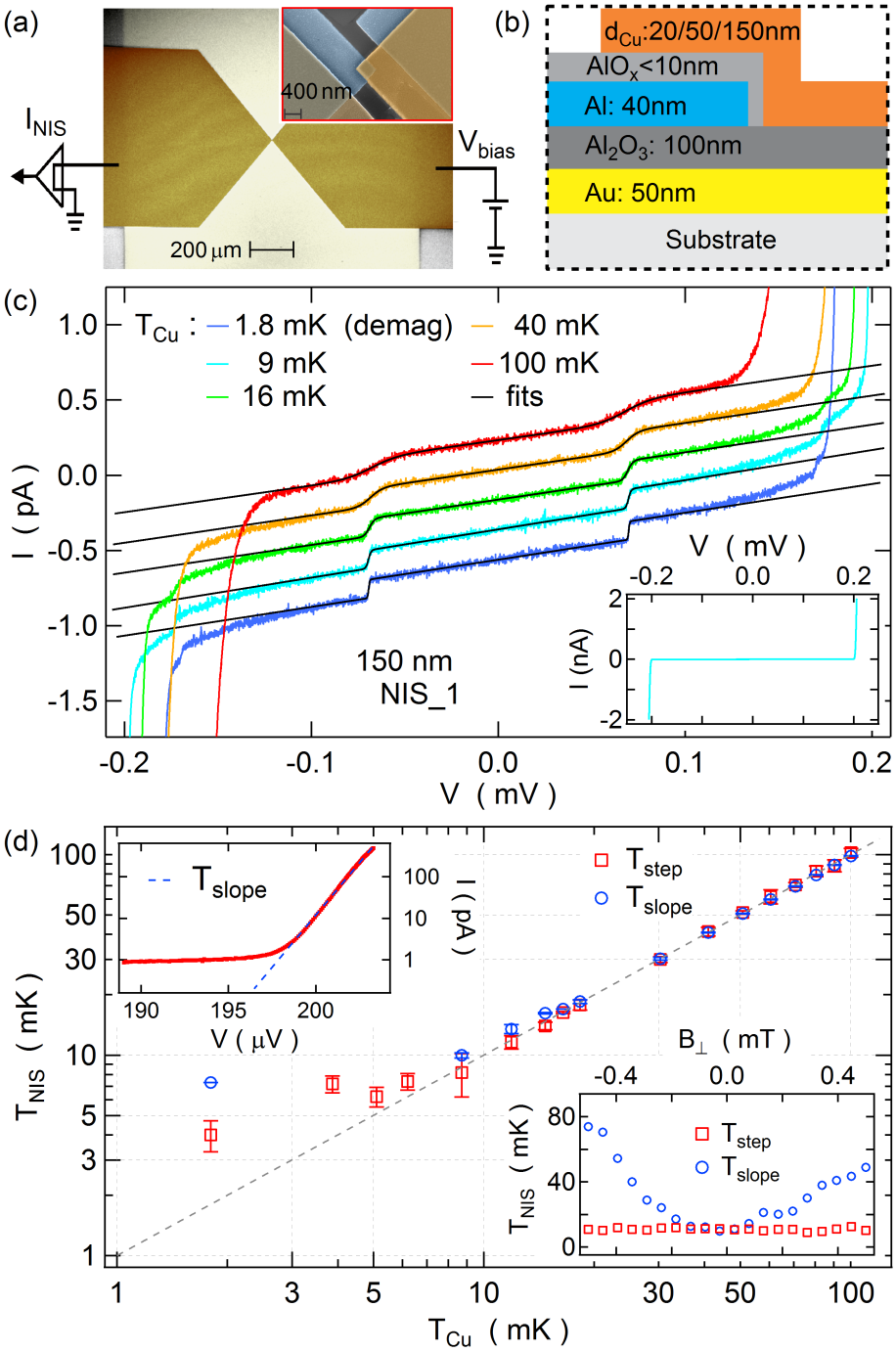

Figure 35: (a) Scanning electron micrograph of a co-fabricated NIS device together with a schematic of the experimental setup. The inset shows a zoom-in of the tunnel junction. (b) Schematic cross section of the NIS junction. (c) Zooms of the I-V curves in the subgap region for various temperatures. Traces are offset vertically for clarity. The black line indicates the double Fermi function fits used to extract T_{step}. To reduce the error on T_{step} the fit is performed on 10 consecutive I-V curves taken at the same temperature and we use the mean value as $< T_{\mathrm{step}} >$ and its standard deviation as error bar. The I-V characteristic for large current range is shown in the lower inset of Fig.35c. (d) T_{step} and T_{slope} as a function of T_{Cu}. The upper inset shows the region of the I-V curve where the semi-logarithmic fit is applied. The lower inset shows T_{step} and T_{slope} as a function of perpendicular magnetic field.

I rises exponentially with applied voltage V and inverse temperature $1/T_{\mathrm{slope}}$, $I \sim \exp(eV/k_B T_{\mathrm{slope}})$ [99, 196], thus allowing us to extract temperature from a linear fit to $\log(I)$ [99], see upper inset of Fig.35d. Indeed, T_{slope} agrees well with T_{step} above 9 mK. After adiabatic nuclear demagnetizing of the leads (the NIS device itself resides within a B-field compensated region) the Cu refrigerant cools down to T_{Cu} ∼1 mK, T_{slope} saturates at 7.5 mK and T_{step} reaches 4.0±0.7 mK, see Supplementary Material. This constitutes the lowest reported electronic temperature for a NIS tunnel junction [99, 178] and is close to lowest temperature obtained so far in a nanoelectronic device [100, 197].

We note that T_{slope} is extremely susceptible to perpendicular magnetic fields $B_\perp$, even on the scale of 1 G. As shown in the lower inset of Fig.35d in presence of a small $B_\perp$ this already results in vastly overestimated electron temperatures. In contrast, T_{step} remains unaffected, showing that T_{step} is more robust against $B_\perp$. On the other hand, while the steps in Fig.35c exhibit a temperature dependence down to 4 mK due to their weak coupling to the leads other subgap steps in different devices saturated at significantly higher temperature (not shown).

The zero bias step (ZBS) exhibits a temperature dependence, however the temperature extracted by fitting to ZBS a Fermi function is systematically higher than T_{Cu} up to 150 mK. The deviation between the two temperatures is reduced for higher T_{Cu} and they agree for temperatures above 150 mK. In addition, the ZBSs are independent from the thermal cycling while the position of finite bias steps (FBSs) randomly change for each thermal cycle, giving evidences that the impurities might be the origin of the steps.

In order to shed more light on the origin of the steps, we study their behavior upon thermal cycling. For each cycle the samples are cooled from room temperature down to base temperature of the cryostat. We observe a random movement of the energy positions for various cycles. Fig.36a shows the I-V curves of the device NIS_2 for four different cycles, which are indicated by shades of grey. This particular device features

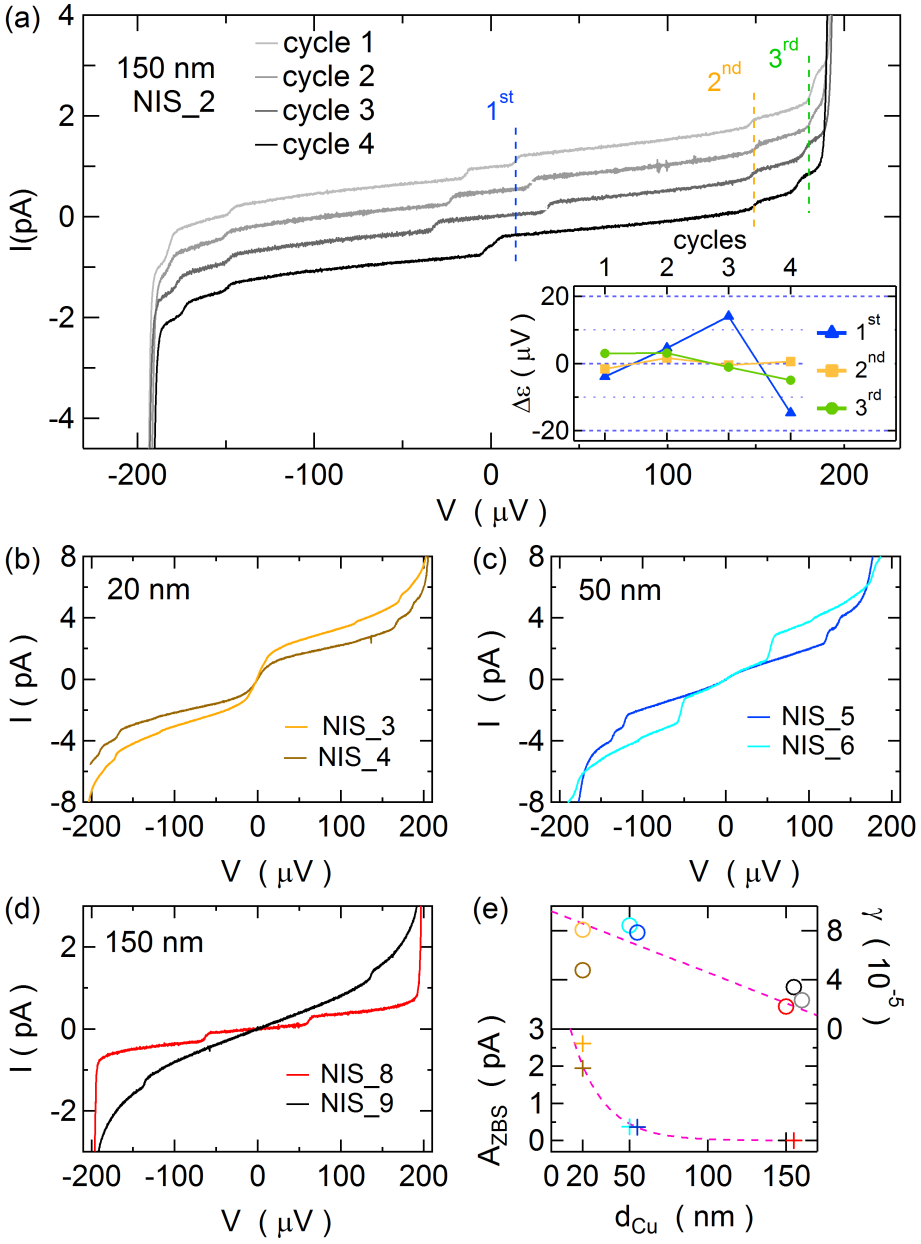

Figure 36: (a) I-V curves of the NIS_2 for various thermal cycles. (b-d) I-V curves for two different devices at Cu thickness of 20 nm, 50 nm and 150 nm, respectively. (e) the upper graph shows the Dynes parameter as a function of d_{Cu} and the lower graph shows the amplitude of the ZBS as a function of Cu thickness. Note that for both graphs the points at 50 nm and 150 nm are horizontally offset by 5 nm to avoid the overlap of the markers.

three separated discrete steps, two of them barely move upon thermal cycling, while the lowest energy one changes significantly, see inset of Fig.36a.

Next, we characterize the steps as a function of the Copper layer thickness (d_{Cu}) in order to gain more insight about their origin. In this study device with Cu thickness of 20 nm, 50 nm and 150 nm were measured. The steps, appearing at random bias voltages, were observed in all investigated junctions. Corresponding I-V curves are shown in Fig.36b-d. The amplitudes of these steps are not correlated with d_{Cu} and vary over one order of magnitude ranging from few hundreds fA up to several pA. The I-V curves for the device with $d_{\mathrm{Cu}} = 20\,\mathrm{nm}$, exhibiting strong ZBS and weak FBSs close to the superconducting gap edges, are shown in Fig.36b. ZBS is faintly visible (Fig.36c) and completely absent (Fig.36d) in the devices wit $d_{\mathrm{Cu}} = 50\,\mathrm{nm}$ and $d_{\mathrm{Cu}} = 150\,\mathrm{nm}$, respectively. The amplitude of the ZBS as a function of d_{Cu} is shown in the lower panel of Fig.36.(e).

The upper inset on the Fig.36e shows that the Dynes parameter γ decreases as d_{Cu} is increased. It is important to mention, that γ is the same for the devices with (NIS_5) and without (NIS_6) the back-plane. Corresponding I-V curves are shown in Fig.36c. This is in contrast to the previous experiment [188] and suggest that heavy RF filtering and shielding present in our setup strongly suppresses photon-assisted tunneling.

In the last experimental section of this letter, we investigate the magnetic field dependence of both, ZBS and FBSs. The measurements were performed in a cryostat equipped with a two-axis vector magnet with one component oriented in the plane ($\mathrm{B}_{\parallel}$) and another component oriented perpendicular ($\mathrm{B}_{\perp}$) to the plane of the junction. Figures 37a-d show the logarithm of the differential conductance G as a function of the voltage bias and $\mathrm{B}_{\parallel}$ for devices with different copper layer thicknesses. To compensate a small sample misalignment the magnetic field $\mathrm{B}_{\perp}$ was varied for each value of $\mathrm{B}_{\parallel}$ such as to maximize the superconducting gap and cancel out the out of plane component of the magnetic field.

As magnitude field $B_{\parallel}$ was increased, the strength of the ZBS gradually decreased and disappeared for $\left|B_{\parallel}\right| > 130\,\mathrm{mT}$. At the same time, the superconducting gap closes only

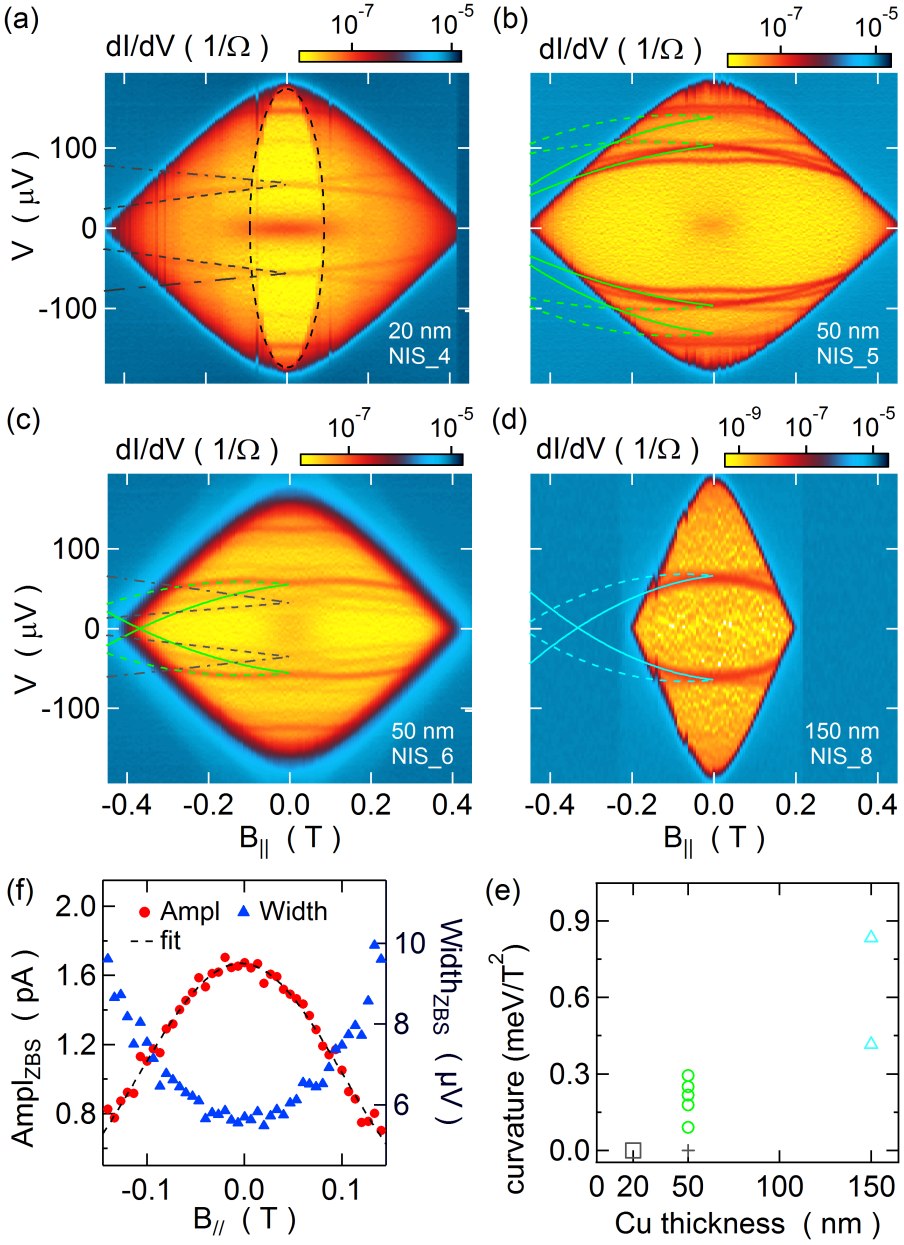

Figure 37: (a-d) The differential conductance plotted in logarithmic color scale as a function of the in-plane magnetic field and the bias voltage for the devices with various Cu thicknesses. The solid lines in (b-d) indicate the parabolic evolution of the FBSs as a function of $B_{\|}$. The dashed lines are displaced from the solid lines by Zeeman energy. (f) The amplitude and the width of the ZBS as a function of in-plane magnetic field. The Gaussian fit to the $\mathrm{Ampl_{ZBS}}$ is shown as a black dashed curve. (e) Curvature $e^2\lambda^2/m$ plotted as a function of Cu layer thickness.

around $B_{\|} = 500\,\mathrm{mT}$. Figure 37f shows how amplitude and width of ZBS depend on magnetic field $B_{\|}$. For the devices with $d_{\mathrm{Cu}} = 50\,\mathrm{nm}$ the ZBS was suppressed already at 60 mT, see Fig.37b,c. FBSs show more complicated dependence on $B_{\|}$ that will be discussed in the next section.

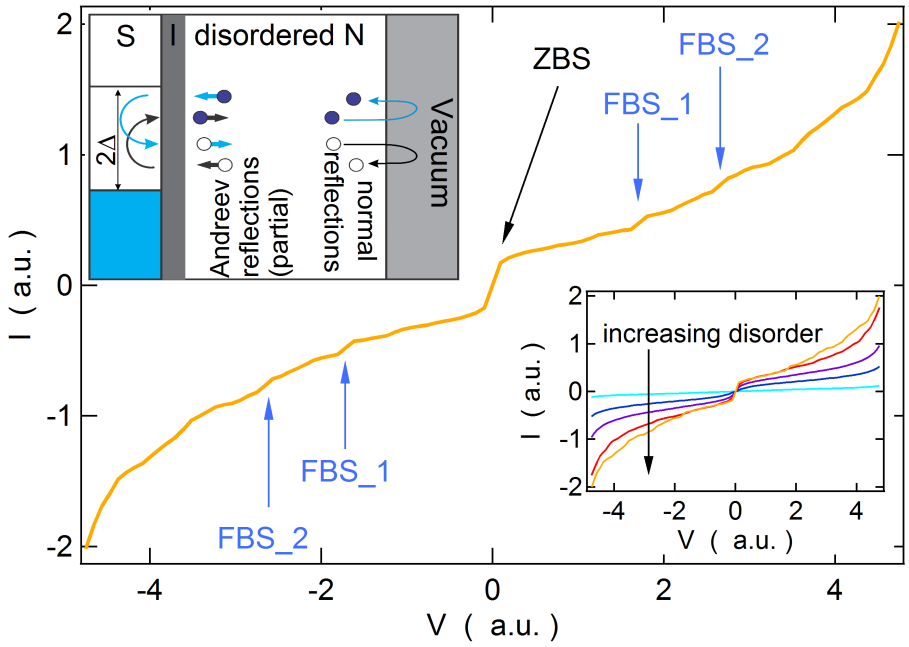

Figure 38: (a) Simulated I-V curve. The upper inset shows Energy diagram of the NIS junction. Showing Andreev reflections (light blue arrows) at NIS interface and normal reflections (black arrow) at the normal metal - vacuum interface. The lower inset shows simulated I-V curve for different disorder strengths.

Vortices pined by the impurities in the superconductor, which support core bound stats [198], can be the possible origin of the FBSs. An argument against this hypothesis is that FBSs are visible in the whole range of $B_{\|}$-fields, even for the fields smaller than the threshold to create a single vortex, see Fig.37. This exclude the vortex bound states as a possible origin of the FBSs. Further more, FBSs are insensitive to the flux jumps induced by $B_{\perp}$ as long as the superconducting gap is not closed.

We now turn to a model of the device. Motivated by FBS energy changes upon thermal cycling as well as random sample-to-sample variations, we develop a tight binding model of the junction based on a disordered normal metal layer of finite thickness sandwiched between a tunnel coupled superconductor and a vacuum interface, see upper inset in Fig.38. The rather low transparency of the barrier to the superconductor implies that an Andreev reflection occurs only rarely e.g. after numerous attempts. The details of the model are presented in the Supplementary Material section S2.

Figure 38 shows the simulated I-V curves for a rather strong disorder with clearly

visible FBSs. Due to computational complexity, the model is limited to a relatively small number of lattice sites. In order to mimic a large device, each I-V curve was averaged over 100 disorder configurations. The features that survive the averaging are predominantly related to the junction geometry. The lower inset in Fig.38 shows the simulated I-V curves for different strengths of disorder. FBSs and ZBS are present on the traces with strong disorders.

The interplay between disorder and the geometry of the tunnel junction produces many unresolvably small steps in the I-V curve, that upon disorder averaging result in a linear slope in the subgap region and thus provide a microscopic picture of the Dynes parameter in resistive tunnel junction, where extrinsic contributions such as photon assisted tunnelling are strongly suppressed. The numerical simulations also show that the subgap leakage current increases upon increasing the disorder strength.

In the following sections, we focus on the interpretation of the FBS and ZBS. The FBSs are given by geometrical resonances due to the charge carriers bouncing coherently in the normal metal layer, leading to the formation of bound states. Furthermore, a moderate-to-strong level of disorder is needed to amplify the geometrical resonances and make the observation of the FBSs possible.

In the presence of a B-field, electrons with different spin orientations are separated by Zeeman energy $g_e\mu_B B$, where $g_e = 2$ is the electron g-factor and μ_B is the Bohr magneton. In addition, electrons localized on a length scale λ experience diamagnetic shift in energy [199] $e^2B^2\lambda^2/m$, where e and m are charge and mass of the electron. These two effects: splitting and parabolic evolution of FBS are clearly visible in experiment Fig.37a-d. The solid and dashed lines correspond to two possible spin orientations. Figure 37e shows the extracted value of $e^2\lambda^2/m$, which result in $\lambda \approx d_{\mathrm{Cu}}$.

All studied junction have high normal state resistance, so probability for electron to undergo Andreev reflection is quite low. Small thickness of the normal metal layer makes it possible for electrons to hit the normal metal - insulator interface many times before loosing a phase-coherence. This increases the chance for electron to be transferred

into the superconductor after being Angreev reflected as a hole. Similar enhancement of Andreev reflection was theoretically predicted and experimentally observed in NIS junctions with disordered normal metal region [200, 201]. On the other hand, in the case of thick normal metal layer, electrons bounce fewer times before losing phase-coherence, so probability of Andreev reflections is not enhanced much. This behavior is in agreement with the experimental data. Figure 36e show that the amplitude of the ZBS decreases as the thickness of the normal metal layer d_{Cu} is increased. Additionally, phase coherence can be suppressed by increasing the temperature or by applying a B-field. Indeed, we observe that the amplitude of the ZBS stays constant up to ~ 100 mK and decreases for higher temperatures. Increasing the magnetic field also reduces the amplitude of the ZBSs as illustrated in Fig.37a-c.

The simulation also predict that the conductance measured as a function of bias voltage and magnetic field should display regions of different background conductance, which strongly resemble the "evil eye" of NIS_4 (Supplementary Material Fig.42). We interpret the evil eye as transport minigap [202–206] that opens in the junction area and can be closed by magnetic field. For the device with $d = 20$ nm the value of the minigap in a linear diffusive junction is of the order of Thouless energy $E_{\mathrm{Th}} = 300\mu eV$, which is larger than the SC transport gap. Numerical simulations of the smaller device confirm a diamond like structure of the background conductance as a function of the field, see Supplementary Material.

In conclusion, we observe current steps in the subgap region of the I-V characteristic associated with the formation of bound-states in the normal metal part of the NIS junction. In presence of magnetic field $B_{\|}$ FBSs show the normal metal thickness dependent damagnetic shift, consistent with the picture of localized-state in a magnetic field. The FBSs are thermally broadened down to 4 mK, so can be used as a primary thermometers. Observed ZBS is ascribed to Andreev reflection processes amplified around zero bias by disorders and sample geometry. Developed theoretical model shades light on the microscopic origin of the Dynes parameter. In this model the

linear subgap leakage current consist of many unresolvably small steps generated by disorders in the normal metal. Additionally, we show evidence for minigap formation in the junction of particular geometry, which can be suppressed by magnetic field.

4.3 Acknowledgments

We would like to thank F. Taddei, P. San-Jose, C. Bruder, S. Hoffman for useful input and discussions. The work shop team of S. Martin is acknowledged for technical support. This work was supported by the Swiss NSF, NCCR QSIT, the Swiss Nanoscience Institute, the Europeam Microkelvin Platform, an ERC starting grant (DMZ), and EU-FP7 MICROKELVIN and SOLID. L. C. acknowledges funds from the Comunidad de Madrid and the EU under the Grant: MAD2D-CM, S2013/MIT-3007, and the EU-FP7 ERC Advanced Grant NOVGRAPHENE Nr. 290846

4.4 Supplementary Information

4.4.1 Current Steps in Differential Conductance

In this section, we focus on the differential conductance G of the experimental traces, obtained by numerical differentiation of the measured I-V curves. The derivative of a step is a symmetric peak centered in voltage bias around the position (inflection point) of the step, see Fig. 39a-c. From now on, we refer in the text to peaks instead of current steps, since the supplementary material is presented in terms of differential conductance G.

Symmetric peaks are observed e.g. in Josephson junctions [196, 207], i.e. superconductor-insulator-superconductor junction, when microwave radiation is applied to the junction. Those are named Shapiro steps [208, 209] and are a direct consequence of the AC Josephson effect. We can exclude Shapiro steps as possible origin for the current steps, since they appear periodically at voltages $V_n = hf/2e$ while the peaks presented in this work are randomly distributed in voltage bias.

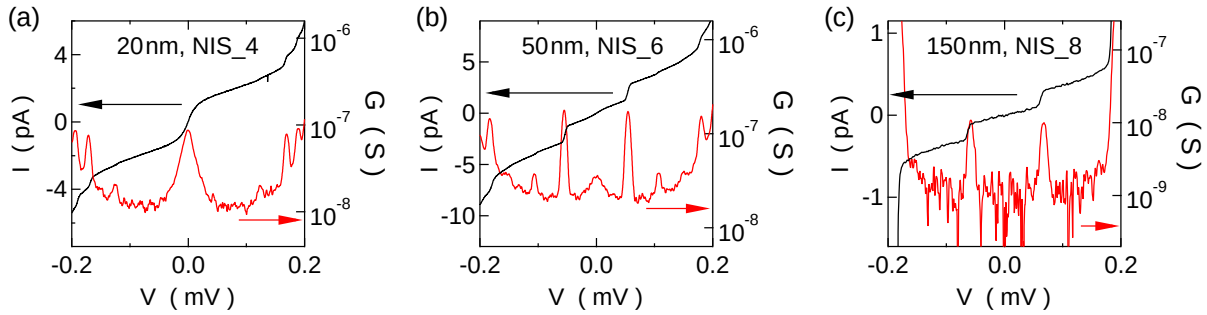

Figure 39: (a-c) I-V curves and the differential conductance G for NIS_4,NIS_6 and NIS_8. The steps observed in the I-V characteristic are transformed in symmetric peaks in the differential conductance.

4.4.2 Numerical Simulation

In the experiment we have three different junctions, characterized mainly by the thickness of the Cu layer. The geometry of the devices consists on a normal lead placed in proximity with a superconducting lead, in a way that on area of 400 nm the two leads overlap. The overlapping region constitutes the NIS junction. Although the experimental device is three-dimensional, we simulate the system by focusing on the two-dimensional section, as shown in Fig. 40. The system is composed by a central region that mimics the actual geometry of the NIS junction. Attached to the central there are a normal lead on the left side and a superconducting lead on the right side. Part of the central device is superconducting (red spots), to better model the NIS geometry. In every site of the central region there is an impurity, that is schematically represented by a white spot in Fig. 40.

The system is modeled by a tight-binding square lattice and impurities are inserted as a local on-site random energy shift of strength comprises between $-U$ and U. The simulations are performed with a Mathematica Package developed by Pablo San-Jose [1]

We start the analysis by first addressing the conductance of the device as a function of the strength of the disorder U. We simulate a device with thickness $W = 100$ sites, $L = 200$ sites and with leads of thickness of 100 sites. Fixing a hopping parameter $t_0 = 1$ eV, a Fermi energy on order of $E_F = 2.25$ eV, and assuming bare electron mass,

[1] P. San-Jose, http://www.icmm.csic.es/sanjose/MathQ/MathQ.html.

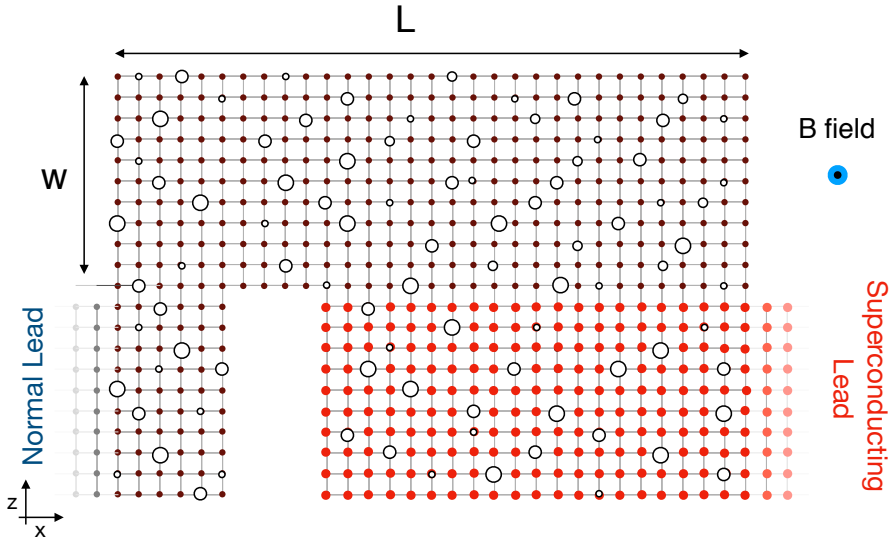

Figure 40: Devices simulated: The system is composed by a square lattice, on the left side we have the normal lead, that is represented by shaded spots that fade away from the device. Analogously, on the right side we have the superconducting lead, that is represented by red spots. The central region comprises also part of the superconducting lead. Impurities are modelled as a local shift of energy and are represented by some indicative white spot, whose size mimics the impurity strength.

the lattice parameter is on order of the Angstrom, so that we simulate a relatively thin device $d_{Cu} = 10\,\text{nm}$. We assume that the superconducting part in the central region (red in Fig. 40) is connected to the normal region by a hopping $t_1 = 0.015\ t_0$, so to simulate a resistive barrier, and we choose the superconducting gap to be $\Delta = 0.005\ t_0$.

In order to obtain a sample independent characterization of the device, we average over many disorder configurations, keeping fixed the strength of the disorder. This is a standard procedure that not only provides device-independent information of the system behavior, but it also better models a single device characterized by a disorder that changes on a scale of the device size.

In Fig. 41a we plot the conductance of the device, each curve corresponding to a different impurity potential strength $U/t_0 = 0,\ 0.3,\ 0.6,\ 0.9,\ 1.2$. We see that upon increasing the strength U the conductance starts to show a background finite value, that can be seen as composed of many resonances at all energies. The associated I-V characteristics is shown in Fig. 41b. We see that it acquires a finite slope due to the disorder induced background conductance. This behavior is contrary to the expectation

of a NS junction with an ordinary linear geometry. In that case, upon increasing the disorder the conductance decreases. Such behavior is due to coherent two-particle tunneling, which dominates in the tunneling limit considered and it is strongly affected by geometrically enhanced interference effects taking place on a length scale of roughly the coherence length. It is worth to point out that it is completely different from a finite DOS in the superconductor modeled by a Dynes parameter.

Beside the background finite value, every curve presents a zero bias conductance peak, that is due to reflectionless tunneling [200, 201]. At small energy Andreev reflection is perfect for a transparent barrier and the phase i determines full current through the junction, regardless of the disorder configuration. Upon reducing the transparency of the barrier the conductance is depressed at finite energy and survives at zero energy in the form of a peak. The width of the peak does not depend on the strength of the disorder, but the height of the peak increases with disorder. The particular geometry enhances the Andreev reflections due to the back wall of junction, that reflects particles and let them collide many time onto the superconductor, where they are occasionally Andreev reflected. Regardless of the low rate of Andreev reflection at each collision due to the low transparency of the barrier, coherent sum over many path makes the Andreev reflection at zero bias particularly efficient.

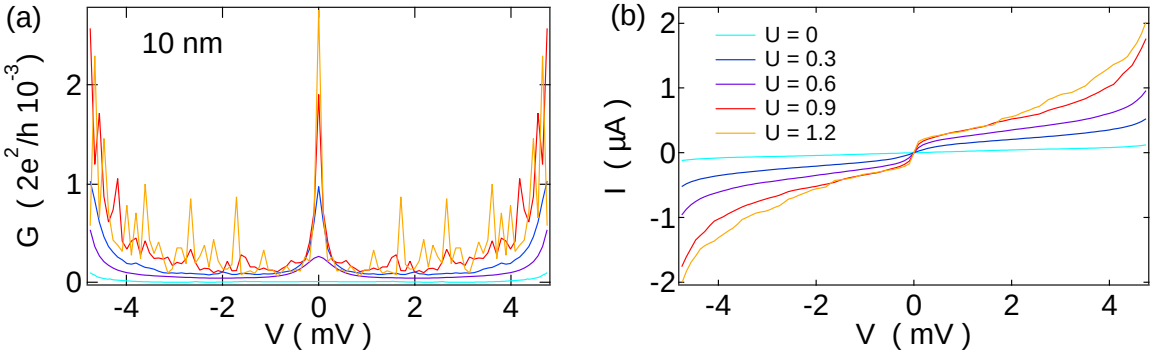

Figure 41: (a) Conductance as a function of the voltage bias and (b) I-V characteristics of a 10 nm thick NIS junction with the geometry of Fig. 40 for several values of the disorder strength $U/t_0 = 0.0, 0.3, 0.6, 0.9, 1.2$. and the conductance has been averaged over 100 configuration for each voltage V. The device has $W = 100$, $L = 200$, $t_0 = 1$ eV, $t_1 = 0.015\ t_0$, $\Delta = 0.005\ t_0$.

Finally, we notice that well defined conductance peaks at finite energies appear upon

increasing the disorder strength. Remarkably, the peaks survive disorder average. This is a very important result, stating that the origin of these resonances is related to the geometry of the system and it is strongly enhanced by disorder. Although every disorder realization presents a randomly distributed series of resonance, the averaged conductance makes manifest the underlying geometric origin of the resonances.

In the regime we are considering the bare coherence length of the superconductor is on the order of 200 lattice sites, that is on order of the linear sizes of the system, and interference effects in the two-particle coherent tunneling can be strongly enhanced by the geometry. The occurrence of a peak is consistent with a quasi-ballistic picture, in which the mean free path $\ell_{\text{m.f.}}$ is at on order of the length W. The latter can be estimated for a linear geometry by the Drude weight [200] $G_N = (2e^2/h)\pi N \ell_{\text{m.f.}}/2\tilde{L}$ and for about $N = 50$ number of propagating modes, taking as the linear size the geometric mean $\tilde{L} = \sqrt{LW}$ and calculating the average zero-energy conductance in the normal case with $t_1 = t_0$ and $U = 1.2\ t_0$ we find $\ell_{\text{m.f.}} \sim 5 - 10$ lattice sites, that is an order of magnitude smaller than W. In a linear geometry such a ratio between the mean-free path and W would imply a diffusive/quasi-ballistic regime. We then conclude that the geometry of the system enhances coherence effect and that the correct regime is quasi ballistic.

The back wall of the junction reflects particles towards the interface with the superconductor and a quasi bound state occurs, in which a particle bounces many times between the corners of the normal region and the superconductor, experiencing both normal and Andreev reflection. Weak disorder randomizes the momentum at every scattering event, so that it connects bound states that form in the junction to the scattering channels. For the strong disorder case the mechanism at the basis of finite energy peaks is similar to the reflectionless tunneling characterizing the zero bias peak. When normal reflection dominates, due to the low transparencies of the barrier, resonances occur also at finite energy thanks to the peculiar geometry. The energy of the resonance is inversely proportional to the path length of the bound state, that in

turn is upper bounded by the width W. However, disorder randomizes the motion and resonances can occur at any energy in the gap.

4.4.3 Magnetic Field Dependence

We now study the magnetic field dependence of the resonances. We assign a given disorder configuration with strength $U = 0.9\ t_0$ and we do not average over disorder. We assume $t_0 = 1$ eV, $\mu = -2.25$ eV, $t_1 = 0.015\ t_0$, and $\Delta = 0.005\ t_0$. We fix the sample size to $W = 200$ sites and $L = 400$ sites. In order to amplify the effect of the magnetic field we assume a lattice parameter $a \simeq 5$ Å and a large g-factor $g^*/g = m_0/m^* \simeq 27.6$. Although these number do not provide a good description of a metal, they allow us to study the putative effect of a magnetic field and to check the results with the experiment. The magnetic field is applied in the plane of the junction, that is orthogonal to the lattice in the simulation.

The resuts of the simulations are shown in Fig. 42a, where we show the conductance versus the applied field B and the energy ϵ, together with the $\log(G)$ in Fig. 42b and the $\log(G)$ after a cutoff for $G > 0.07$ is applied in Fig. 42c. The resulting Zeeman splitting for 0.5 T is on the order of 0.0008 eV, so that Figs. 42 are almost entirely dominated by orbital effect. Two features clearly appear: i) the resonances move with the magnetic field and their trajectories depart from the Zeeman induced linear splitting, ii) the background conductance changes as a function of the B-field and produces three different regions.

4.4.4 Resonances versus B-field

The resonances clearly acquire a dependence from the orbital magnetic field. The evolution is quite complicated but a common feature can be seen: the peaks position oscillates with the magnetic field. This pattern is visible for every resonance and the evolution is the result of several crossings of the different resonances. The oscillation and crossing may result in a diverging or a converging resonance as a function of the

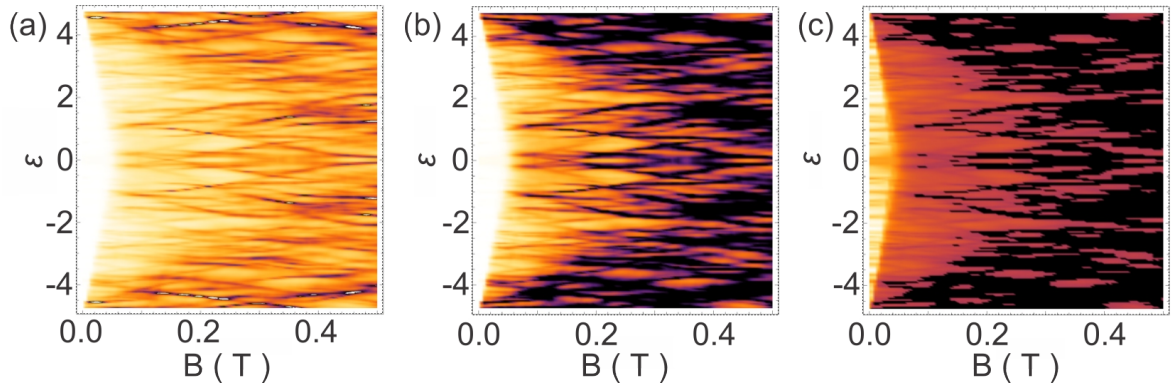

Figure 42: (a) Color plot of the conductance as a function of the magnetic field B (abscissa) and the energy ϵ (ordinata). (b) Color plot of $\log G$, and (c) color plot of $\log G$ with a cutoff for values $G > 0.07$. Parameters of the simulations are $t_0 = 1$ eV, $\mu = -2.25\ t_0$, $\Delta = 0.005\ t_0$, $t_1 = 0.015\ t_0$, $g^*/g = 27.6$, $a \simeq 5$ Å.

applied field. For small B the resonances show a very tiny dependence on the applied field, as it is visible in Fig. 42c. In order to further understand the dependence on the magnetic field we simulate a much smaller device with a slightly different geometry (see Fig. 43c). We see that the finite-bias peak for the case $U = 0.8\ t_0$ bend towards zero energy (Fig. 43b). The values of the magnetic field are very high, whereby $2\pi\Phi/\Phi_0 = ea^2B/\hbar$ is the Peierls phase associated to the orbital magnetic field.

In Fig. 43d-e we also plot the scattering states of two given transport channel in the cases $U = 0$ and $U = 0.8\ t_0$, both for the ZBP and the FBP. The clean case shows how bound states develop in the junction region, confirming the geometric origin of the resonances. In the disordered case we see that the motion becomes highly irregular, but the comparison between the ZBP and the FBP confirms the common origin of the effect.

4.4.5 Background Conductance and Minigap

The background conductance as a function of the energy and the magnetic field shows two regions of different background value: very bright, bright, and slightly dark in Figs. 42. The first region is approximately comprised in the region $|\epsilon|/\Delta < 1 - \epsilon|B|/B_1^*$, with $B_1^* \sim 0.07$ T, and the second region approximately comprised in the region $|\epsilon|/\Delta <$

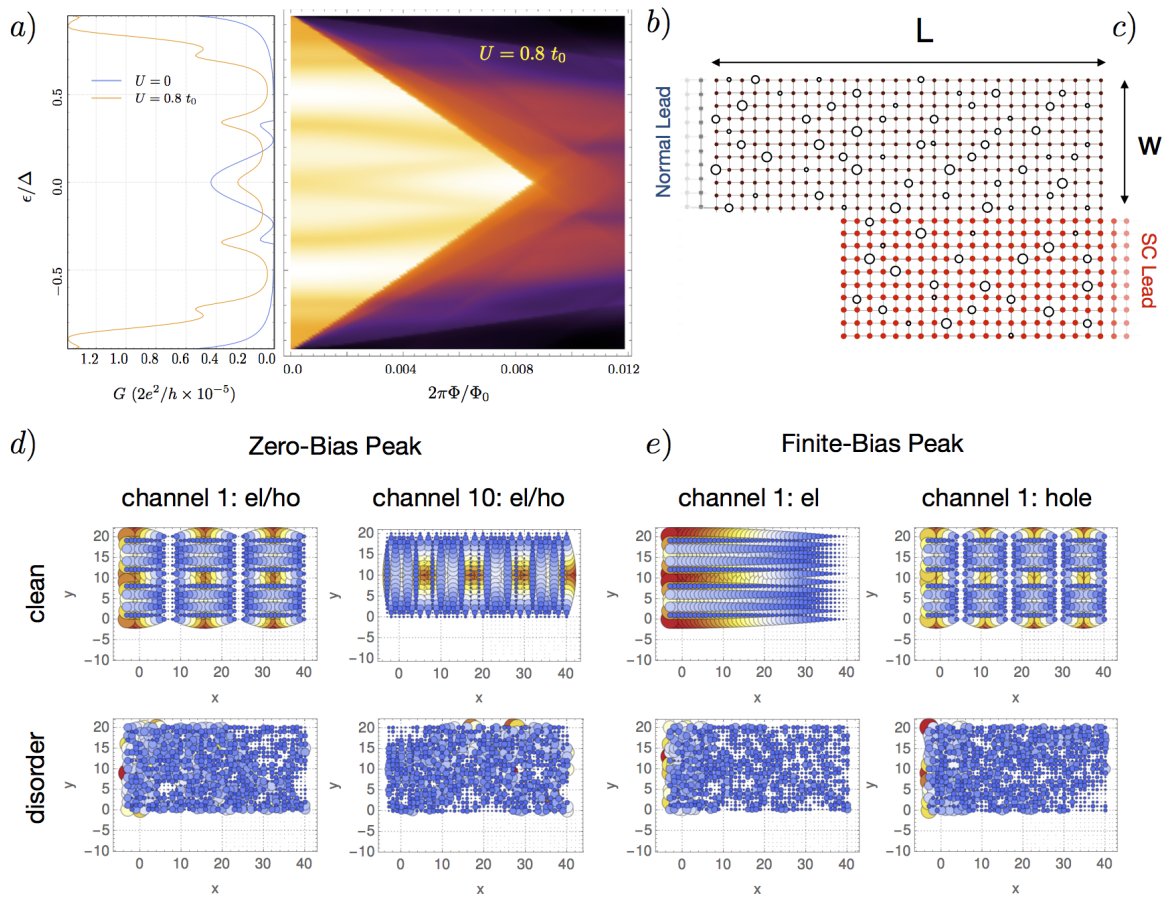

Figure 43: Study of the conductance for a slightly different geometry: $W = 20$ and $L = 40$ lattice sites. a) Conductance for two different values of $U/t_0 = 0, 0.8$. b) Color plot of the conductance as a function of the magnetic field B (abscissa) and the energy ϵ (ordinata) for the case $U = 0.8\ t_0$. c) Device geometry. d) Scattering states of the ZBP for the $U = 0$ and $U = 0.8\ t_0$ for two significant scattering channels. e) Scattering states of the FBP for a given scattering channel. The device is characterized by the following parameters: $t_0 = 1$ eV, $\mu = -2.25\ t_0$, $\Delta = 0.1\ t_0$, $t_1 = 0.01\ t_0$, $g^* = 0$.

$1 - \epsilon|B|/B_2^*$, with $B_2^* \sim 0.5$ T. We interpret these two regions as two different minigap at finite field. Theoretical models predicts that the minigap in large junctions is on order of the Thouless energy and that the orbital magnetic field closes the minigap in a dirty junction [202–206, 210–213]. Here we observe a gap on order of Δ at $B = 0$ and two different values that detach from $\epsilon = \Delta$ and close with different slope with B.

To our knowledge such a behavior has been never observed, nor theoretically predicted. Our numerical results show that the background conductance in a highly disordered NIS junction can develop regions in the plane (ϵ, B) characterized by different background DOS that close with the applied orbital B field with a law that approximately previous

theoretical predictions for a minigap in a diffusive junction [202, 203]. We ascribe these features to the geometry under consideration.

4.4.6 Photon Absorption

Photon absorption processes in NIS junctions produce peaks in conductance. To exclude this process as possible origin of the sub-gap feature, we perform RF measurements. The RF setup comprises of a coaxial cable, connected to a free-standing few-turn coil surrounding the samples. The RF measurements are performed on NIS_8, since the device has no ground plane, which would shunt filter the RF signal. The photon absorption produces copies of the gap peaks (single particle DOS for the superconductor), which we show in Fig. 44 by shifting copies (black and blue traces) of the original data (red curve) in order to overlay the absorption peak of the copy with the gap peak of the original data. The photon absorption peak, produced by the RF signal of frequency f, is shifted by a voltage $V_n = hf/e$ compared to the gap peak, see Fig. 45b.

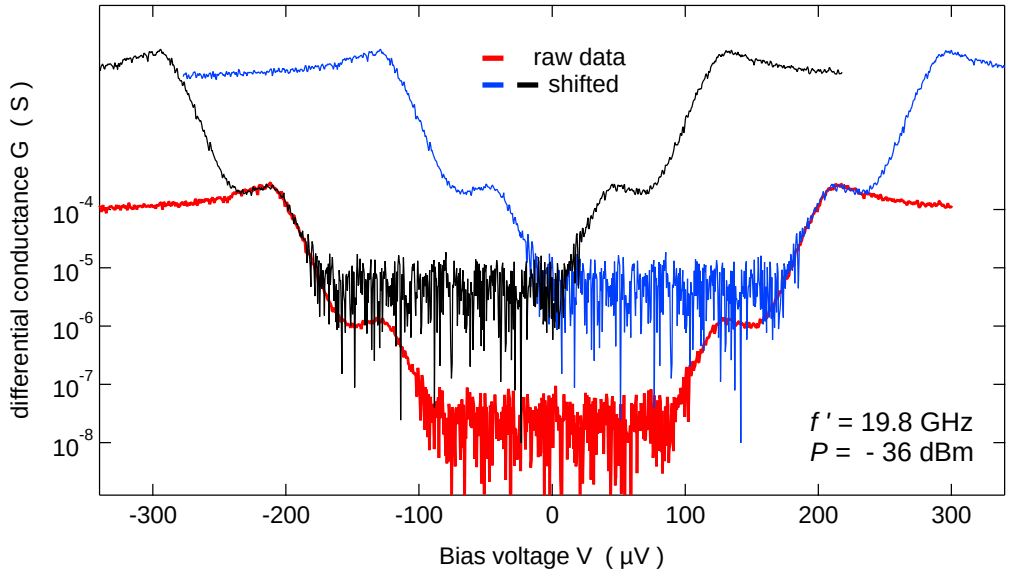

Figure 44: Logarithm of the absolute value of G as a function of the voltage bias for $P = $-36 dBm and $f' = 19.8$ GHz. The blue and the black traces are shifted copies of the original data (red trace).

Next, we compare the shape of the observed sub-gap features with the photon absorption peaks. The sub-gap peaks are symmetric around their bias positions, in contrast

to the photon absorption peaks are asymmetric and being characterized by two different slopes around the maximum of the peak, see Fig. 45d. The different shape of the peak compared to the photon absorption peak indicates that they are due to different processes. To further investigate the origin of the sub-gap peaks, we probe their position as a function of applied RF power normalized to 1 mW $P[dbm]$ and at frequency f. As shown in Fig. 45a. the position of the peaks (indicated by the red arrows) stays constant regardless of f and P, confirming that the sub-gap peaks are not due to photon absorption and they are independent from the RF radiation. Fig. 45e. shows multiphoton absorption for two different frequencies f and f'.

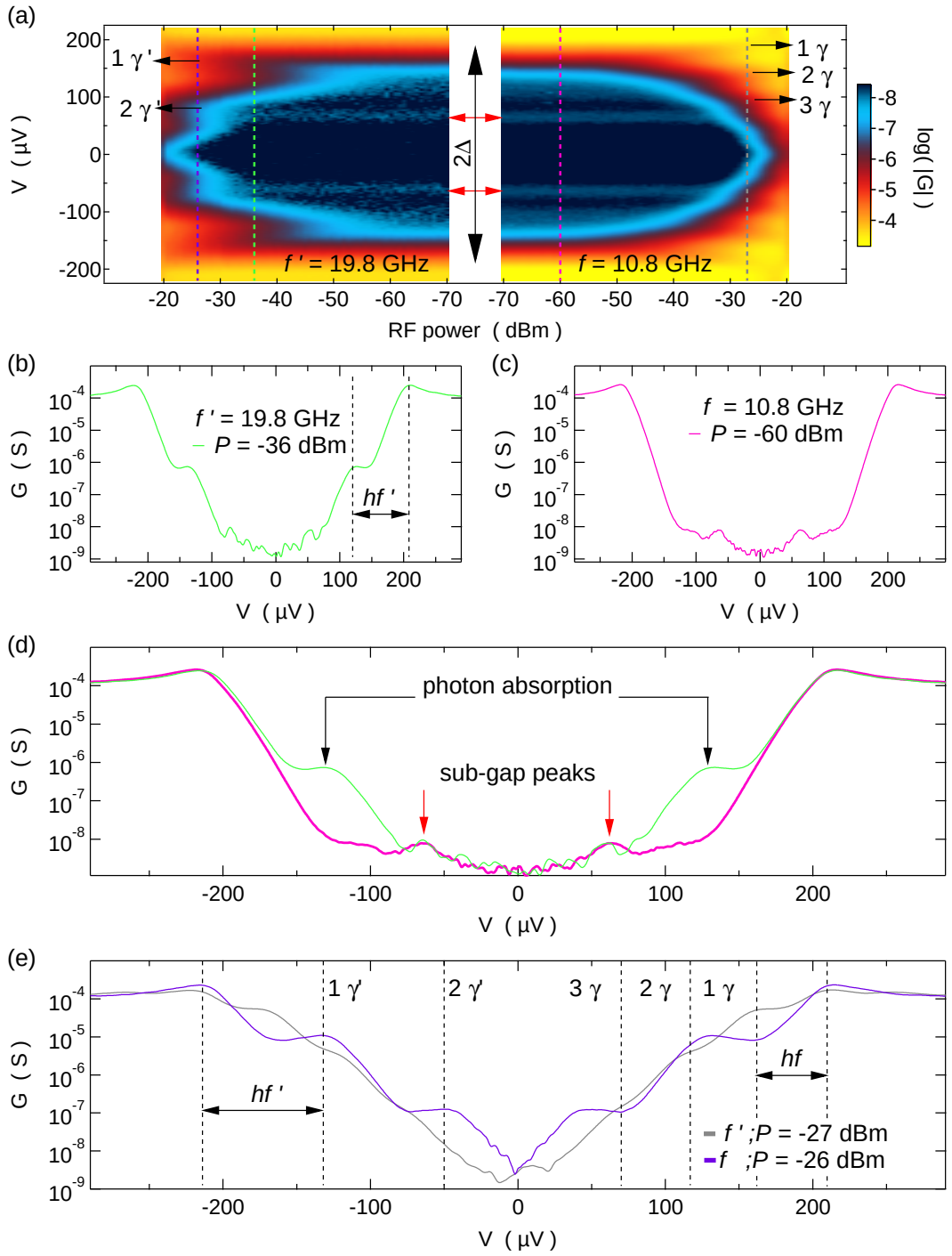

Figure 45: (a) Logarithm of the absolute value of G as a function of P and voltage bias for two different frequencies f and f'. Black arrows indicate the different multiphoton absorption processes. (b) A cut of the color plot shown in (a) for $P = -36$ dBm and $f' = 19.8$ GHz, where one photon is absorbed and it creates a replica of the gap peak shifted by $V_n = hf'/e$. The peaks are narrow features, thus we highlighted them by averaging many cuts at different powers without losing the main features. (c) The averaged cut at $P = -60$ dBm, where the peaks are clearly visible without photon absorption features. (d) Comparison between the cuts shown in (b) and (c), to point out the different shapes between sub-gap peaks and photon absorption peaks. (e) Logarithm of the absolute value of G, showing multiphoton absorption for the two different frequencies.

4.4.7 Perpendicular B-field

The main text shows the dependence of the ZBP and FBPs as a function of the $B_{\parallel}$, while here we present their dependence on the perpendicular magnetic field $B_{\perp}$. As shown in Fig. 46a-d, the zero bias peak is weakly reduced with increasing $B_{\perp}$. This is in agreement with the measurements in $B_{\parallel}$ and the theory of the reflectionless tunneling, confirming that phase coherence interferences, responsible for the ZBP, are destroyed when an external field is applied. Figure 37 of the main text shows that the ZBP is already suppressed for $B_{\parallel}$ higher than the critical field $B_c \sim 130\,\mathrm{mT}$, which is smaller than the $B_{\parallel}$ needed to close the gap. In contrast, the ZBP is visible until the gap of the superconductor is completely closed at $B_{\perp} \sim 10\,\mathrm{mT}$, see Fig. 46a-d, because the junction area, affected by $B_{\perp}$ is larger than the cross section to which $B_{\parallel}$ is orthogonal.

Panels (c) and (d) in Fig. 46 show that the FBPs move to higher energies with increasing $B_{\perp}$, in contrast to the case of $B_{\parallel}$. Additionally, the FBPs have a stronger dependence on $B_{\perp}$, showing changes of energies already at a few mT compared to the 100 mT needed in $B_{\parallel}$ to observe changes of the energies. The different dependence of the FBPs for different field orientations is not yet understood.

The color plots in Fig. 46 show a faint zone (bright color) where the sub-gap conductance G_g is on the order of the normal state conductance and a well defined zone (dark color) where G_g is suddenly reduced by several orders of magnitude. These zones appear at different magnetic fields, which depend on the sweep directions. This dependence of the zones suggest entrance of vortices in the junction area, leading to a local suppression of the superconductivity in the faint region. In contrast when the vortices move out of the junction, the superconductivity is recovered, resulting in a reduction of G_g. This scenario is possible since it has been observed that a thin film of Al behaves as type II superconductor [196, 214, 215], allowing the presence of vortices in the superconducting layer. Additionally, Fig. 46a-d show horizontal spikes, where G locally jumps at different values of $B_{\perp}$. The spikes might be due to the movement of vortices through the junction. The ZBP and the FBPs appear regardless of the spikes

and even at $B_\perp = 0$, indicating that vortices can be excluded as origin of the peaks.

In the main text we show that the temperature T_{slope} is not indicating anymore the right temperature reading once $B_\perp$ is different from zero. To clarify this concept, we show in Figure 46e,f the evolution of the gap as a function of $B_\perp$ for a specific sweep direction and at base temperature of the fridge. The superconducting gap seem to be qualitative very different when approaching the gap at zero magnetic field region (I) and moving away from the zero magnetic field region (II). The gap edges evolve from a soft gap to a hard gap when $B_\perp$ is reduced to zero, see Fig. 46f. Further reducing $B_\perp$ the inflection points of the gap edge move towards the middle of the gap. We conclude that the gap edges are strongly modified by $B_\perp$ and they are not anymore only a function of the temperature and voltage bias.

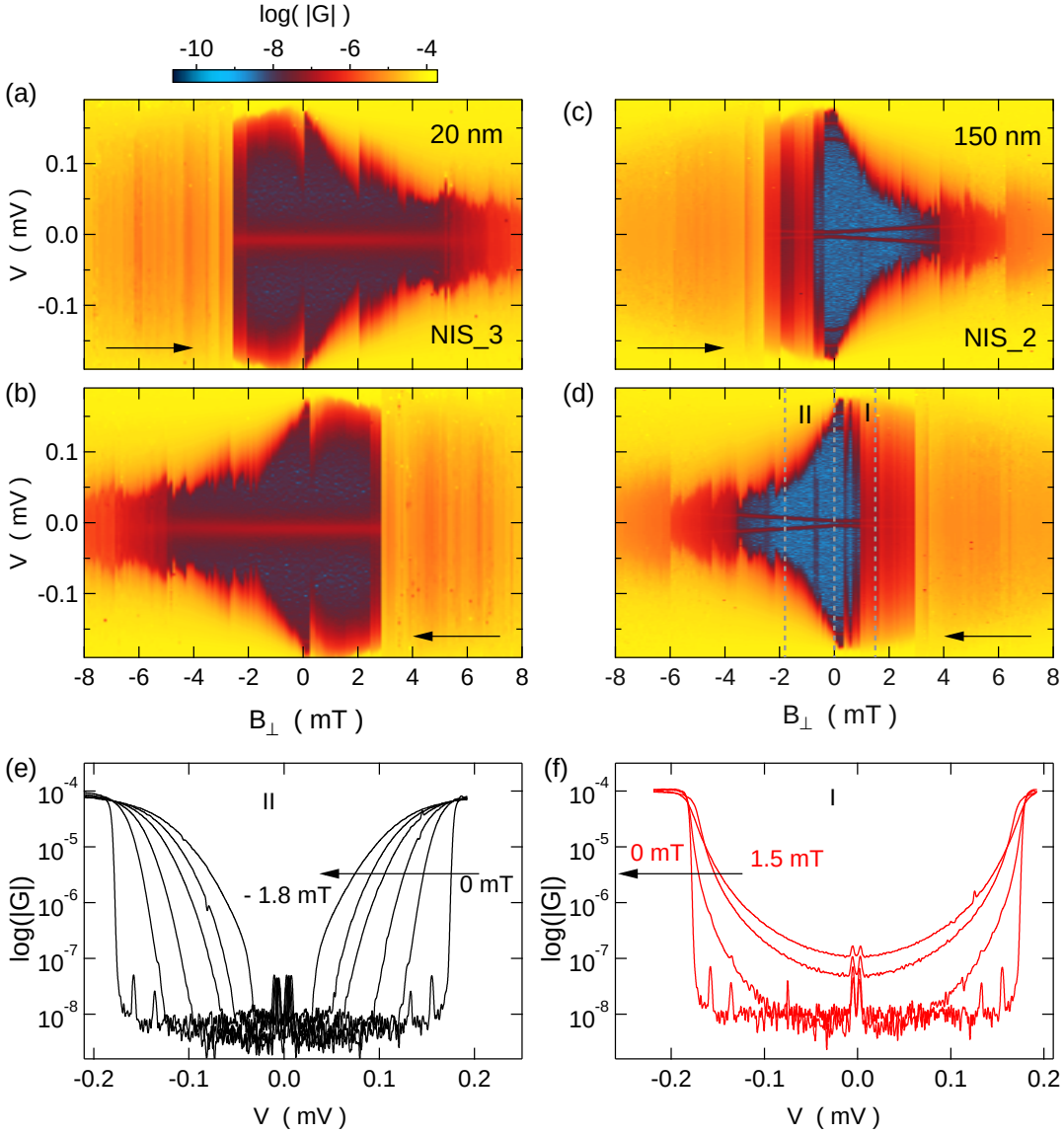

Figure 46: (a-d) Logarithm of the absolute value of the differential conductance is shown as a function of $B_\perp$ and voltage bias. Black arrows indicate the sweep direction of $B_\perp$. The grey dashed lines in (d) indicate two regions I and II of the analysis. (e) Vertical cuts of region II, showing the evolution of the gap . (f) Vertical cuts for the region I.

4.4.8 Demagnetization

We present measurements of the step temperature T_{step} after performing a demagnetization process, which cools the Cu plate temperature T_{Cu} down to $\sim 1\,\mathrm{mK}$. As shown in Fig. 47, T_{step} decreases from roughly 7 mK down to 4 mK in the first few hours after the demagnetization process. The values of T_{step} are scattered around a mean value of 4 mK with a standard deviation of 0.7 mK. The spread of the temperature values and

the lowest temperature might be limited by the voltage noise, which needs to be less than 400 nV to resolve a temperature broadening of 4 mK, by using $eV_{noise} = k_B T_{step}$.

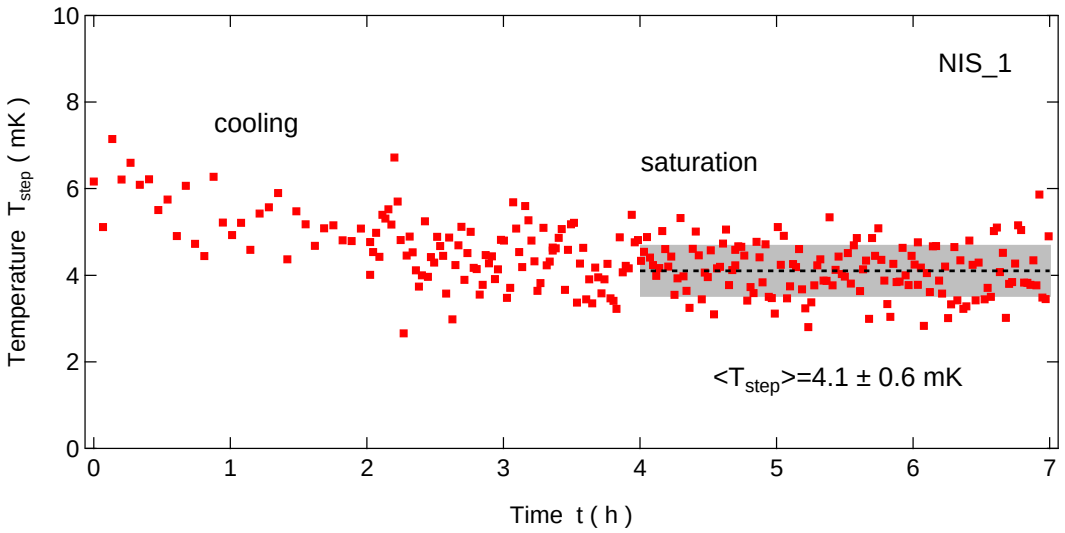

Figure 47: T_{step} as a function of the time after performing an adiabatic nuclear demagnetization. The black dashed line indicates the mean value of T_{step} in the time interval between 4 and 7 hours

5 Summary and Outlook

Edge state spectroscopy

Quantum Hall edge states were studied in a sample with a sharp confinement potential using momentum resolved tunneling spectroscopy. To our knowledge, this is the first time that simultaneous evolution of up to ten lowest Landau level edge states was tracked from formation all the way through to magnetic depopulation. In contrast to a shallow confinement potential, where compressible and in-compressible stripes are formed, for a steep confinement potential the wave functions of different Landau level edge states are located in the same region in space. This makes it very difficult to distinguish different edge states using point-like scanning probes. We exploit the fact that the momentum of each edge state is uniquely defined and measure it using momentum resolved tunneling spectroscopy. Our sample is clean and homogeneous enough to distinguish tunneling from different edge states starting from a perpendicular magnetic field as low as 20 mT.

Interesting correlation phenomena such as fractional quantum Hall effect can only be observed in high quality samples with large electron mobility. For GaAs/AlGaAs heterostructures one of the parameters that has to be optimized during the sample growth is the depth of the 2DEG below the sample surface. To minimize the scattering induced by the impurities and defects at the sample surface, high-mobility 2DEGs are normally buried deep (> 500 nm) below the sample surface. This increases the electron mean-free path but reduces accessibility to interesting states that exist in the 2DEG by standard imaging techniques such as STM or AFM. Our technique overcomes this limitation utilizing the quantum wire embedded during the sample growth process very close to the high mobility 2DEG, giving sub nanometer special resolution of the guiding center position of the integer quantum Hall edge states at moderate magnetic field values (≈ 1T).

The described technique only requires a small AC excitation voltage ($6\,\mu$V), therefore is noninvasive and does not involve any moving elements, so can be performed at milikelvin temperatures, making it very attractive for studying fragile states, for example fractional quantum Hall effect. This could reveal the composition and location of the fractional quantum Hall edge states.

All the tunneling experiments presented in this thesis were performed at zero DC bias voltage, which ensures that electrons involved in the tunneling were taken from the Fermi surface of the upper system and were placed at the Fermi level of the lower wire. At finite DC bias the tunneling involves electrons located above or blow the Fermi level, thus allowing one to probe the dispersion relations of the states involved in the tunneling. The slopes of these dispersions could be used to extract the propagation velocity of the edge states - a fundamental parameter characterizing the edge states. The detailed analysis of the intensity of the tunneling resonances combined with self-consistent calculations of the electron density and electrostatic confinement potentials could be used to experimentally and theoretically investigate the quantum Hall edge state wavefunctions.

This technique is analogous to Raman spectroscopy with the advantage that a large momentum difference between probed and probing states can be achieved using experimentally accessible magnetic fields. It must, however, be mentioned that the explored technique can be only used in specially designed samples, where the system of interest, in our case 2DEG with the integer quantum Hall edge states, is tunnel-coupled to the 1D quantum wire. One important parameter in such experiments is a center-to-center distance between the two systems. On the one hand, this distance has to be small to ensure a measurable tunneling current. On the other hand, it has to be sufficiently large, as it is directly linked to the momentum boost induced by the external magnetic field. This distance also has to be very uniform throughout the entire length of the tunnel junction, otherwise the tunneling resonances would be additionally broadened. It would be very interesting to apply the described technique to probe the edge or

surface states of novel materials, for example, topological insulators.

References

[1] L. Pfeiffer, H. Störmer, K. Baldwin, K. West, A. Goñi, A. Pinczuk, R. Ashoori, M. Dignam, and W. Wegscheider. *Cleaved edge overgrowth for quantum wire fabrication.* Journal of Crystal Growth **127**, 849 (1993).

[2] A. Yacoby, H. Stormer, K. Baldwin, L. Pfeiffer, and K. West. *Magneto-transport spectroscopy on a quantum wire.* Solid State Communications **101**, 77 (1997).

[3] D. L. Maslov and M. Stone. *Landauer conductance of Luttinger liquids with leads.* Physical Review B **52**, R5539 (1995).

[4] I. Safi and H. J. Schulz. *Transport in an inhomogeneous interacting one-dimensional system.* Physical Review B **52**, R17040 (1995).

[5] V. V. Ponomarenko. *Renormalization of the one-dimensional conductance in the Luttinger-liquid model.* Physical Review B **52**, R8666 (1995).

[6] D. L. Maslov. *Transport through dirty Luttinger liquids connected to reservoirs.* Physical Review B **52**, R14368 (1995).

[7] S. Tarucha, T. Honda, and T. Saku. *Reduction of quantized conductance at low temperatures observed in 2 to 10 μm-long quantum wires.* Solid State Communications **94**, 413 (1995).

[8] C. P. Scheller, T. M. Liu, G. Barak, A. Yacoby, L. N. Pfeiffer, K. W. West, and D. M. Zumbühl. *Possible evidence for helical nuclear spin order in GaAs quantum wires.* Physical Review Letters **112**, 1 (2014).

[9] C. P. Scheller, S. Heizmann, K. Bedner, D. Giss, M. Meschke, D. M. Zumbühl, J. D. Zimmerman, and A. C. Gossard. *Silver-epoxy microwave filters and thermalizers for millikelvin experiments.* Applied Physics Letters **104** (2014).

[10] B. Braunecker, P. Simon, and D. Loss. *Nuclear magnetism and electron order in interacting one-dimensional conductors.* Physical Review B **80**, 165119 (2009).

[11] B. Braunecker, G. I. Japaridze, J. Klinovaja, and D. Loss. *Spin-selective Peierls transition in interacting one-dimensional conductors with spin-orbit interaction.* Physical Review B **82**, 045127 (2010).

[12] B. Braunecker, P. Simon, and D. Loss. *Nuclear Magnetism and Electronic Order in ^{13}C Nanotubes.* Physical Review Letters **102**, 116403 (2009).

[13] H. Steinberg, G. Barak, A. Yacoby, L. N. Pfeiffer, K. W. West, B. I. Halperin, and K. Le Hur. *Charge fractionalization in quantum wires.* Nature Physics **4**, 116 (2008).

[14] O. M. Auslaender, A. Yacoby, R. de Picciotto, K. W. Baldwin, L. N. Pfeiffer, and K. W. West. *Experimental Evidence for Resonant Tunneling in a Luttinger Liquid.* Physical Review Letters **84**, 1764 (2000).

[15] L. P. Kouwenhoven, G. Schön, and L. L. Sohn. *Introduction to Mesoscopic Electron Transport.* In *Mesoscopic Electron Transport*, 1–44 (Springer Netherlands, Dordrecht, 1997).

[16] A. Furusaki. *Resonant tunneling through a quantum dot weakly coupled to quantum wires or quantum Hall edge states.* Physical Review B **57**, 7141 (1998).

[17] M. Bockrath, D. H. Cobden, J. Lu, A. G. Rinzler, R. E. Smalley, L. Balents, and P. L. McEuen. *Luttinger-liquid behaviour in carbon nanotubes.* Nature **397**, 598 (1999).

[18] T. Kleimann, M. Sassetti, A. Yacoby, and B. Kramer. *Charge and spin addition energies of a one-dimensional quantum dot.* Physical Review B - Condensed Matter and Materials Physics **62**, 8144 (2000).

[19] O. M. Auslaender, A. Yacoby, R. De Picciotto, K. W. Baldwin, L. N. Pfeiffer, and K. W. West. *Tunneling spectroscopy of the elementary excitations in a one-dimensional wire.* Science **295**, 825 (2002).

[20] J. T. Devreese, R. P. Evrard, and V. E. van Doren. *Highly Conducting One Dimensional Solids* (1979).

[21] O. M. Auslaender. *Spin-Charge Separation and Localization in One Dimension.* Science **308**, 88 (2005).

[22] D. Carpentier, C. Peça, and L. Balents. *Momentum-resolved tunneling between Luttinger liquids.* Physical Review B - Condensed Matter and Materials Physics **66**, 1 (2002).

[23] D. Boese, M. Governale, A. Rosch, and U. Zülicke. *Mesoscopic effects in tunneling between parallel quantum wires.* Physical Review B **64**, 085315 (2001).

[24] A. V. Lebedev, A. Crépieux, and T. Martin. *Electron injection in a nanotube with leads: Finite-frequency noise correlations and anomalous charges.* Physical Review B - Condensed Matter and Materials Physics **71**, 1 (2005).

[25] C. Bena, S. Vishveshwara, L. Balents, and M. P. A. Fisher. *Measuring Fractional Charge in Carbon Nanotubes.* Journal of Statistical Physics **103**, 429 (2001).

[26] K.-I. Imura, K.-V. Pham, P. Lederer, and F. Piéchon. *Conductance of one-dimensional quantum wires.* Physical Review B **66**, 035313 (2002).

[27] S. Bosco and D. P. Divincenzo. *Transmission lines and resonators based on quantum Hall plasmonics: electromagnetic field, attenuation and coupling to qubits* 1–31 (2019).

[28] S. Bosco, D. P. Divincenzo, and D. J. Reilly. *Transmission Lines and Meta-Materials based on Quantum Hall Plasmonics.* arXiv Applied Physics 1–16 (2018).

[29] K. v. Klitzing, G. Dorda, and M. Pepper. *New Method for High-Accuracy Determination of the Fine-Structure Constant Based on Quantized Hall Resistance.* Physical Review Letters **45**, 494 (1980).

[30] D. C. Tsui and A. C. Gossard. *Resistance standard using quantization of the Hall resistance of GaAs/AlGaAs heterostructures.* Applied Physics Letters **38**, 550 (1981).

[31] D. C. Tsui, H. L. Stormer, and A. C. Gossard. *Two-dimensional magnetotransport in the extreme quantum limit.* Physical Review Letters **48**, 1559 (1982).

[32] B. I. Halperin. *Quantized Hall conductance, current-carrying edge states, and the existence of extended states in a two-dimensional disordered potential.* Physical Review B **25**, 2185 (1982).

[33] L. Schweitzer, B. Kramer, and A. MacKinnon. *Magnetic field and electron states in two-dimensional disordered systems.* Journal of Physics C: Solid State Physics **17**, 4111 (1984).

[34] D. B. Chklovskii, B. I. Shklovskii, and L. I. Glazman. *Electrostatics of edge channels.* Physical Review B **46**, 4026 (1992).

[35] Y. Y. Wei, J. Weis, K. v. Klitzing, and K. Eberl. *Edge Strips in the Quantum Hall Regime Imaged by a Single-Electron Transistor.* Physical Review Letters **81**, 1674 (1998).

[36] Y. Y. Wei, J. Weis, K. v. Klitzing, and K. Eberl. *Single-electron transistor as an electrometer measuring chemical potential variations.* Applied Physics Letters **71**, 2514 (1997).

[37] V. Gudmundsson and R. R. Gerhardts. *Interpretation of experiments implying density of states between Landau levels of a two-dimensional electron gas by a statistical model for inhomogeneities.* Physical Review B **35**, 8005 (1987).

[38] S. H. Tessmer, P. I. Glicofridis, R. C. Ashoori, L. S. Levitov, and M. R. Melloch. *Subsurface charge accumulation imaging of a quantum Hall liquid.* Nature **392**, 51 (1998).

[39] K. L. McCormick, M. T. Woodside, M. Huang, M. Wu, P. L. McEuen, C. Duruoz, and J. S. Harris. *Scanned potential microscopy of edge and bulk currents in the quantum Hall regime.* Physical Review B **59**, 4654 (1999).

[40] A. Yacoby, H. Hess, T. Fulton, L. Pfeiffer, and K. West. *Electrical imaging of the quantum Hall state.* Solid State Communications **111**, 1 (1999).

[41] A. H. MacDonald and P. Středa. *Quantized Hall effect and edge currents.* Physical Review B **29**, 1616 (1984).

[42] T. Patlatiuk, C. P. Scheller, D. Hill, Y. Tserkovnyak, G. Barak, A. Yacoby, L. N. Pfeiffer, K. W. West, and D. M. Zumbühl. *Landau Level Wave-Functions and the Density Profile at Sharp Edges* (in preparation for publication).

[43] C. D. C. Chamon and X. G. Wen. *Sharp and smooth boundaries of quantum Hall liquids.* Physical Review B **49**, 8227 (1994).

[44] G. Moore and N. Read. *Nonabelions in the fractional quantum hall effect.* Nuclear Physics B **360**, 362 (1991).

[45] S. Das Sarma, M. Freedman, and C. Nayak. *Topologically Protected Qubits from a Possible Non-Abelian Fractional Quantum Hall State.* Physical Review Letters **94**, 166802 (2005).

[46] C. Nayak, S. H. Simon, A. Stern, M. Freedman, and S. Das Sarma. *Non-Abelian anyons and topological quantum computation.* Reviews of Modern Physics **80**, 1083 (2008).

[47] A. M. Chang, L. N. Pfeiffer, and K. W. West. *Observation of Chiral Luttinger Behavior in Electron Tunneling into Fractional Quantum Hall Edges.* Physical Review Letters **77**, 2538 (1996).

[48] G. Li, A. Luican-Mayer, D. Abanin, L. Levitov, and E. Y. Andrei. *Evolution of Landau levels into edge states in graphene.* Nature Communications **4**, 1744 (2013).

[49] K. S. Novoselov. *Electric Field Effect in Atomically Thin Carbon Films.* Science **306**, 666 (2004).

[50] K. Bolotin, K. Sikes, Z. Jiang, M. Klima, G. Fudenberg, J. Hone, P. Kim, and H. Stormer. *Ultrahigh electron mobility in suspended graphene.* Solid State Communications **146**, 351 (2008).

[51] C. R. Dean, A. F. Young, I. Meric, C. Lee, L. Wang, S. Sorgenfrei, K. Watanabe, T. Taniguchi, P. Kim, K. L. Shepard, and J. Hone. *Boron nitride substrates for high-quality graphene electronics.* Nature Nanotechnology **5**, 722 (2010).

[52] I. K. Drozdov, A. Alexandradinata, S. Jeon, S. Nadj-Perge, H. Ji, R. J. Cava, B. Andrei Bernevig, and A. Yazdani. *One-dimensional topological edge states of bismuth bilayers.* Nature Physics **10**, 664 (2014).

[53] F. Yang, L. Miao, Z. F. Wang, M.-Y. Yao, F. Zhu, Y. R. Song, M.-X. Wang, J.-P. Xu, A. V. Fedorov, Z. Sun, G. B. Zhang, C. Liu, F. Liu, D. Qian, C. L. Gao, and J.-F. Jia. *Spatial and Energy Distribution of Topological Edge States in Single Bi(111) Bilayer.* Physical Review Letters **109**, 016801 (2012).

[54] L. Peng, Y. Yuan, G. Li, X. Yang, J.-J. Xian, C.-J. Yi, Y.-G. Shi, and Y.-S. Fu. *Observation of topological states residing at step edges of WTe_2.* Nature Communications **8**, 659 (2017).

[55] Z. F. Wang, H. Zhang, D. Liu, C. Liu, C. Tang, C. Song, Y. Zhong, J. Peng, F. Li, C. Nie, L. Wang, X. J. Zhou, X. Ma, Q. K. Xue, and F. Liu. *Topological edge states in a high-temperature superconductor $FeSe/SrTiO_3(001)$ film.* Nature Materials **15**, 968 (2016).

[56] M. König, S. Wiedmann, C. Brüne, A. Roth, H. Buhmann, L. W. Molenkamp, X.-L. Qi, and S.-C. Zhang. *Quantum Spin Hall Insulator State in HgTe Quantum Wells.* Science **318**, 766 (2007).

[57] K. C. Nowack, E. M. Spanton, M. Baenninger, M. König, J. R. Kirtley, B. Kalisky, C. Ames, P. Leubner, C. Brüne, H. Buhmann, L. W. Molenkamp, D. Goldhaber-Gordon, and K. A. Moler. *Imaging currents in* HgTe *quantum wells in the quantum spin hall regime.* Nat. Mater. **12**, 787 (2013).

[58] J. Weis and K. von Klitzing. *Metrology and microscopic picture of the integer quantum Hall effect.* Philosophical Transactions of the Royal Society A: Mathematical, Physical and Engineering Sciences **369**, 3954 (2011).

[59] M. E. Suddards, A. Baumgartner, M. Henini, and C. J. Mellor. *Scanning capacitance imaging of compressible and incompressible quantum Hall effect edge strips.* New Journal of Physics **14**, 083015 (2012).

[60] D. Zhang, S. Schmult, V. Venkatachalam, W. Dietsche, A. Yacoby, K. von Klitzing, and J. Smet. *Local compressibility measurement of the* $\nu_{tot} = 1$ *quantum Hall state in a bilayer electron system.* Physical Review B **87**, 205304 (2013).

[61] N. Pascher, C. Rössler, T. Ihn, K. Ensslin, C. Reichl, and W. Wegscheider. *Imaging the Conductance of Integer and Fractional Quantum Hall Edge States.* Phys. Rev. X **4**, 011014 (2014).

[62] L.-J. Yin, H. Jiang, J.-B. Qiao, and L. He. *Direct imaging of topological edge states at a bilayer graphene domain wall.* Nature Communications **7**, 11760 (2016).

[63] K. Panos, R. R. Gerhardts, J. Weis, and K. von Klitzing. *Current distribution and Hall potential landscape towards breakdown of the quantum Hall effect: a scanning force microscopy investigation.* New Journal of Physics **16**, 113071 (2014).

[64] F. Dahlem, E. Ahlswede, J. Weis, and K. v. Klitzing. *Cryogenic scanning force microscopy of quantum Hall samples: Adiabatic transport originating in anisotropic depletion at contact interfaces.* Physical Review B **82**, 121305 (2010).

[65] A. Yacoby, H. L. Stormer, N. S. Wingreen, L. N. Pfeiffer, K. W. Baldwin, and K. W. West. *Nonuniversal Conductance Quantization in Quantum Wires.* Physical Review Letters **77**, 4612 (1996).

[66] O. M. Auslaender. *Spin-Charge Separation and Localization in One Dimension.* Science **308**, 88 (2005).

[67] B. Braunecker, P. Simon, and D. Loss. *Nuclear magnetism and electron order in interacting one-dimensional conductors.* Phys. Rev. B **80**, 165119 (2009).

[68] B. I. Halperin. *Quantized Hall conductance, current-carrying edge states, and the existence of extended states in a two-dimensional disordered potential.* Physical Review B **25**, 2185 (1982).

[69] M. Büttiker. *Absence of backscattering in the quantum Hall effect in multiprobe conductors.* Physical Review B **38**, 9375 (1988).

[70] M. Huber, M. Grayson, M. Rother, R. Deutschmann, W. Biberacher, W. Wegscheider, M. Bichler, and G. Abstreiter. *Tunneling in the quantum Hall regime between orthogonal quantum wells.* Physica E: Low-dimensional Systems and Nanostructures **12**, 125 (2002).

[71] M. Huber, M. Grayson, D. Schuh, M. Bichler, W. Biberacher, W. Wegscheider, and G. Abstreiter. *Probing the electrostatics of integer quantum hall edges with momentum-resolved tunnel spectroscopy.* Physica E: Low-dimensional Systems and Nanostructures **22**, 164 (2004).

[72] M. Huber, M. Grayson, M. Rother, W. Biberacher, W. Wegscheider, and G. Abstreiter. *Structure of a single sharp quantum Hall edge probed by momentum-resolved tunneling.* Physical Review Letters **94** (2005).

[73] L. Pfeiffer, H. Störmer, K. Baldwin, K. West, A. Goñi, A. Pinczuk, R. Ashoori, M. Dignam, and W. Wegscheider. *Cleaved edge overgrowth for quantum wire fabrication.* Journal of Crystal Growth **127**, 849 (1993).

[74] W. Wegscheider, W. Kang, L. Pfeiffer, K. West, H. Stormer, and K. Baldwin. *High-mobility transport along single quasi-1D quantum wires formed by cleaved edge overgrowth.* Solid-State Electronics **37**, 547 (1994).

[75] O. M. Auslaender, A. Yacoby, R. De Picciotto, K. W. Baldwin, L. N. Pfeiffer, and K. W. West. *Tunneling spectroscopy of the elementary excitations in a one-dimensional wire.* Science **295**, 825 (2002).

[76] H. Steinberg, O. M. Auslaender, A. Yacoby, J. Qian, G. A. Fiete, Y. Tserkovnyak, B. I. Halperin, K. W. Baldwin, L. N. Pfeiffer, and K. W. West. *Localization transition in a ballistic quantum wire.* Phys. Rev. B **73**, 113307 (2006).

[77] Y. Tserkovnyak, B. I. Halperin, O. M. Auslaender, and A. Yacoby. *Finite-Size Effects in Tunneling between Parallel Quantum Wires.* Physical Review Letters **89**, 136805 (2002).

[78] Y. Tserkovnyak, B. I. Halperin, O. M. Auslaender, and A. Yacoby. *Interference and zero-bias anomaly in tunneling between Luttinger-liquid wires.* Physical Review B **68**, 125312 (2003).

[79] M. Grayson, L. Steinke, D. Schuh, M. Bichler, L. Hoeppel, J. Smet, K. v. Klitzing, D. K. Maude, and G. Abstreiter. *Metallic and insulating states at a bent quantum Hall junction.* Physical Review B **76**, 201304 (2007).

[80] L. Steinke, P. Cantwell, E. Stach, D. Schuh, A. Fontcuberta I Morral, M. Bichler, G. Abstreiter, and M. Grayson. *Hartree simulations of coupled quantum Hall edge states in corner-overgrown heterostructures.* Physical Review B - Condensed Matter and Materials Physics **87**, 1 (2013).

[81] L. Onsager. *Reciprocal Relations in Irreversible Processes. I.* Physical Review **37**, 405 (1931).

[82] K. Lier and R. R. Gerhardts. *Self-consistent calculations of edge channels in laterally confined two-dimensional electron systems.* Physical Review B **50**, 7757 (1994).

[83] K. Güven and R. R. Gerhardts. *Self-consistent local equilibrium model for density profile and distribution of dissipative currents in a Hall bar under strong magnetic fields.* Physical Review B **67**, 115327 (2003).

[84] A. Siddiki and R. R. Gerhardts. *Thomas-Fermi-Poisson theory of screening for laterally confined and unconfined two-dimensional electron systems in strong magnetic fields.* Phys. Rev. B **68**, 125315 (2003).

[85] A. Siddiki and R. R. Gerhardts. *Incompressible strips in dissipative Hall bars as origin of quantized Hall plateaus.* Physical Review B - Condensed Matter and Materials Physics **70**, 1 (2004).

[86] S. Baer, C. Rössler, E. C. de Wiljes, P. L. Ardelt, T. Ihn, K. Ensslin, C. Reichl, and W. Wegscheider. *Interplay of fractional quantum Hall states and localization in quantum point contacts.* Phys. Rev. B **89**, 85424 (2014).

[87] R. R. Gerhardts, K. Panos, and J. Weis. *Current-induced asymmetries of incompressible strips in narrow quantum Hall systems.* New Journal of Physics **15**, 073034 (2013).

[88] O. E. Dial, R. C. Ashoori, L. N. Pfeiffer, and K. W. West. *High-resolution spectroscopy of two-dimensional electron systems.* Nature **448**, 176 (2007).

[89] O. E. Dial, R. C. Ashoori, L. N. Pfeiffer, and K. W. West. *Anomalous structure in the single particle spectrum of the fractional quantum Hall effect.* Nature **464**, 566 (2010).

[90] R. J. Nicholas, R. J. Haug, K. v. Klitzing, and G. Weimann. *Exchange enhancement of the spin splitting in a GaAs-$Ga_xAl_{1-x}As$ heterojunction.* Physical Review B **37**, 1294 (1988).

[91] J. Dempsey, B. Y. Gelfand, and B. I. Halperin. *Electron-electron interactions and spontaneous spin polarization in quantum Hall edge states.* Physical Review Letters **70**, 3639 (1993).

[92] F. D. M. Haldane. *'Luttinger liquid theory' of one-dimensional quantum fluids. I. Properties of the Luttinger model and their extension to the general 1D interacting spinless Fermi gas.* Journal of Physics C: Solid State Physics **14**, 2585 (1981).

[93] F. D. M. Haldane. *Effective Harmonic-Fluid Approach to Low-Energy Properties of One-Dimensional Quantum Fluids.* Physical Review Letters **47**, 1840 (1981).

[94] U. Zuelicke, E. Shimshoni, and M. Governale. *Momentum-Resolved Tunneling into Fractional Quantum Hall Edges.* Physical Review B **65**, 241315 (2002).

[95] A. Seidel and K. Yang. *Momentum-resolved tunneling into the Pfaffian and anti-Pfaffian edges.* Physical Review B **80**, 241309 (2009).

[96] A. C. Clark, K. K. Schwarzwälder, T. Bandi, D. Maradan, and D. M. Zumbühl. *Method for cooling nanostructures to microkelvin temperatures.* Review of Scientific Instruments **81**, 103904 (2010).

[97] L. Casparis, M. Meschke, D. Maradan, A. C. Clark, C. P. Scheller, K. K. Schwarzwälder, J. P. Pekola, and D. M. Zumbühl. *Metallic Coulomb blockade thermometry down to 10 mK and below.* Review of Scientific Instruments **83**, 083903 (2012).

[98] D. Maradan, L. Casparis, T.-M. Liu, D. E. F. Biesinger, C. P. Scheller, D. M. Zumbühl, J. D. Zimmerman, and A. C. Gossard. *GaAs Quantum Dot Thermometry Using Direct Transport and Charge Sensing.* Journal of Low Temperature Physics **175**, 784 (2014).

[99] A. V. Feshchenko, L. Casparis, I. M. Khaymovich, D. Maradan, O. P. Saira, M. Palma, M. Meschke, J. P. Pekola, and D. M. Zumbühl. *Tunnel-Junction Thermometry Down to Millikelvin Temperatures.* Physical Review Applied **4**, 1 (2015).

[100] M. Palma, C. P. Scheller, D. Maradan, A. V. Feshchenko, M. Meschke, and D. M. Zumbühl. *On-and-off chip cooling of a Coulomb blockade thermometer down to 2.8 mK.* Applied Physics Letters **111**, 253105 (2017).

[101] M. Palma, D. Maradan, L. Casparis, T.-M. Liu, F. N. M. Froning, and D. M. Zumbühl. *Magnetic cooling for microkelvin nanoelectronics on a cryofree platform.* Review of Scientific Instruments **88**, 043902 (2017).

[102] G. Barak, H. Steinberg, L. N. Pfeiffer, K. W. West, L. Glazman, F. von Oppen, and A. Yacoby. *Interacting electrons in one dimension beyond the Luttinger-liquid limit.* Nature Physics **6**, 489 (2010).

[103] R. de Picciotto, H. L. Stormer, L. N. Pfeiffer, K. W. Baldwin, and K. W. West. *Four-terminal resistance of a ballistic quantum wire.* Nature **411**, 51 (2001).

[104] T. Meng and D. Loss. *Helical nuclear spin order in two-subband quantum wires.* Physical Review B **87**, 235427 (2013).

[105] D. Loss and D. P. DiVincenzo. *Quantum computation with quantum dots.* Physical Review A **57**, 120 (1998).

[106] D. Kielpinski, C. Monroe, and D. J. Wineland. *Architecture for a large-scale ion-trap quantum computer.* Nature **417**, 709 (2002).

[107] D. Gottesman. *An introduction to quantum error correction and fault-tolerant quantum computation.* 13–58 (2010).

[108] D. J. Reilly. *Engineering the quantum-classical interface of solid-state qubits.* npj Quantum Information **1**, 15011 (2015).

[109] J. M. Gambetta, J. M. Chow, and M. Steffen. *Building logical qubits in a superconducting quantum computing system.* npj Quantum Information **3**, 2 (2017).

[110] S. Takahashi, I. S. Tupitsyn, J. van Tol, C. C. Beedle, D. N. Hendrickson, and P. C. E. Stamp. *Decoherence in crystals of quantum molecular magnets.* Nature **476**, 76 (2011).

[111] J. Goetz, F. Deppe, P. Eder, M. Fischer, M. Müting, J. P. Martínez, S. Pogorzalek, F. Wulschner, E. Xie, K. G. Fedorov, A. Marx, and R. Gross. *Second-order decoherence mechanisms of a transmon qubit probed with thermal microwave states.* Quantum Science and Technology **2**, 025002 (2017).

[112] A. Kitaev. *Fault-tolerant quantum computation by anyons.* Annals of Physics **303**, 2 (2003).

[113] A. Stern and N. H. Lindner. *Topological Quantum Computation–From Basic Concepts to First Experiments.* Science **339**, 1179 (2013).

[114] A. Y. Kitaev. *Unpaired Majorana fermions in quantum wires.* Physics-Uspekhi **44**, 131 (2001).

[115] J. Klinovaja and D. Loss. *Parafermions in an Interacting Nanowire Bundle.* Physical Review Letters **112**, 246403 (2014).

[116] J. Klinovaja and D. Loss. *Time-reversal invariant parafermions in interacting Rashba nanowires.* Physical Review B **90**, 045118 (2014).

[117] V. Mourik, K. Zuo, S. M. Frolov, S. R. Plissard, E. P. A. M. Bakkers, and L. P. Kouwenhoven. *Signatures of Majorana Fermions in Hybrid Superconductor-Semiconductor Nanowire Devices.* Science **336**, 1003 (2012).

[118] A. Das, Y. Ronen, Y. Most, Y. Oreg, M. Heiblum, and H. Shtrikman. *Zero-bias peaks and splitting in an Al-InAs nanowire topological superconductor as a signature of Majorana fermions.* Nature Physics **8**, 887 (2012).

[119] S. M. Albrecht, A. P. Higginbotham, M. Madsen, F. Kuemmeth, T. S. Jespersen, J. Nygård, P. Krogstrup, and C. M. Marcus. *Exponential protection of zero modes in Majorana islands.* Nature **531**, 206 (2016).

[120] M. T. Deng, C. L. Yu, G. Y. Huang, M. Larsson, P. Caroff, and H. Q. Xu. *Anomalous Zero-Bias Conductance Peak in a Nb-InSb Nanowire-Nb Hybrid Device.* Nano Letters **12**, 6414 (2012).

[121] Y.-H. Lee, X.-Q. Zhang, W. Zhang, M.-T. Chang, C.-T. Lin, K.-D. Chang, Y.-C. Yu, J. T.-W. Wang, C.-S. Chang, L.-J. Li, and T.-W. Lin. *Synthesis of Large-Area MoS 2 Atomic Layers with Chemical Vapor Deposition.* Advanced Materials **24**, 2320 (2012).

[122] E. J. H. Lee, X. Jiang, M. Houzet, R. Aguado, C. M. Lieber, and S. De Franceschi. *Spin-resolved Andreev levels and parity crossings in hybrid superconductor-semiconductor nanostructures.* Nature Nanotechnology **9**, 79 (2014).

[123] R. M. Lutchyn, E. P. A. M. Bakkers, L. P. Kouwenhoven, P. Krogstrup, C. M. Marcus, and Y. Oreg. *Majorana zero modes in superconductor-semiconductor heterostructures.* Nature Reviews Materials **3**, 52 (2018).

[124] J. Alicea, Y. Oreg, G. Refael, F. von Oppen, and M. P. A. Fisher. *Non-Abelian statistics and topological quantum information processing in 1D wire networks.* Nature Physics **7**, 412 (2011).

[125] S. Gazibegovic, D. Car, H. Zhang, S. C. Balk, J. A. Logan, M. W. A. de Moor, M. C. Cassidy, R. Schmits, D. Xu, G. Wang, P. Krogstrup, R. L. M. Op het Veld, K. Zuo, Y. Vos, J. Shen, D. Bouman, B. Shojaei, D. Pennachio, J. S. Lee, P. J. van Veldhoven, S. Koelling, M. A. Verheijen, L. P. Kouwenhoven, C. J. Palmstrøm, and E. P. A. M. Bakkers. *Epitaxy of advanced nanowire quantum devices.* Nature **548**, 434 (2017).

[126] S. R. Plissard, I. van Weperen, D. Car, M. A. Verheijen, G. W. G. Immink, J. Kammhuber, L. J. Cornelissen, D. B. Szombati, A. Geresdi, S. M. Frolov, L. P. Kouwenhoven, and E. P. A. M. Bakkers. *Formation and electronic properties of InSb nanocrosses.* Nature Nanotechnology **8**, 859 (2013).

[127] J. Gooth, M. Borg, H. Schmid, V. Schaller, S. Wirths, K. Moselund, M. Luisier, S. Karg, and H. Riel. *Ballistic One-Dimensional InAs Nanowire Cross-Junction Interconnects.* Nano Letters **17**, 2596 (2017).

[128] Y. Huang. *Directed Assembly of One-Dimensional Nanostructures into Functional Networks.* Science **291**, 630 (2001).

[129] Y. Huang. *Logic Gates and Computation from Assembled Nanowire Building Blocks.* Science **294**, 1313 (2001).

[130] N. A. Melosh. *Ultrahigh-Density Nanowire Lattices and Circuits.* Science **300**, 112 (2003).

[131] Ö. Gül, D. J. van Woerkom, I. van Weperen, D. Car, S. R. Plissard, E. P. A. M. Bakkers, and L. P. Kouwenhoven. *Towards high mobility InSb nanowire devices.* Nanotechnology **26**, 215202 (2015).

[132] D. Car, J. Wang, M. A. Verheijen, E. P. A. M. Bakkers, and S. R. Plissard. *Rationally Designed Single-Crystalline Nanowire Networks.* Advanced Materials **26**, 4875 (2014).

[133] T. Rieger, D. Rosenbach, D. Vakulov, S. Heedt, T. Schäpers, D. Grützmacher, and M. I. Lepsa. *Crystal Phase Transformation in Self-Assembled InAs Nanowire Junctions on Patterned Si Substrates.* Nano Letters **16**, 1933 (2016).

[134] J.-H. Kang, Y. Cohen, Y. Ronen, M. Heiblum, R. Buczko, P. Kacman, R. Popovitz-Biro, and H. Shtrikman. *Crystal Structure and Transport in Merged InAs Nanowires MBE Grown on (001) InAs.* Nano Letters **13**, 5190 (2013).

[135] D. Dalacu, A. Kam, D. G. Austing, and P. J. Poole. *Droplet Dynamics in Controlled InAs Nanowire Interconnections.* Nano Letters **13**, 2676 (2013).

[136] G. Tutuncuoglu, M. de la Mata, D. Deiana, H. Potts, F. Matteini, J. Arbiol, and A. Fontcuberta i Morral. *Towards defect-free 1-D GaAs/AlGaAs heterostructures based on GaAs nanomembranes.* Nanoscale **7**, 19453 (2015).

[137] Z. Yang, A. Surrente, G. Tutuncuoglu, K. Galkowski, M. Cazaban-Carrazé, F. Amaduzzi, P. Leroux, D. K. Maude, A. Fontcuberta i Morral, and P. Plochocka. *Revealing Large-Scale Homogeneity and Trace Impurity Sensitivity of GaAs Nanoscale Membranes.* Nano Letters **17**, 2979 (2017).

[138] C.-Y. Chi, C.-C. Chang, S. Hu, T.-W. Yeh, S. B. Cronin, and P. D. Dapkus. *Twin-Free GaAs Nanosheets by Selective Area Growth: Implications for Defect-Free Nanostructures.* Nano Letters **13**, 2506 (2013).

[139] G. Tutuncuoglu, M. de la Mata, D. Deiana, H. Potts, F. Matteini, J. Arbiol, and A. Fontcuberta i Morral. *Towards defect-free 1-D GaAs/AlGaAs heterostructures based on GaAs nanomembranes.* Nanoscale **7**, 19453 (2015).

[140] M. de la Mata, C. Magén, P. Caroff, and J. Arbiol. *Atomic Scale Strain Relaxation in Axial Semiconductor III-V Nanowire Heterostructures.* Nano Letters **14**, 6614 (2014).

[141] M. de la Mata, R. Leturcq, S. R. Plissard, C. Rolland, C. Magén, J. Arbiol, and P. Caroff. *Twin-Induced InSb Nanosails: A Convenient High Mobility Quantum System.* Nano Letters **16**, 825 (2016).

[142] M. O. Lipinski, H. Schuler, O. G. Schmidt, K. Eberl, and N. Y. Jin-Phillipp. *Strain-induced material intermixing of InAs quantum dots in GaAs.* Applied Physics Letters **77**, 1789 (2000).

[143] E. Pehlke, N. Moll, and M. Scheffler. *The equilibrium shape of quantum dots.* arXiv preprint cond-mat/9612004 (1996).

[144] N. Moll, M. Scheffler, and E. Pehlke. *Influence of surface stress on the equilibrium shape of strained quantum dots.* Physical Review B **58**, 4566 (1998).

[145] J. G. Belk, D. W. Pashley, C. F. McConville, J. L. Sudijono, B. A. Joyce, and T. S. Jones. *Surface atomic configurations due to dislocation activity in InAs/GaAs(110) heteroepitaxy.* Physical Review B **56**, 10289 (1997).

[146] B. Z. Nosho, L. A. Zepeda-Ruiz, R. I. Pelzel, W. H. Weinberg, and D. Maroudas. *Surface morphology in InAs/GaAs(111)A heteroepitaxy: Experimental measurements and computer simulations.* Applied Physics Letters **75**, 829 (1999).

[147] H. Potts, M. Friedl, F. Amaduzzi, K. Tang, G. Tütüncüoglu, F. Matteini, E. Alarcon Lladó, P. C. McIntyre, and A. Fontcuberta i Morral. *From Twinning to Pure Zincblende Catalyst-Free InAs(Sb) Nanowires.* Nano Letters **16**, 637 (2016).

[148] J. M. García, G. Medeiros-Ribeiro, K. Schmidt, T. Ngo, J. L. Feng, A. Lorke, J. Kotthaus, and P. M. Petroff. *Intermixing and shape changes during the formation of InAs self-assembled quantum dots.* Applied Physics Letters **71**, 2014 (1997).

[149] C. W. J. Beenakker and H. van Houten. *Boundary scattering and weak localization of electrons in a magnetic field.* Physical Review B **38**, 3232 (1988).

[150] M. Fahed, L. Desplanque, D. Troadec, G. Patriarche, and X. Wallart. *Selective area heteroepitaxy of GaSb on GaAs (001) for in-plane InAs nanowire achievement.* Nanotechnology **27**, 505301 (2016).

[151] A. Trampert, E. Tournie, and K. H. Ploog. *Influence of the Growth Mode on the Microstructure of Highly Mismatched InAs/GaAs Heterostructures.* Physica Status Solidi (a) **145**, 481 (1994).

[152] L. E. Ocola and A. Stein. *Effect of cold development on improvement in electron-beam nanopatterning resolution and line roughness.* Journal of Vacuum Science & Technology B: Microelectronics and Nanometer Structures **24**, 3061 (2006).

[153] D. B. Suyatin, C. Thelander, M. T. Björk, I. Maximov, and L. Samuelson. *Sulfur passivation for ohmic contact formation to InAs nanowires.* Nanotechnology **18**, 105307 (2007).

[154] S. Hikami, A. I. Larkin, and Y. Nagaoka. *Spin-Orbit Interaction and Magnetoresistance in the Two Dimensional Random System.* Progress of Theoretical Physics **63**, 707 (1980).

[155] B. Al'Tshuler and A. Aronov. *Magnetoresistance of thin films and of wires in a longitudinal magnetic field.* JETP Lett., **33**, 499 (1981).

[156] Z. Sun, O. Hazut, R. Yerushalmi, L. J. Lauhon, and D. N. Seidman. *Criteria and considerations for preparing atom-probe tomography specimens of nanomaterials utilizing an encapsulation methodology.* Ultramicroscopy **184**, 225 (2018).

[157] K. Thompson, D. Lawrence, D. Larson, J. Olson, T. Kelly, and B. Gorman. *In situ site-specific specimen preparation for atom probe tomography.* Ultramicroscopy **107**, 131 (2007).

[158] G. Tutuncuoglu, M. de la Mata, D. Deiana, H. Potts, F. Matteini, J. Arbiol, and A. Fontcuberta i Morral. *Towards defect-free 1-D GaAs/AlGaAs heterostructures based on GaAs nanomembranes.* Nanoscale **7**, 19453 (2015).

[159] D. Lockwood, G. Yu, and N. Rowell. *Optical phonon frequencies and damping in AlAs, GaP, GaAs, InP, InAs and InSb studied by oblique incidence infrared spectroscopy.* Solid State Communications **136**, 404 (2005).

[160] M. Cantoro, A. V. Klekachev, A. Nourbakhsh, B. Sorée, M. M. Heyns, and S. De Gendt. *Long-wavelength, confined optical phonons in InAs nanowires probed by Raman spectroscopy.* The European Physical Journal B **79**, 423 (2011).

[161] L. Pavesi, G. Mariotto, J. Carlin, A. Rudra, and R. Houdré. *Raman study of a single InP/InAs/InP strained quantum well.* Solid State Communications **84**, 705 (1992).

[162] S. Birner, T. Zibold, T. Andlauer, T. Kubis, M. Sabathil, A. Trellakis, and P. Vogl. *nextnano: General Purpose 3-D Simulations.* IEEE Transactions on Electron Devices **54**, 2137 (2007).

[163] F. Glas. *Critical dimensions for the plastic relaxation of strained axial heterostructures in free-standing nanowires.* Physical Review B **74**, 121302 (2006).

[164] X. Zhang, V. G. Dubrovskii, N. V. Sibirev, and X. Ren. *Analytical Study of Elastic Relaxation and Plastic Deformation in Nanostructures on Lattice Mismatched Substrates.* Crystal Growth & Design **11**, 5441 (2011).

[165] V. G. Dubrovskii, N. V. Sibirev, X. Zhang, and R. A. Suris. *Stress-Driven Nucleation of Three-Dimensional Crystal Islands: From Quantum Dots to Nanoneedles.* Crystal Growth & Design **10**, 3949 (2010).

[166] V. G. Dubrovskii, V. Consonni, A. Trampert, L. Geelhaar, and H. Riechert. *Scaling thermodynamic model for the self-induced nucleation of GaN nanowires.* Physical Review B **85**, 165317 (2012).

[167] J.-Y. Shen, C. Chatillon, I. Ansara, A. Watson, B. Rugg, and T. Chart. *Optimisation of the thermodynamic and phase diagram data in the ternary As-Ga-In system.* Calphad **19**, 215 (1995).

[168] D. Schlenker, T. Miyamoto, Z. Pan, F. Koyama, and K. Iga. *Miscibility gap calculation for* $Ga_{1-x}In_xN_yAs_{1-y}$ *including strain effects.* Journal of Crystal Growth **196**, 67 (1999).

[169] I. van Weperen, B. Tarasinski, D. Eeltink, V. S. Pribiag, S. R. Plissard, E. P. A. M. Bakkers, L. P. Kouwenhoven, and M. Wimmer. *Spin-orbit interaction in InSb nanowires.* Physical Review B **91**, 201413 (2015).

[170] C. W. J. Beenakker and H. van Houten. *Boundary scattering and weak localization of electrons in a magnetic field.* Physical Review B **38**, 3232 (1988).

[171] S. Chakravarty and A. Schmid. *Weak localization: The quasiclassical theory of electrons in a random potential.* Physics Reports **140**, 193 (1986).

[172] B. L. Altshuler, D. Khmel'nitzkii, A. I. Larkin, and P. A. Lee. *Magnetoresistance and Hall effect in a disordered two-dimensional electron gas.* Physical Review B **22**, 5142 (1980).

[173] S. Hikami, A. I. Larkin, and Y. Nagaoka. *Spin-Orbit Interaction and Magnetoresistance in the Two Dimensional Random System.* Progress of Theoretical Physics **63**, 707 (1980).

[174] B. Al'Tshuler and A. Aronov. *Magnetoresistance of thin films and of wires in a longitudinal magnetic field.* JETP Lett., **33**, 499 (1981).

[175] D. Liang and X. P. Gao. *Strong Tuning of Rashba Spin-Orbit Interaction in Single InAs Nanowires.* Nano Letters **12**, 3263 (2012).

[176] A. E. Hansen, M. T. Björk, C. Fasth, C. Thelander, and L. Samuelson. *Spin relaxation in InAs nanowires studied by tunable weak antilocalization.* Physical Review B **71**, 205328 (2005).

[177] J. Clarke and F. K. Wilhelm. *Superconducting quantum bits.* Nature **453**, 1031 (2008).

[178] M. Nahum and J. M. Martinis. *Ultrasensitive-hot-electron microbolometer.* Appl. Phys. Lett. **63**, 3075 (1993).

[179] H. Courtois, S. Rajauria, P. Gandit, F. W. J. Hekking, and B. Pannetier. *Inherent Thermometry in a Hybrid Superconducting Tunnel Junction.* J. Low Temp. Phys. **153**, 325 (2008).

[180] F. Giazotto, T. T. Heikkilä, A. Luukanen, A. M. Savin, and J. P. Pekola. *Opportunities for mesoscopics in thermometry and refrigeration: Physics and applications.* Rev. Mod. Phys. **78**, 217 (2006).

[181] H. Q. Nguyen, T. Aref, V. J. Kauppila, M. Meschke, C. B. Winkelmann, H. Courtois, and J. P. Pekola. *Trapping hot quasi-particles in a high-power superconducting electronic cooler.* New Journal of Physics **15**, 085013 (2013).

[182] J. M. Martinis, K. B. Cooper, R. McDermott, M. Steffen, M. Ansmann, K. D. Osborn, K. Cicak, S. Oh, D. P. Pappas, R. W. Simmonds, and C. C. Yu. *Decoherence in Josephson Qubits from Dielectric Loss.* Phys. Rev. Lett. **95**, 210503 (2005).

[183] M. V. Fistul. *Resonant enhancement of macroscopic quantum tunneling in Josephson junctions: Influence of coherent two-level systems.* Phys. Rev. B **92**, 014505 (2015).

[184] C. Wang, C. Axline, Y. Y. Gao, T. Brecht, Y. Chu, L. Frunzio, M. H. Devoret, and R. J. Schoelkopf. *Surface participation and dielectric loss in superconducting qubits.* Appl. Phys. Lett. **107**, 162601 (2015).

[185] J. B. Chang, M. R. Vissers, A. D. Córcoles, M. Sandberg, J. Gao, D. W. Abraham, J. M. Chow, J. M. Gambetta, M. Beth Rothwell, G. A. Keefe, M. Steffen, and D. P. Pappas. *Improved superconducting qubit coherence using titanium nitride.* Appl. Phys. Lett. **103**, 012602 (2013).

[186] L. Zeng, D. T. Tran, C.-W. Tai, G. Svensson, and E. Olsson. *Atomic structure and oxygen deficiency of the ultrathin aluminium oxide barrier in Al/AlOx/Al Josephson junctions.* Sci. Rep. **6**, 29679 (2016).

[187] S. Oh, K. Cicak, J. S. Kline, M. A. Sillanpää, K. D. Osborn, J. D. Whittaker, R. W. Simmonds, and D. P. Pappas. *Elimination of two level fluctuators in superconducting quantum bits by an epitaxial tunnel barrier.* Phys. Rev. B **74**, 100502(R) (2006).

[188] J. P. Pekola, V. F. Maisi, S. Kafanov, N. Chekurov, A. Kemppinen, Y. A. Pashkin, O.-P. Saira, M. Möttönen, and J. S. Tsai. *Environment-Assisted Tun-*

neling as an Origin of the Dynes Density of States. Phys. Rev. Lett. **105**, 026803 (2010).

[189] J. Aumentado, M. W. Keller, J. M. Martinis, and M. H. Devoret. *Nonequilibrium Quasiparticles and 2e Periodicity in Single-Cooper-Pair Transistors.* Phys. Rev. Lett. **92**, 066802 (2004).

[190] D. Rainis and D. Loss. *Majorana qubit decoherence by quasiparticle poisoning.* Phys. Rev. B **85**, 174533 (2012).

[191] D. Ristè, C. C. Bultink, M. J. Tiggelman, R. N. Schouten, K. W. Lehnert, and L. DiCarlo. *Millisecond charge-parity fluctuations and induced decoherence in a superconducting transmon qubit.* Nat. Commun. **4**, 2936 (2013).

[192] D. Aasen, M. Hell, R. V. Mishmash, A. Higginbotham, J. Danon, M. Leijnse, T. S. Jespersen, J. A. Folk, C. M. Marcus, K. Flensberg, and J. Alicea. *Milestones Toward Majorana-Based Quantum Computing.* Phys. Rev. X **6**, 031016 (2016).

[193] S. M. Albrecht, E. B. Hanson, A. P. Higginbotham, F. Kuemmeth, T. S. Jespersen, J. Nygård, P. Krogstrup, J. Danon, K. Flensberg, and C. M. Marcus. *Transport Signatures of Quasiparticle Poisoning in a Majorana Island.* Phys. Rev. Lett. **118**, 137701 (2017).

[194] T. A. Fulton and G. J. Dolan. *Observation of single-electron charging effects in small tunnel junctions.* Phys. Rev. Lett. **59**, 109 (1987).

[195] G. E. Blonder, M. Tinkham, and T. M. Klapwijk. *Transition from metallic to tunneling regimes in superconducting microconstrictions: Excess current, charge imbalance, and supercurrent conversion.* Phys. Rev. B **25**, 4515 (1982).

[196] M. Tinkham. *Introduction to superconductivity* (Dover, New York, 1996), 2nd edition.

[197] D. I. Bradley, R. E. George, D. Gunnarsson, R. P. Haley, H. Heikkinen, Y. A. Pashkin, J. Penttilä, J. R. Prance, M. Prunnila, L. Roschier, *et al. Nanoelectronic primary thermometry below 4 mK.* Nature communications **7**, 10455 (2016).

[198] C. Caroli, P. G. D. Gennes, and J. Matricon. *Bound Fermion states on a vortex line in a type II superconductor.* Phys. Lett. **9**, 307 (1964).

[199] S. Simon. *The Oxford Solid State Basics* (OUP Oxford, 2013).

[200] I. K. Marmorkos, C. W. J. Beenakker, and R. A. Jalabert. *Three signatures of phase-coherent Andreev reflection.* Phys. Rev. B **48**, 2811 (1993).

[201] J. Melsen and C. Beenakker. *Reflectionless tunneling through a double-barrier NS junction.* Physica B: Condensed Matter **203**, 219 (1994).

[202] W. Belzig, C. Bruder, and G. Schön. *Local density of states in a dirty normal metal connected to a superconductor.* Phys. Rev. B **54**, 9443 (1996).

[203] B. Crouzy, E. Bascones, and D. A. Ivanov. *Minigap in a superconductor–normal metal junction with paramagnetic impurities.* Phys. Rev. B **72**, 092501 (2005).

[204] G. Fagas, G. Tkachov, A. Pfund, and K. Richter. *Geometrical enhancement of the proximity effect in quantum wires with extended superconducting tunnel contacts.* Phys. Rev. B **71**, 224510 (2005).

[205] A. Altland, B. D. Simons, and D. T. Semchuk. *Field theory of mesoscopic fluctuations in superconductor-normal-metal systems.* Adv. Phys. **49**, 321 (2000).

[206] E. Scheer, W. Belzig, Y. Naveh, M. H. Devoret, D. Esteve, and C. Urbina. *Proximity Effect and Multiple Andreev Reflections in Gold Atomic Contacts.* Phys. Rev. Lett. **86**, 284 (2001).

[207] G. P. Antonio Barone. *Physics and Applications of the Josephson Effect* (Wiley, 1982).

[208] S. Shapiro. *Josephson Currents in Superconducting Tunneling: The Effect of Microwaves and Other Observations.* Phys. Rev. Lett. **11**, 80 (1963).

[209] C. C. Grimes and S. Shapiro. *Millimeter-Wave Mixing with Josephson Junctions.* Phys. Rev. **169**, 397 (1968).

[210] F. W. J. Hekking and Y. V. Nazarov. *Subgap conductivity of a superconductor–normal-metal tunnel interface.* Phys. Rev. B **49**, 6847 (1994).

[211] C. Beenakker. *Andreev Billiards*, 131–174 (Springer Berlin Heidelberg, Berlin, Heidelberg, 2005).

[212] W. Belzig, F. K. Wilhelm, C. Bruder, G. Schön, and A. D. Zaikin. *Quasiclassical Green's function approach to mesoscopic superconductivity.* Superlattices and Microstructures **25**, 1251 (1999).

[213] A. A. Golubov and M. Y. Kupriyanov. *Theoretical investigation of Josephson tunnel junctions with spatially inhomogeneous superconducting electrodes.* Journal of Low Temperature Physics **70**, 83 (1988).

[214] M. Tinkham. *Effect of Fluxoid Quantization on Transitions of Superconducting Films.* Phys. Rev. **129**, 2413 (1963).

[215] F. E. Harper and M. Tinkham. *The Mixed State in Superconducting Thin Films.* Phys. Rev. **172**, 441 (1968).

Acknowledgment

I would like to thank Prof. Dr. Dominik Zumbühl for giving me the opportunity to do a PhD in his group. It was a joy to work under Dominik's supervision, who was always ready to help overcoming any obstacle that appear on the way. It was a pleasure to discuss experiments with such a passionate physicist, who is interested in all aspects down to the smallest details. I am very grateful for the time he spent showing me how to do scientific research.

I would like to thank Dr. Myrsini Lafkioti for introducing me to the low temperature experiments and for teaching me what to do and what not to do with the very valuable CEO samples. I also would like to say big thank you to Dr. Christian Scheller, who was always helping me in the lab and with whom I spend numerous hours discussing physics. This work would not be possible without his help.

I would like to thank Prof. Dr. Yaroslav Tserkovnyak and Daniel Hill for helping us to understand our results and for developing a theoretical framework to describe our experiment. I also would like to thank Prof. Dr. Jose Carlos Egues for very interesting, informative and helpful discussions, which helped me to gain a much deeper understanding of our experiment works.

I would like to thank Prof. Dr. Amir Yacoby and Prof. Dr. Bertrand Halperin for very fruitful discussions. I also would like to thank Prof. Dr. Daniel Loss and Prof. Dr. Jelena Klinovaja, who answered many theory-related questions.

I would like to thank Prof. Dr. Anna Foncuberta, Martin Friedl and Dr. Gözde Tütüncüoglu for the growth of nanomembranes samples. I also would like to thank Dr. Pirmin Weigele and Kristopher Cerveny for a great collaboration on this project. Another big thanks to Kris for correcting this manuscript.

I am grateful to Prof. Dr. Jukka Pekola, Prof. Dr. Matthias Meschke and Dr. Anna Feshchenko for providing NIS samples of exceptional quality, that were consumed quite

heavily during initial bonding attempts. Another big thanks to Dr. Lucas Casparis, Dr. Dario Maradan and Dr. Mario Palma, who initiated and advanced the low temperature measurements on NIS samples.

I would like to thank Dr. Liuqi Yu for sharing his scientific experience and for the excellent times we spent outside of the university. I also would like to thank Leon Camenzind, who was in the lab during so many Friday evenings ready to help and answer any question, Dr. Yemliha Bilal Kalyoncu, who was a great neighbor and skilled climbing buddy, and Dr. Mirko Rehman, who was a great example of how to do a research in a systematic way. I also would like to thank all other current and previous group members for creating an excellent working atmosphere.

All our measurements benefited significantly from state of the art low-noise electronic equipment developed by the electronic workshop lead by Michael Steinacher. Thanks to help of Patrick Stöcklin and Sasha Martin from the mechanical workshop all our technical problems were solved perfectly and almost instantly. I would like to thank Dominik Sifrig for delivering liquid helium always on time and his flexibility for short notice requests.

I am very thankful to Barbara Kammermann and Astrid Kalt who solved so many administrative problems during my stay in Basel.

Special thanks to my wife Anna, for patience and support and to my sister and parents.

Curriculum Vitae

Taras Patlatiuk

2004 - 2008	Physics Gymnasium, Lviv, Ukraine
2008 - 2012	Bachelor of physics, Taras Shevchenko National University of Kiev, Ukraine
2012 - 2014	Master Degree in Physics, Taras Shevchenko National University of Kiev
2014 - 2019	PhD at University of Basel, Switzerland

Publications

T. Patlatiuk, C. P. Scheller, D. Hill, Y. Tserkovnyak, G. Barak, A. Yacoby, L. N. Pfeiffer, K. W. West, D. M. Zumbühl, *Evolution of the quantum Hall bulk spectrum into chiral edge states.* Nature Communicationsvolume **9**, 3692 (2018)

M. Friedl, K. Cerveny, P. Weigele, G. Tütüncüoglu, S. Martí-Sánchez, C. Huang, T. Patlatiuk, H. Potts, Z. Sun, M. O. Hill, L. Güniat, W. Kim, M. Zamani, V. G. Dubrovskii, J. Arbiol, L. J. Lauhon, D. M. Zumbühl, and A. Fontcuberta i Morral, *Template-Assisted Scalable Nanowire Networks.* Nano Letters **18** (4), 2666 (2018)

T. Patlatiuk, C. P. Scheller, D. Hill, Y. Tserkovnyak, G. Barak, A. Yacoby, L. N. Pfeiffer, K. W. West, D. M. Zumbühl, *Landau Level Wave-Functions and the Density Profile at Sharp Edges.* In preparation for publication.

M. Palma, C. P. Scheller, L. Chirolli, T. Patlatiuk, L. Casparis, A. V. Feshchenko, D. Maradan, M. Meschke, J. P. Pekola, D. M. Zumbühl, *Sub-gap bound-states in normal metal-insulator-superconductor junctions.* In preparation for publication.